FIRST-PRINCIPLES STUDY OF HEMATITE (α-Fe_2O_3) SURFACE DOPED WITH COPPER, TITANIUM, NICKEL, AND MANGANESE

BY

CLARENCE VUSI MABASO

(11628655)

THESIS

SUBMITTED IN FULFILMENT OF THE REQUIREMENTS OF THE MASTER OF SCIENCE (M.Sc.) DEGREE

IN

PHYSICS

FACULTY OF SCIENCE, ENGINEERING AND AGRICULTURE

AT THE

UNIVERSITY OF VENDA

SUPERVISOR: DR N.E. MALUTA (UNIVEN)

CO-SUPERVISOR: PROF R.R. MAPHANGA (CSIR)

YEAR: 2021

Declaration

I, Clarence Vusi Mabaso, declare that the dissertation titled “First-principles study of Hematite (α-Fe_2O_3) surface structures doped with Copper (Cu), Titanium (Ti), nickel (Ni) and manganese (Mn)” for the Master of Science degree in Physics at the University of Venda hereby submitted by me has not been previously submitted for a degree at this or any other university. Over and above that, I certify that it is my own work in design and execution and that all the reference materials contained therein have been fully acknowledged.

Signed by Mabaso at University of Venda on the 14th day of March 2022

Dedications

I dedicate this dissertation to myself and my family for their patience and support as I continue with my studies. Special dedication goes to my mother Maria, my two brothers Mxolisi and Stein Mabaso, lastly my partner Nandi Ndlovu and our daughter Masana Mabaso.

Acknowledgements

I wish to express my sincere gratitude to the following for the assistance and support in making this research possible:

- Dr. N.E Maluta for his critical and enthusiastic supervision, under his supervision I have learnt a lot in the field of research. I salute him for his time, patience and understanding, I thank him for believing in me, not forgetting my co-supervisor Prof RR Maphanga.
- I acknowledge the University of Venda and the department of Physics for granting me the opportunity to continue with my studies.
- To all physics department staff and senior students for their support on many academic works.
- I also would like to acknowledge all my family members and friends for moral support through my studies.
- I would also like to acknowledge the financial support I got from the National Institute for Theoretical and Computational Sciences (NiTheCS), thank you.

Abstract

Hematite has attracted research interest for many years due to its application in water splitting. Despite its attractive characters such as a reasonable optical band gap, the semiconductor is still faced with great uncertainty for the accomplishment of hematite based photoelectrochemical cells for water splitting. Doping with transition metals has shown to be a practical solution to overcome some of the limitations faced with hematite by modifying the energy band to improve its photo-electrochemical (PEC) activity. This study explored two surface structures of pure and transition metals (Ti, Cu, Ni and Mn) doped- α-Fe_2O_3 oriented in the directions (001) and (101). Calculations via the first principle using the density functional theory (DFT) were adopted, the results show that the doping of transition metals in α-Fe_2O_3 has an effect in modifying both the valence and conduction band edges. Specifically, doping Ti introduces more electrons in the conduction band and fills the unoccupied 3d states, which could improve the rate of charge transportation and likely enhance the electrical conductivity of α-Fe_2O_3. Doping with Mn, Ni, and Cu has effectively improved the absorption coefficient for α-Fe_2O_3 (001) and (101) surfaces, in the visible light region. The overall analysis of the results shows an opportunity for a successful photo-electrochemical water splitting application.

Key words: Hematite, density functional theory, transition metals, band gap, and surface structures.

Table of contents

List of abbreviations

CASTEP - Cambridge Serial Total Energy Package

CBM - Conduction Band Minimum

CB - Conduction Band

CO_2 - Carbon Dioxide

Cu - Copper

DFT - Density Functional Theory

DFT+U - Density Functional Theory with Hubbard Potential

DOS - Density of States

E_C - Conduction Band Energy

E_F - Fermi Level Energy

Eg - Energy Gap

E_V - Valence Band Energy

GGA - Generalized Gradient Approximation

GGA+U - Generalized Gradient Approximation with Hubbard Potential

H_2 - Hydrogen Gas

HER - Hydrogen Evolution Reaction

KS - Kohn-Sham

LDA - Local Density Approximation

NHE - Normal Hydrogen Electrode

OER - Oxygen Evolution Reaction

O_2 - Oxygen Gas

PDOS - Partial Density of States

PEC - Photo-electrochemical

PV - Photovoltaic

REWP - Renewable Energy White Paper

STH - Solar To Hydrogen

Ti - Titanium

TM - Transition Metal

UV - Ultra-violet

VASP - Vienna Ab-initio Simulation Package

VB - Valence Band

VBM - Valence Band Maximum

List of figures

CHAPTER ONE

1. Introduction

1.1 Renewable energy

Energy demand have been subjected to major changes over the past years, the economic and environmental issues are energy related [1]. Recently, different weather-related catastrophes such as heat waves on the earth, drought and cyclones are prominent signs from nature that are human's concerns about climate change [2]. Africa is assessed as a topmost region with supreme liability to the outcome of the changing of climate, this is because of the increase in the number of people in a population and contributed by the activities of human, incompetence to conform to change, anticipated energy and over-reliance on subsistence agriculture crisis by the United Nations organization [3]. The obligation for various resource and the likeliness of resource exhaustion is still a challenge in countries that are developing. In Sub-Saharan Africa since 1980, carbon dioxide emissions from the use of petroleum have witnessed an increasing trend, and there are fears that Africa, with its low capital, would be more vulnerable to extreme weather conditions [4], for instance, this will affect food production, hence, the alteration from burning of no-renewable fuels to renewable energy resource would equivalently underestimate Africa's economic demand to energy and ensure environmental sustainability. Non-renewable resources are the most contributing sources of energy around the globe, Figure 1 displays the energy sources for the whole world in 2017. Unfortunately, most renewable energy sources (geothermal, biomass, solar, and wind) still provide just a small portion of total energy production

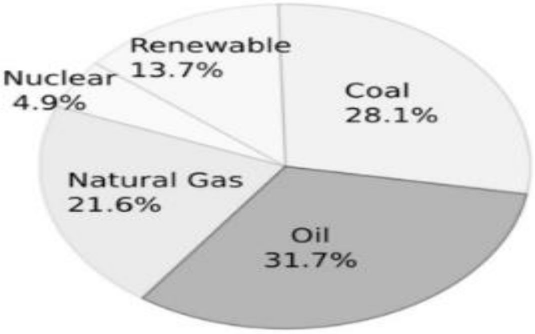

Figure 1: Global energy sources [5].

The search for renewable energy is driven by uncertainty in energy supply, and due to that, non-renewable resources currently make up a sizeable percentage of the world's energy supply, these resources will run out in due course. sufficient and reliable supplies of affordable clean energy, obtained in environmentally sustainable ways, are essential to economic prosperity and environmental quality [6]. Effective energy development strategies generally involve three important technological changes: replacement of fossil fuels by diverse sources of renewable energy, energy savings on side of need, and efficiency improvements in energy production [7]. Renewable energy is originated from an extensive scale of resources that are established on self-sustaining energy sources, attractive examples are solar energy (sunlight), biomass, hydropower, wind energy and agricultural waste, these resources are renewable and can be used to generate energy (electricity) for our homes, fuel for transportation, fuels for transportation, industrial processes and all economic divisions [8]. The range of technologies and resources is one of the most obvious features of renewable forms of energy. The absolute size of the renewable energy resource is massive, and could, in proposition, make a very significant contribution to world energy demands surpassing the current supply of electricity around the world [9].

Research has shown that there has been greater vitality of certain regions with numerous demographic and environmental benefits, this is mainly a contribution of using energy sources that are renewable such solar energy (photovoltaic and solar thermal), hydropower, wind energy, and biomass-derived fuel. Previous studies show that the contribution of renewable energy resources yield an extensive advantage in making less of pollution locally and worldwide, thus this contribution gives relief to the changing of climate. The trials of implementing cheap and reliable energy supply are a basic precondition for growing the economy and technological development. Electricity generated from sustainable energy sources can be of paramount in the generation of electricity in countries found in Africa [10].

Statistics showed that in 2012, South Africa had 85% of the population with access to electricity and targeted that by 2019, 100% should have access to electricity [11], however, South African's major supply of electricity is through the burning of coal, a supply from Eskom. Hence, there is a need for development of renewable resource technologies to overcome this problem. According to the policy of renewable energy of 2003, statistics patterned South Africa as a fast-transitioning country regarding the development of renewable energy sources. South African made a target on renewable energy technologies supplies that by 2030 they should be able to supply 8.4 GW from each, solar PV and wind energy [3], the target was set by the Renewable Energy White Paper (REWP 2003), developed by the Department of Minerals [12].

1.2 Solar energy

The Sun is a prime source of infinite free energy, it is estimated to produce about $3x10^{24}$ joules of energy per year, 10,000 times that of the world's energy use [13], thus , solar energy is by far considered the most commonly used clean energy resource. In principle, solar energy holds the potential to sufficiently carry out the energy demands of the whole world, provided technologies for its harvesting and distributing were readily available [14]. South Africa is one of the countries with the highest potential to deploy renewable energy sources. In 2009, it was reported that in the region of 194,000 km^2 in South Africa, there is a great solar radiation potential, this includes the Northern Cape province which is considered amongst the best area for solar resource [3]. There are recent new technologies established to generate electricity from energy harnessed from the sun. These ways are being used worldwide as alternatives to non-renewable technologies and are proven to be relevant. There are challenges and interests related the use of solar energy technologies such as the high cost of PV cells, low efficiency of domestic solar panels [14]. Storage problem is the most prominent shortcoming of electricity generated from solar energy, the storage technology involves a considerable administration cost because of its finite life span. However, technologies such as solar fuel cells, enhanced chemical batteries, and super capacitors are deemed as alternative energy storage solutions. Production of hydrogen using solar water splitting technology is an option to solve storage problem since hydrogen can be used as solar fuels. The recognition of hydrogen as a potential fuel for transport and industry is growing massively. Hydrogen can be produced by electrolysis or photolysis of water, and its oxidation produces no greenhouse gases. Moreover, it is the best fuel for fuel cells, which generate electricity directly by reverse electrolysis [15].

1.3. Introduction to solar water splitting.

The large amount of energy that falls on earth as sunlight has motivated the phenomenon of solar energy regeneration technologies such as electricity converted by photovoltaics (PV) and most recent technology of solar fuels through photo-electrochemical (PEC) water splitting. Thus, large-scale conversion of solar energy to usable form is a potential solution to future energy needs. The demand means that the harvesting of solar energy, and storage must be prioritized and cost operative.

.

Conversion of solar energy into chemical energy can be carried out in a most distinctive and coherent way by water splitting [16]. Water splitting is contestably one of the most significant reactions in chemistry because its oxidation process produces oxygen, permitting an expansive range of life to different species. The reduction process simply pilot to the production of hydrogen, which may be considered a probable clean energy carrier; therefore, producing hydrogen by splitting water using sunlight could be one possible solution to energy crisis [17], [18].

Using a semiconductor to harvest solar photons to break the bond between hydrogen and oxygen in the water molecule is one approach to successfully produce hydrogen, and, if successful, it could set up a mechanism that is inclusive for utilizing hydrogen as a pure solar fuel [19]. Hydrogen is an energy carrier such as electricity and can be produced by water splitting [6]. To successfully perform this process, a designated semiconductor must satisfy a sum total of precise requirements that include an acceptable band gap, efficient visible light absorption, charge separation and transportation, interfacial charge-transfer kinetics, and suitable valence and conduction band positions relative to water oxidation and reduction potential and good stability in contact with aqueous solutions [20].

Using sunlight to photo-generate charge carriers in a semiconductor electrode, which then electrochemically dissociate water, is a more environmentally friendly and potentially a low-cost alternative. The advantage of solar water splitting over using photovoltaics to drive conventional electrolysis is that the photon energy is converted directly into chemical energy, simplifying the device to potentially reduce costs and increasing efficiency [21]. Photo-electrochemical (PEC) water splitting also resolves the threat of collecting and storing energy on large amounts. Comparable to the process of photosynthesis, solar energy is seized and stored in the form of chemical energy to produce solar fuels, and can be utilized at any given time when there is a need for energy [22].

PEC water splitting was initiated in early 1970s, when the work of Fujishima and Honda, built interest on the research of catalysts. Using PEC cell they illustrated an overall water splitting incorporated of a single crystalline TiO_2 undergoing the ultraviolet (UV) light, Pt used for cathode in the applied external bias [23]. Following then, different semiconductor materials have been investigated for use as photoelectrodes, including metal oxide semiconductors such as TiO_2, WO_3, $SrTiO_3$, Fe_2O_3, and narrow band gap semiconductors such as GaAs, CdSe, and CdS. Although small band gap semiconductors absorb more of the solar spectrum and so are potentially more efficient, their band energies may be unsuitable for the evolution of both O_2 and H_2. Non-oxide semiconductors are often severely corroded or photo-corroded under water dissociation conditions. The practicality of large-scale photoelectrochemical cells for hydrogen production based on group III-V semiconductors is also limited by the high cost of these materials [24]. For an absolute all-round water splitting, the valence band and conduction band edge positions of the semiconductor should be well matched with the water oxidation and reduction potentials. Figure. 2 is representation of the band edge positions of few semiconductors photoelectrodes comparable to the water oxidation-reduction potentials. Even though research has shown that majority of the devices that underwent PEC water splitting have experienced a very low efficiencies of solar-to-hydrogen (STH), investigations indicates that a semiconductor that have an energy band gap of 1.6 eV can achieve up to 30% STH. Even so, because of numerous uncompromising requirements of solar water splitting, it is still a challenge to find a perfect semiconductor material to undergo PEC water splitting. Consequently, majority of these materials still endure a very low in solar-to-hydrogen conversion [19].

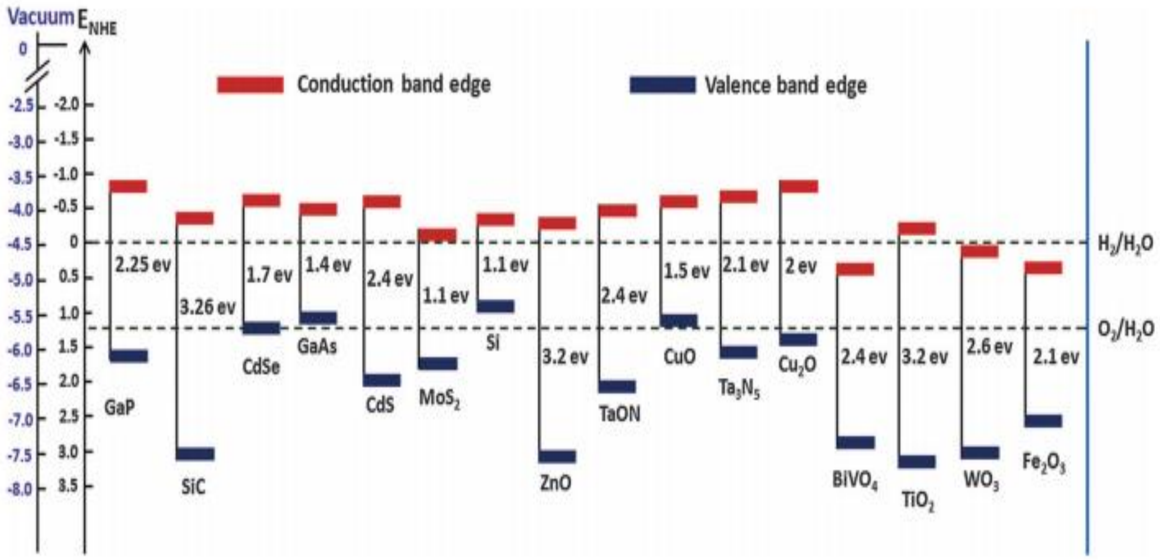

Figure 2: Edges of valence and conduction band of materials in the electrolyte at pH = 0 comparable to normal hydrogen electrode [19].

Metal oxides are noticeable materials for PEC photocatalytic activities, α-Fe_2O_3 is most regarded, because it is generally cheap, stable, and it is easily assembled on expansive scale. An intensive study on α-Fe_2O_3 have been carried out because of the semiconductor's multiple promising properties.

1.4 Hematite

Hematite (α-Fe_2O_3) has been identified as one of the most optimistic materials for solar water splitting applications, it is a semiconductor approximated to have a band gap of 2.1 eV allowing a macroscale of visible light to absorb about 40% in the incident solar spectrum. In theory, it is capable of converting the sun's energy into hydrogen to about 12.9% [25]. α-Fe_2O_3 have well-defined properties such as availability (abundance) of the material, non-toxicity and extraordinary chemical stability in aqueous electrolytes [26]. Furthermore, its valence band edge (VBE) position is thermodynamically suitable to drive water oxidation (E^0 (O_2/H_2O) = 1.23 V) by photogenerated holes, hence, hematite is a suitable photoanode.

Hematite has remarkable advantages compared to other metal oxides and has drawn a lot of interest in the solar energy conversion discipline. However, the efficiency of α-Fe_2O_3 for solar energy conversion is reported to be very low than the predicted value, this is caused by the fast electron-hole recombination and short hole diffusion length of the hole [26]. The PEC activity of α-Fe_2O_3 is still congested by a multiple drawbacks, following a comparatively poor optical absorption, poor kinetics of the oxygen evolution reaction, a very short excited-state lifetime ($\sim 10^{12}$ s), and poor electrical conductivity. [19]. These drawbacks considerable limit hematite for PEC applications. As a result, scientists have focused their efforts on understanding and improving the performance of α-Fe_2O_3, and fortunately, doping, nano-structuring and surface modification can address these shortcomings, doping have been studied to improve the electronic and optical properties of hematite, such as reducing the band gap to intensify the optical absorption coefficient in the visible light region [16].

Transition-metal doping has also been studied extensively to improve its PEC properties. Many metal ions such as Ti, Zn, Sn, Cr, Pt, and Ta have been adopted as effective dopants to improve the PEC activity of α-Fe_2O_3 electrodes for water splitting [26]..

1.5 Working principle of hematite photocatalyst.

Figure 3 shows a schematic diagram of the PEC used to perform the reaction. In PEC water splitting, according to Tamirat *et al.,* when a semiconductor is exposed to sunlight, electrons within the semiconductor are stimulated and migrate from the valence band to the conduction band (CB), leaving holes in the valence band in a condition that the semiconductor's energy gap is equal to or less than the energy of the absorbed photons. Holes and electrons will then move to the surface and are infused into the electrolyte using the co-catalyst to produce oxygen and hydrogen respectively [19],[28].

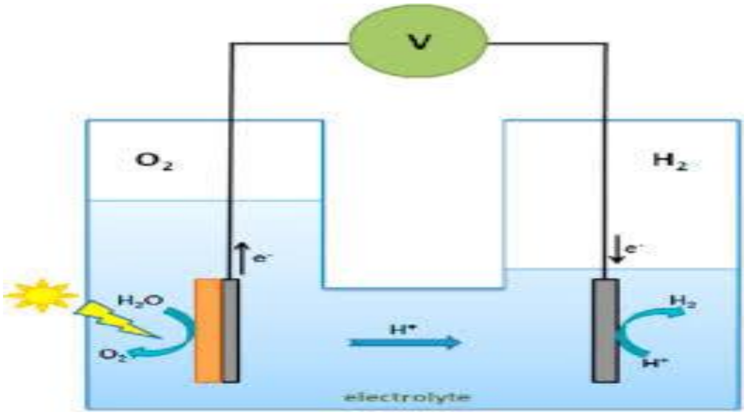

Figure 3: Basic setup for water splitting system: photo-electrochemical cell [29].

In PEC water splitting cells, the semiconductor electrode is the working electrode, while platinum is usually used as the counter electrode. At the semiconductor site, electrons and holes will be created; the holes will then produce O_2 at the semiconductor site, whereas electrons will migrate to the counter electrode to undergo a reduction process, resulting in H_2. To start the reduction-oxidation reaction, the highest level of the valence band should be higher than water oxidation level (E_{O_2/H_2O}, 1.23 V vs. Normal hydrogen electrode; (NHE)), while the lowest level of the conduction band should be lower than the hydrogen evolution potential (E_{H_2/H_2O}, 0 V vs. NHE) [30], as shown in Figure 3. In addition, materials should be chemically stable to resist photo-corrosion and the electron/hole pairs should have a longer life span. Due to a suitable band gap and chemical stability, α-Fe_2O_3 is a potential candidate to undergo this process.

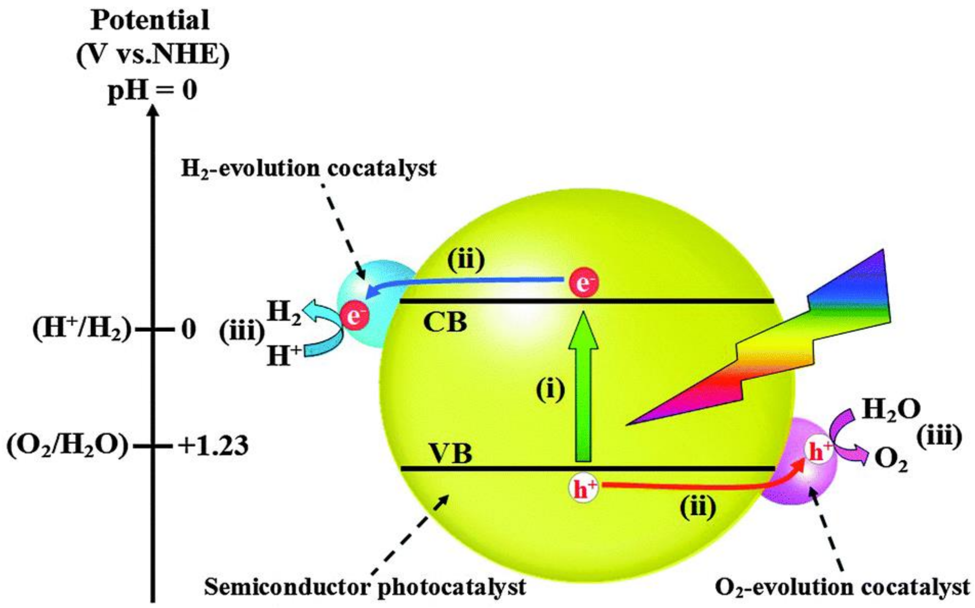

Figure 4: Schematic illustration of photocatalytic water splitting of a semiconductor [31]

Figure 4 shows the possible photo induced physical and chemical processes on and inside the surface of a semiconductor electrode throughout PEC splitting of the water molecule. The reaction involves a number of essential steps, such as: (i) photon absorption and charge (electron and hole) separation, (ii) transfer of electrons and holes, (iii) and on both co-catalyst surface chemical reactions, followed by water oxidation: oxygen evolution reaction (OER) and reduction reaction: hydrogen evolution reaction (HER). The general splitting of water into H_2 and O_2, is demonstrated in equations 1, [28]:

$$H_2O \rightarrow H_2 + \frac{1}{2}O_2 \qquad (1)$$

The absorbed photons generate the excited electrons and holes which (i) diffuse to the surface of the semiconductor particles (ii) participate in the HER and OER on the photocatalyst surface, as shown in Figure 3, provided by equations 2 and 3.

$$2H^+ + 2e^- \rightarrow H_2 \qquad E^0_{reduction} = 0.00\ V \qquad (2)$$

$$H_2O + 2h^+ \rightarrow 2H^+ + \frac{1}{2}O_2 \qquad E^0_{oxidation} = -1.23\ V \qquad (3)$$

At the electrode-electrolyte interface, the reaction occurs. When the semiconductor's Fermi level (E_F) surpass the electrolyte reduction-oxidation reaction potential, a space charge layer with a thickness of approximately 0.1-1 μm forms in the semiconductor surface closer to the area in contact with the solution [32].

When a semiconductor surface gets exposed to the electrolyte, there will be transfer of charge among the semiconductor and the electrolyte until the system has reached equilibrium (Figure 5) [24]. This equilibrium causes a band-bending in the phase of the semiconductor, which is determined by the difference in Fermi levels of the electrolyte and the semiconductor. The charge carriers assembled at the surface resulted in the bending region. Figure 4 display how charges respond in the semiconductor before and after equilibration when it encounters an electrolyte [19].

Because there is no formal energy of states in the semiconductor band gap, the change in Fermi level position will be much greater for the semiconductor than for the solution. The following descriptions are for n-type semiconductors (such as Fe_2O_3), in which electrons are the majority charge carrier and the Fermi level lies just below the edge of the conduction band.

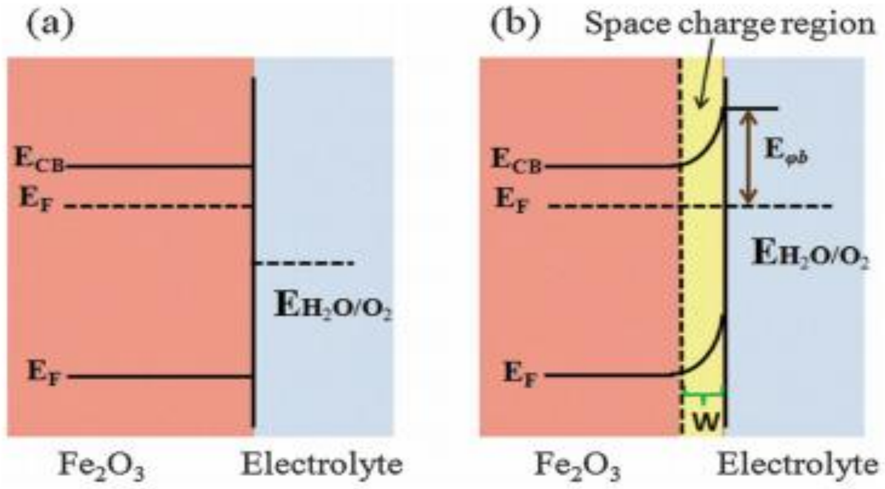

Figure 5: n-type semiconductor (Fe_2O_3) -electrolyte junction: E is the redox potential. (a) before chemical stasis (equilibrium); (b) after chemical stasis (equilibrium). The potential barrier height φb determines the maximum amount of energy that may be collected from a system [24].

This results in a build-up of negatively charged ions in solution (Helmholtz and Gouy layers) at the interface and depletion of electrons from the near-surface region of the semiconductor. At the interface, the (or space charge) is part of the electric double layer.

The charge separation (electrons and holes) at the junction causes an electric field, resulting in band bending across the space-charge layer, electrons (e^-) repel from the surface to the bulk and diffuse over the external circuit to the counter electrode because the positive charge carriers are forced to the surface by a stronger negative field, hence electrons have more energy at the surface than in the bulk. For a α-Fe_2O_3 photoanode in equilibrium with oxidation-reduction character in solution (O_2/H_2O), the electrode will have an excessive positive charge across the depletion width, and the solution will have an overload negative charge in the Helmholtz layer near the electrode [19]. The potential drop in the space-charge layer is determined by the difference between the Fermi levels of the solution and the semiconductor when it is free of excess charge, in this case, without band bending [24]. This potential is referred to as the flat-band potential. Any potential given to the electrode that is greater than the flat band potential causes the band to bend. This will lead to the depletion of charge carriers reaching the surface of the electrode. It should be noted that in nanostructured or particulate semiconductors, no band bending will occur if the particle size is smaller than the width of the space-charge layer [24].

Although various materials can undergo a photo-catalytically process to produce hydrogen, the efficiency of the overall energy conversion is still very low for application purposes. This is mainly because the three vital steps for the water splitting reaction are not fully addressed. Water splitting is the most thermodynamically challenging chemical reaction because it demands a multiple transfer of electrons. As a result, loading an appropriate co-catalyst for reduction and oxidation in semiconductors can significantly boost the activity of the PEC water splitting reaction in semiconductor-based photocatalytic and PEC systems [33].

1.6 Co-catalyst

In the process of PEC water splitting, the water oxidation reactions occur at the anode and cathode respectively, so co-catalyst loaded on these sites (electrode) of the semiconductor actively play as reactions sites [33]. The excited electrons/holes are accelerated to reaction sites by means of loading Co-catalysts on the surface of semiconductor [19].

Co-catalysts operate as trapping sites for active generated charge carriers by energy of photons and overcome the charge recombination. The approach of loading co-catalysts have been considerable established to improve the activity of a semiconductor with slow surface reaction kinetics [34]. In addition, co-catalysts reduce the electrochemical overpotentials associated with multielectron water oxidation, reduction reaction and also advance charge transfer across the semiconductor electrolyte interface [35]. The use of catalysts with a low adsorption energy and a high covalency of transition metal oxygen bonds could be a good technique [32]. Ruthenium oxide (RuO_2) and iridium oxide (IrO_2) are the best-known catalysts for water oxidation, while noble metals such as (Pt, Pd, and Ni) or transition-metal oxides are frequently used as a co-catalyst to forward the water reduction. Co-catalysts of this manner are normally used as nanoparticles (NPs), by impregnating the catalyst surface [35].

For photocatalytic water oxidation, compounds that are cobalt-based have also been forwarded as cocatalysts. The inexpensive and abundance of cobalt-based compounds have led to its selection when compared to iridium and ruthenium oxides.

Studies show that the use of cobalt phosphate (Co-Pi) for photoelectrochemical water oxidation has displayed an outstanding stimulation on α-Fe_2O_3 ativity, this includes an application of a major cathodic onset potential shift and a higher photocurrent density [34]. Co-Pi was shown to increase the life span of photogenerated holes and slow the charge carriers recombination [36]. In addition, the implantation of a Ru-based compounds catalyst in hematite improves the photocurrent, and bring about an efficiency that can sustain for at least 3 hours [33][18]. However, because the molecular catalyst may be photodegraded, the stability of the molecular catalyst to be used for a longer period of time may be a concern. According to a study of findings from several studies, the use of molecular catalysts in PEC water splitting has a lot of potential. [32].

The presence of a co-catalyst layer also acts as protect the electrode from photo-corrosion. The optimizing of co-catalyst is a vital task to avoid the likeliness of blocking the solar radiation from reaching the semiconductor by the co-catalyst, the thickness of the co-catalyst may also resist to function when it is too thick. As shown, the most recommended co-catalyst for the surface reaction is an exceptionally active co-catalyst that is inexpensive, light-tolerant, and easily manufactured on photoelectrodes. The co-catalyst may or may not have a defined structure with a high density of active sites and fine mass diffusion capabilities, or a consistent layer with high crystallinity, but it must be extraordinarily conductive to carriers such as metals or metal oxides with varied valence states [32], [37].

1.7 Aim and objectives

This work is designed to improve the photocatalytic properties of hematite α-Fe_2O_3 by doping transition metals (Cu, Ti, Ni and Mn). Mainly, reducing the band gap to enhance the absorption of α-Fe_2O_3 in the white light spectrum, thus, improve its conductivity. The objectives of this study are to:

- Determine the convergence parameters for hematite bulk system.
- Calculate structural, electronic, and optical properties by optimizing the α-Fe_2O_3 structure.
- Cleave low index surfaces from the bulk system and calculate properties of undoped surfaces.

- Dope α-Fe_2O_3 surface (001) and (101) with Cu, Ti, Ni and Mn by replacing one Fe atom.
- Perform electronic properties calculations for Cu, Ti, Ni, Mn doped α-Fe_2O_3 systems i.e., density of states and band structure.
- Calculate the optical properties for Cu, Ti, Ni, Mn doped systems i.e., absorbance, dielectric function, and conductivity.

CHAPTER TWO

2. Literature review

A semiconductor material with a value of 2.0 eV band gap is thought to be suitable for solar water splitting in classical physics. With this reflection hematite protrude as a best semiconductor for solar water splitting. In 2016, Tamirat *et al.* studied the development and problems faced with hematite for solar water splitting. The investigations showed that a calculated value of 2.1 eV band gap can theoretically have 15% efficiency of successfully converting solar-to-hydrogen (STH), which surpasses the required 10% measured STH efficiency for practical applications. However, the given theoretical STH efficiency benchmark is still not attained by practical efficiency [19]. Wheeler *et al*. also reviewed the synthesis and characterization of hematite, results reported that the short lifetime of charge carrier or has hindered the applicability of hematite to undergo PEC water splitting. Hematite nanostructures, doping and surface modification present the opportunity to beat some of the restrictions by improving the electronic and optical properties of hematite [38].

2.1 Hematite

2.1.1 Structural properties

Hematite (α-Fe_2O_3) is a hexagonal iron oxide crystal structure. It's thermodynamically stable, a semiconductor with a theoretical optical band gap approximately 2.0 eV [39], which allows absorption of wavelengths of up to 600 nm [24]. It is a recognized photoanode material because of its stability under water photolysis conditions. These features make hematite an admirable semiconductor to be used for photocatalytic activities. The cation Fe^{3+} found on both the valence band (VB) and the conduction band (CB) is determined by octahedral FeO_6 units contained in the crystal lattice. The VB can be adequately positioned in relation to the O_2/H_2O redox level in solution because VB is not dependable on the pH [40].

The crystal structure of α-Fe_2O_3 is described within $R\bar{3}c$ space group with a = b =0.5034 nm and c = 1.3752 nm lattice parameters [41]. The trigonal-hexagonal unit cells and the primitive rhombohedral unit cells are shown in Figure 6, a_{rh} = 0.5427 nm and α = 55.3 ° for the rhombohedral unit cell [42].

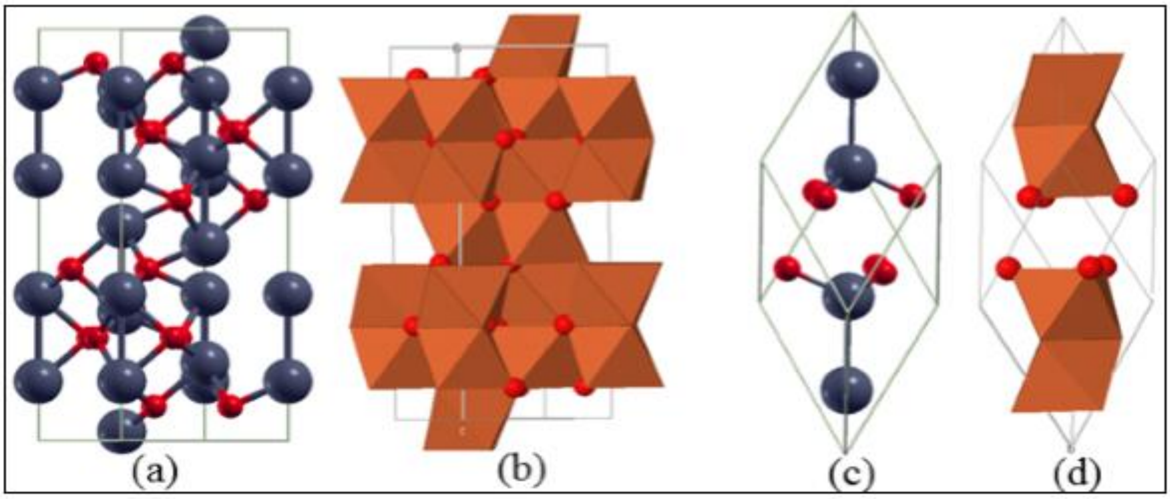

Figure 6: (a) The hexagonal unit cell and (c) the rhombohedral primitive cell of α-Fe_2O_3 is both represented. The face-sharing octahedra in (a) and (c) are depicted in (b) and (d) respectively. Fe is grey colour, while O is a bright red colour [42].

The hematite structure is easily understood based on the arrangement of the oxygen (O^{2-}) ions in the direction [001], they are packed in a hexagonal lattice with Fe^{3+} ions holding two out of three of the octahedral interstices in the hexagonal unit. Figure 5(b) display the understanding of the cations system pairs of FeO_6 octahedra that share edges with three adjacent and one face with the plane along the [001] direction.

The photo-electrochemical performance of α-Fe_2O_3 is unaffected by its magnetic properties; however, the iron spin configuration has an impact on its optical, electrical, and carrier transport capabilities. The characteristics should be accurately interpreted before it is used as a solar water splitting semiconductor. Multiple studies have shown that temperature and particle size are the main two factors that contribute to the magnetic properties of hematite, [42]. Hematite is weakly ferromagnetic at room temperature, and paramagnetic at temperatures above 956 K [19].

2.1.2 Electronic and optical properties

The theoretical energy band gap of a pure α-Fe_2O_3 semiconductor lies 1.9 and 2.30 eV, according to first-principles computation. The conduction band minimum (CBM) is primarily a contribution of the Fe 3d empty orbitals, while the valence band maximum (VBM) is generally made up of the Fe 3d and O 2p orbitals, with O 2p characters showing a predominant role of the electrons in this band. A pure hematite has the lattice parameters a = b = 5.07 Å and c = 13.88 Å [43]. According to Pendlebury [24], more recent soft X-ray spectroscopy and density functional theory (DFT) studies on the physical properties of α-Fe_2O_3 have indicated that the valence band consists of strongly hybridized Fe-d and O-p orbitals. While spectroscopic studies have suggested that the top of the VB is strongly hybridized. DFT calculations suggested that the band gap is primarily between Fe-d states, with the oxygen density of states being largely >1.5 eV below the top of the VB. Figure 7 shows a typical band structure of the α-Fe_2O_3.

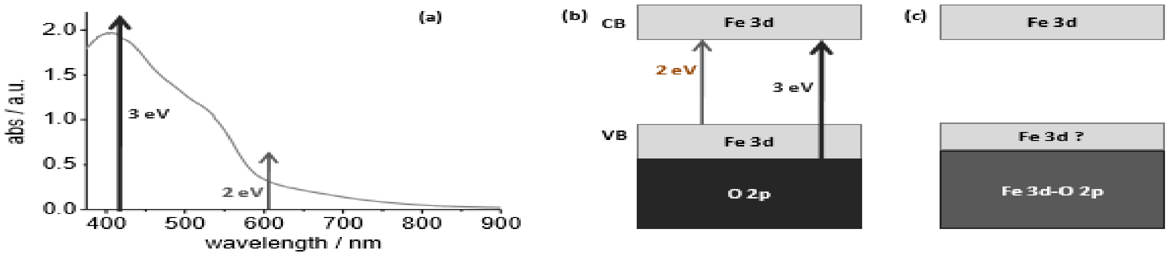

Figure 7: (a) Typical α-Fe_2O_3 absorption spectrum; (b) schematic of proposed α-Fe_2O_3 band structure; (c) hybridization of Fe 3d/O 2p VB [24].

Pendlebury [24] reported that unfortunately, the water oxidation efficiency of hematite under visible light is severely limited by this long absorption depth coupled with a short-hole diffusion length. The hole-diffusion length has been reported to be 2-4 nm and ~20 nm. This is an indicator of low mobility and/or rapid electron-hole recombination. Electron mobility in hematite is also thought to be low (0.01-0.1 cm^2.V^{-1}.s^{-1}). α-Fe_2O_3 films oriented with the basal plane perpendicular to the substrate have been reported to facilitate the collection of photogenerated electrons. Although the edge of the valence band lies below the O_2/H_2O redox potential of O2 / H2O and is suitable for water oxidation, the conduction band edge lies ~0.4 V positive of the H_2/H^+ potential, therefore a positive applied bias is necessary for the reduction of the proton to occur.

In the absence of impurities, a pure α-Fe_2O_3 exhibits poor electrical conductivity between temperatures 250 K and 960 K. This is under the impression that at this range low drift mobilities of charge carriers, is indispensable of thermal activation to jump between lattice sites [39]. Huda *et al.* [44] reported that, the weak optical absorption and very low electrical conductivity are the two main aspects which stand as an obstacle for α-Fe_2O_3 to fully perform in PEC application. Therefore, the electrical conductivity properties enhancement is a vital task for the future application of α-Fe_2O_3 in PEC activities. Adding impurities by means of doping has long been considered in studying the electrical transport properties of α-Fe_2O_3, this includes off-stoichiometric effects (oxygen vacancy) [45].

Meng *et al*. [46] studied the photo-electrochemical activities for Cu- and Ti-doped hematite using the first-principles, and the results showed that introducing Ti impurities in hematite extends the life of charge carriers and consequently improve the electrical conductivity of the semiconductor, hence, some of the photocatalytic properties of hematite have been enhanced when comparing undoped α-Fe_2O_3 and Ti-doped α-Fe_2O_3, . Results also estimated that doping Cu on hematite could improve the usage to ratio of solar energy and achieve an unprompted generation of hydrogen in the visible light impelled PEC water splitting occurring in the absence an external voltage bias.

Calculations indicate that Ti-doped-α-Fe_2O_3 generates minor donor level below the conduction band minimum; thereby, the energy band gap insignificantly gets narrowed by 0.34 eV [46]. As a result of this large shift in Fermi level, the peak positions of partial density of states (PDOS) move toward the lowest energy about 2.0 eV. Before entering the conduction bands, the Ti-doped Fermi level reaches a high energy level. Doping Ti and Cu in α-Fe_2O_3 broadens the range of energy in the conduction band and generates a split in Fe-3d and O-2p orbital energy due to the symmetry break in the crystal potential field. Doping Cu dopant generates an upward extension of the VBM because the function of introducing Cu impurities in hematite moderately simulates but is inferior to oxygen. In contrast to Fe, Ti dopant tends to be more ionized, lowering the energy required to join with oxygen, because it has a lower first ionization energy (1.07 eV lower).

Due to the enlarged locations of the conduction band generated by a shift of the band gap from the lower energy position to the higher energy position in Ti-doped hematite, the Fermi level (EF) enters the band gap, improving the contribution of electrons closer to the Fermi level.

Improving the conductivity of hematite for photocatalytic applications increases the life span of charge carriers, hence reduces rate of electron-hole pairs recombination, and advance an opportunity for charge carriers to take part in the reduction-oxidation reaction. Hypothetically, for Cu-doped- α-Fe_2O_3, the enhancement of the electrical conductivity could be a challenge due to localized electronic states around the Fermi level when E_F enters the valence band [46].

Huda *et al.* employed the Vienna ab initio simulation program (VASP) to investigate the properties of 3d transition metals doped in hematite in a recent DFT study. The study found that for a pure hematite the valence band maximum (VBM) is mainly a contribution has of O-2p and Fe-3d states and the conduction band minimum (CBM) has a mostly minor Fe-3d states [44]. Because of the orbital properties it holds, the structure of hematite has a CBM that is less dispersed in the first Brillouin zone. This is a demonstration that undoped hematite has excessively heavy carrier effective masses, resulting in low movement of the electrons. This is because electron carriers in α-Fe_2O_3 are confined due to the conducting phenomena and it is the given reason why α-Fe_2O_3 has low efficiency in converting solar-to-hydrogen even with a desirable band gap shown by the semiconductor. Huda and co-workers further explained that the properties of 3d transition metals ™ incorporated in α-Fe_2O_3 can be described using these inclinations:

In the case of Ti incorporated with α-Fe_2O_3, Ti substituted at Fe^{3+} site gives in a conduction band electron, this is because Ti^{4+} ion consist of four electrons in the outermost shell of its last energy level and favors a 4^+ charge state. The results also showed that, from the electronic band structure, the CB is fractionally occupied due to the added impurities. The Ti-4s and 3d states are added to the Ti-doped. The CBM becomes more spread out than that of pure α-Fe_2O_3, denoting that the introduction Ti orbitals may the reason why the effective mass of electrons is reduced, and the secondary (additional) n-type charge carriers (conduction electrons) will speed up electron transportation. Hematite has a higher electron affinity. The excess electrons will not confine in the centre of Ti impurities to create donor species but will be given to the iron atom. When compared to pure α-Fe_2O_3, the upshift of conduction band minimum do not undergo any significant alterations. However, the hybridization of O-2p and Ti-3d states have resulted in two levels of defects above the initial VBM. The calculated electronic properties of Ti-doped α-Fe_2O_3 gave 1.19 eV value, a reduced band gap in comparison of that of pure α-Fe_2O_3: consequently, this will ensure improvement of the low energy photon absorption. The results suggested that considering all the 3d transition metals, the incorporation of Ti would greatly accomplish an enhancement in electrical conductivity resulting an effective PEC performance.

In addition to the findings, they discovered that when doped to α-Fe_2O_3, some 3d transition metals give extra electrons and promote electrical conductivity, potentially increasing the efficiency of solar conversion for hydrogen generation by aiding for charge separation and transportation [44].

2.2 Doping

Doping is the process of adding impurities to alter the properties of the materials. Doping a semiconductor in a good crystal allows the introduction of energy states within the band gap. Doping is a well-established concept that has been shown to benefit several semiconductors by increasing carrier concentration in the bulk structure, and the enhancing the efficiency in the conductivity and charge separation. Dopants also have an important effect of shifting the energy bands relative to the Fermi level. It can change the electrical conductivity of the lattice and therefore vary the efficiency of the semiconductor [8]. Doping is regarded as a vital tool for modifying the electronic properties of metal oxides, it is also ideal for hematite photoanodes. Substituting a dopant element with high valence cations improves the electron concentration and the electrical conductivity in hematite [47].

According to Meng *et al.* [46], is was reported that the engineering of the band gap by metal doping, one should select a dopant (atom) that have similarities in the electronic structure but must be distinct in orbital energies to Fe 3d orbital. In this study, some of the first-row transition metals have been chosen as dopants (namely, Cu, T, Ni and Mn) because they have an electronic shell structure similar to that of Fe atoms.

An *et al*. [49] reported that transition metal oxide dopants have cultivated a lot of interest in theoretical and experimental research due to their distinctive properties. Metals such as Zn, Mo, Cr, Zr, Co, Ni, Rh, and Ti, have experimentally proven to play a significant role in improving photo-electrochemical activities of hematite. Previous reports stated that the first-principles studies on Co and Ni-doped hematite film result in a preferable performance than that of undoped α-Fe_2O_3 in PEC activities [49]. Transition-metal oxides form a group of predominantly ionic solids, which have a wide range of optical and electronic properties. Metallic dopants offer a wide range of distinctive properties than to non-metal doping. Metallic doping exhibits additional energy orbitals in energy the band gap, which brings about a new optical absorption edge and creates less of the energy boundary [23]. In general, electrode changes that increase the flow of electrons, concentration, and life span of charges participating in electrochemical processes can make photo-electrochemical systems involving transition-metal oxides more rational. Incorporation of cations into α-Fe_2O_3 displayed to have influence PEC performance through numerous procedures, adjusting the lattice parameters, raising carrier concentration, and overcoming charge recombination by increasing the electric field near the electrode-electrolyte interface [50].

Theoretical considerations and experimental observations in titanium doped hematite photoelectrodes were done by Kronawitter *et al.* [50]. The study indicated that DFT was the most common used method for investigating the semiconductor's electronic structure, however, using conventional DFT approaches to α-Fe_2O_3 had minor setbacks because of the localized Fe-3d electrons, which causes large errors when it is collaborative with the necessarily approximation of electron exchange-correlation (XC) functionals, the incomplete cancelation of Coulomb and exchange self-interaction terms are the reasons for such occurrence. The DFT+U technique replaces the inexact treatment of electron exchange with Hartree-Fock-like intra-atomic Coulomb (U) and exchange interaction terms for localized 3d electrons, according to the study. The Hartree-Fock theory has accurate electron exchange, and the DFT+U technique provides a transparent characterization of the first-row transition metal oxides and has been adopted in the α-Fe_2O_3 investigation. In 2015 Pan *et al.* reported that the incorporation of Zr into α-Fe_2O_3 is predicted produce more electron–hole pairs. Results also show that Zr-doped α-Fe_2O_3 exhibit a photocurrent density that is greater than that of undoped α-Fe_2O_3. Modifying α-Fe_2O_3 by introducing Co or Ni impurities result in a thermodynamically stable reaction route. This study also includes that substituting Rh for Fe can reduce the band gap of α-Fe_2O_3, thus lead to more absorption of solar radiation, it also improves the photocurrent over the wavelengths of 340 – 850 nm [43].

Gurudayal *et al.* [16] suggested that elemental doping of hematite could be constructive on the overall efficiencies of solar-to-hydrogen conversions. Examples of elements that were used in this study are Al, Cd, Mg, Mo, Mn, Si, Sn, Ti and Zn, for example, the atomic radius properties of Mn ions have made manganese a desirable dopant in α-Fe_2O_3. In the periodic table Mn is also closer to Fe, thus, their atomic radii are very close to each other, hence, will not yield any mishap in the α-Fe_2O_3 structure. Furthermore, because Mn can exist as Mn^{2+} and Mn^{4+} ions, it is a possible p- or n-type dopant. The trend of the results suggests that doping Mn can form energy states inside the band gap of α-Fe_2O_3, which could be useful in regulating electrical conductivity.

Simfukwe *et al.* [27] used DFT to investigate Cu-doped hematite surfaces for water splitting, and the results showed that Cu doped surface system can reduce the band gap and align the position of the conduction band to straddle with normal hydrogen electrode potential for direct water splitting. Meng *et al.* [46] used DFT+U to investigate the effects of doping Ti and Cu on hematite for improved PEC applications, and found that Cu-doped bulk hematite shifted the edge of the lower conduction band to high energy by around 0.5 eV, resulting in direct splitting water.

2.3 Hematite surfaces

The desirable properties exhibited by hematite for photo-electrochemical water splitting had since been on the quest to improve its efficiency for solar hydrogen production, electronic and optical of doped α-Fe_2O_3 were also investigated on surface structures as one way of enhancing the efficiency in converting solar to hydrogen. Research shows that there is an increase in the number of theoretical investigations carried out to describe the surface properties of α-Fe_2O_3 [42]. Using functional density theory, Wang *et al.* [51] calculated various possible structures of the surface of the hematite (0001). The (0001) surface structure has been reported by other theoretical groups regarding its interaction with water. Cui *et al.* [52] using first principles conducted a comparative study on the surface structure of sulfide and oxide minerals, results on the electronic structure of the surface of the hematite (001) suggest that the interactions of O and Fe are mainly in the areas of the valence band, and the sharp mixing peaks attributing to the orbitals of O-2p and Fe-3p, 3d and 4s orbitals show more characteristic of localization.

Bulk doping has been shown to boost the photocatalytic activity of α-Fe_2O_3, but it also introduces localized impurities that can behave as undesirable electron-hole pair recombination hotspots. Surface doping is thought to be more advantageous than bulk doping because it minimizes the distance traveled by charge carriers and also reduces fast recombination, resulting in more effective use of the charges [27].

CHAPTER THREE

3.1 Theoretical Methodology

3.1.1 Schrodinger equation

The Schrodinger equation is a fundamental physics equation that describes a system's quantum mechanical behavior. It's a partial differential equation that describes how a physical system's wave function evolves over time. The following is the time-dependent one-dimensional Schrodinger equation:

$$i\hbar\frac{\partial\varphi(r,t)}{\partial t} = H\varphi(r,t) \tag{4}$$

H is the Hamiltonian operator defined as:

$$H = \left(-\frac{\hbar^2}{2m}\ \ \nabla^2 + V\right) \tag{5}$$

where $\hbar$ is the Planck's constant divided by 2π and m is the mass of the electron, φ is a wavefunction, r is the position, t is the time where ∇^2 is the Laplace operator and V is the potential energy. When the Hamiltonian operates on a wave function, it gives the energy of the wavefunction.

$$\left(-\frac{\hbar^2}{2m}\ \ \nabla^2 + V(R)\right)E(k)\varphi(r,k), \tag{6}$$

The band structure of a crystalline solid, that is, the energy-momentum (E-k) relationship, is usually obtained by solving the Schrodinger equation of an approximate one-electron problem [54],[55].

3.1.2 Density functional theory

Density functional theory (DFT) is a computational quantum mechanical modelling method used to investigate the electronic structure of atoms, molecules, and the condensed phase of many-body systems known as the ground-state electron density.

The DFT can be used to determine the properties of a many-electron system using functionals, which in this case is the spatial-dependent electron density. In addition, DFT is computationally versatile,

it has been broadened to include spin polarized systems, multicomponent systems like nuclei and electron hole droplets, free energy at finite temperatures, superconductors with electronic pairing mechanics, relativistic electrons, time-dependent phenomena and excited states, bosons, etc. [56]. As a result, DFT is frequently used in first-principles computations to describe and predict properties of molecular and condensed matter systems.

3.1.3 First-principles calculation

In any case, quantum mechanics gives a dependable approach to figure out provides what electrons and atomic nuclei do in any given environment. Most of a material's qualities are determined by electron behavior. Because quantum mechanics describes and explains chemical bonds, this is true for a single atom or assemblages of atoms in condensed matter. As a result, by solving the Schrodinger equation for the electrons in any substance, the properties of that material may be understood, that is, based on fundamental physical laws and without the use of free parameters. Electrons interact intensely with each other, causing rapid complications. In simple potentials, it only exists for a single electron, which is frightening. First-principles techniques recast the problem from one in which electron interactions are consider to one in which they are not for practical computations on condensed materials [57]. The interactions take place are in the effective potential, and one electron at a time is dealt with. The result is a series of Schrodinger-like equations for one electron:

$$H\psi_n = \left(-\frac{\hbar^2}{2m} \nabla^2 + V_{ext} + V_{eff}\right)\psi_n = e_i\psi_n, \tag{7}$$

The n one-electron wavefunctions are denoted by ψ_n , V_{ext} is the nuclei's external potential, and V_{eff} is the effective potential.

The ground and excited state properties of a many-electron system in the presence of an external field can all be derived accurately from the ground state density according to Kohn-Sham [58]. The external potential $\mathrm{V_{ext}(r)}$ is a unique functional of $\rho(r)$ according to Hohenberg and Kohn and since $V_{ext}(r)$ fixes H, the Hamiltonian is the unique functional of the electron density. The Hamiltonian for many electrons is given by [59]:

$$H = T + U + V \tag{8}$$

where the parameter T is the kinetic energy, U is the potential energy term indicating the electrons interacting with the nuclei, and V is the external potential (V_{ext}). The electron density $\rho(r)$ is defined as:

$$\rho(r) = \Psi^*(r_1, r_2, r_3, \dots, r_N)\Psi(r_1, r_2, r_3, \dots, r_N) \tag{9}$$

Thus, $\rho(r)$ determines $V_{ext}(r)$ and hence all the properties of the ground state, for example the kinetic energy $T[\rho]$, the potential energy $V[\rho]$,, and the total energy $E[\rho]$. The ground state energy E is a unique functional of the electron density, thus total ground state energy is given as: [60]

$$E = E[\rho(r)] \tag{10}$$

The electron density is all that is required to define the total ground state energy. The electron density that minimizes the energy of the overall functional is the true ground state electron density. This brings knowledge of how to find the ground state energy.

$$E[\rho(r))] > E_0[\rho_0(r)] \tag{11}$$

The energy functional consist of two main parts, the known and the unknown energy.

$$E[\{\Psi_i\}] = E_{known}[\{\Psi_i\}] + E_{XC}[\{\Psi_i\}] \tag{12}$$

The known energy term is given by:

$$E_{known}[\{\Psi_i\}] = -\frac{\hbar}{m_e}\sum_i \int \Psi_i{}^{*}\nabla^2\,\Psi_i d^3r + \int V(r)\rho(r)d^3r + \frac{e^2}{2}\int\int \frac{\rho(r)\rho(r')}{r-r'}d^3rd^3r' + E_{ion}$$

(13)

The unknown energy term $E_{XC}[\{\Psi_i\}]$ is known as the exchange correlation functional and it takes care of all the quantum mechanical interactions between electrons. It includes all quantum mechanical terms, and it is not known but needs to be approximated.

3.1.4 Exchange correlation functionals

The local density approximation (LDA) which was proposed by Kohn and Sham along with the KS equations, is the most extensively used approximation. According to the LDA, E_{XC} can be calculated by assuming an infinitesimal element of density ρdr, the exchange-correlation energy is that of a uniform electron gas of density $\rho = \rho r$ Then [61],

$$E_{XC} = \int \rho(r)\epsilon_{xc}(\rho(r))\,dr \tag{14}$$

In LDA method, only the electron density (ρ) at point r is considered for the approximation of the exchange correlation energy, the gradient of the density $\nabla\rho$ is not utilized to approximate the exchange correlation energy, this led to the development of generalized gradient approximation (GGA) method. The GGA improves predicted binding and dissociation energies, especially for hydrogen-containing systems. Although there are various GGAs, one of the most employed is the GGA by Perdew, Burke, and Ernzerhof (PBE) [62]. GGA-PBE is the default exchange-correlation functional. It is recommended, especially for studies of molecules interacting with metal surface, although it is also reliable for bulk calculations. GGA provides a better overall description than the LDA functionals.

3.1.5 The Kohn-Sham scheme

Kohn and Sham introduced an approach for minimizing the functional cost based on the Hohenberg-Kohn theorem $E[\rho(r)]$ by varying $\rho(r)$ over all densities containing N electrons [63]. This constraint is introduced by the Lagrange multiplier μ chosen so that $\int \rho(r)dr = N.$

$$\frac{\delta}{\delta\rho(r)}[E[\rho(r)] - \mu \int \rho(r)dr] = 0 \qquad (15)$$

$$\Rightarrow \mu = \frac{\delta E[\rho(r)]}{\delta\rho(r)} \qquad (16)$$

Kohn and Sham chose to separate $F[\rho(r)]$ into three parts, so that $E[\rho(r)]$ becomes:

$$E[\rho(r)] = T_s[\rho(r)] + \frac{1}{2}\int\int \frac{\rho(r)\rho(r')}{|r-r'|}drdr' + E_{XC}[\rho(r)] + \int \rho(r)V_{ext}(r)dr \qquad (17)$$

where $\mathrm{T_s}[\rho(\mathrm{r})]$ is defined as the kinetic energy of a non-interacting electron gas with density $\rho(r)$ and is given by:

$$T_s[\rho(r)] = -\frac{1}{2}\sum_{i=1}^{N}\int \Psi_i^*(r)\nabla^2\Psi_i(r)dr \qquad (18)$$

Equation 18 also acts as a definition for the exchange correlation energy functional$\mathrm{E_{XC}}[\rho(\mathrm{r})]$. We can rewrite equation 20 in terms of an effective potential $\mathrm{V_{eff}}(\mathrm{r})$ as follows:

$$\frac{\delta T_S[\rho(r)]}{\delta\rho(r)} + V_{eff}(r) = \mu \qquad (19)$$

where

$$V_{eff}(r) = V_{ext}(r) + \int \frac{\rho(r')}{|r-r'|}dr' + \frac{\delta E_{XC}[\rho(r)]}{\delta\rho(r)} \qquad (20)$$

Now, if one considers a system that really contained non-interacting electrons moving in an external potential equal to $V_{eff}(r)$ as defined in equation 19, then the same analysis would lead to the same equation. Therefore, to find the ground state energy and density, E_0 and $\rho_0(r)$ all one must do is to solve the one electron equations:

$$\left(-\frac{1}{2}\nabla_i^{\,2} + V_{eff}(r) - E_i\right)\Psi_i(r) = 0 \qquad (21)$$

As the electron density is constructed according to the equation:

$$\rho(r) = \sum_{i=1}^{N} |\Psi_i(r)|^2 \qquad (22)$$

These equations must be solved with self-consistently scheme [63].

1.3.6 Self-consistency scheme to finding the ground state

The wave functions are expressed on a planewave basis when finding the ground state in calculations, and these are sampled at a discrete number of k-points. The ground state is found by iteratively improving an initial guess until the change in energy differences is small to make sure the structure converges as shown in Figure 7. The scheme consists of 4 steps and are as follows:

Step 1. Guess the electron density: trial $\rho(r)$

Step 2. Solve the Kohn-Sham equations with $\rho(r)$, obtain single electron wave functions $\Psi_i(r)$

Step 3. Calculate the electron density based on the single-electron wave functions

$$\rho(r) = 2\sum_i \Psi_i^{\,*}(r)\Psi_i(r) \qquad (23)$$

Step 4. Compare the new electron density $\rho(r)$ with the initially approximated electron density $\rho(r)$ from step 1.

There are two conditions to consider before concluding about the electron density,

a. If the new density is different from the approximated density, begin with the new electron density as the approximated and repeat the whole procedure from step 1.

b. If they are both the same, then that means true ground state electron density has been obtained.

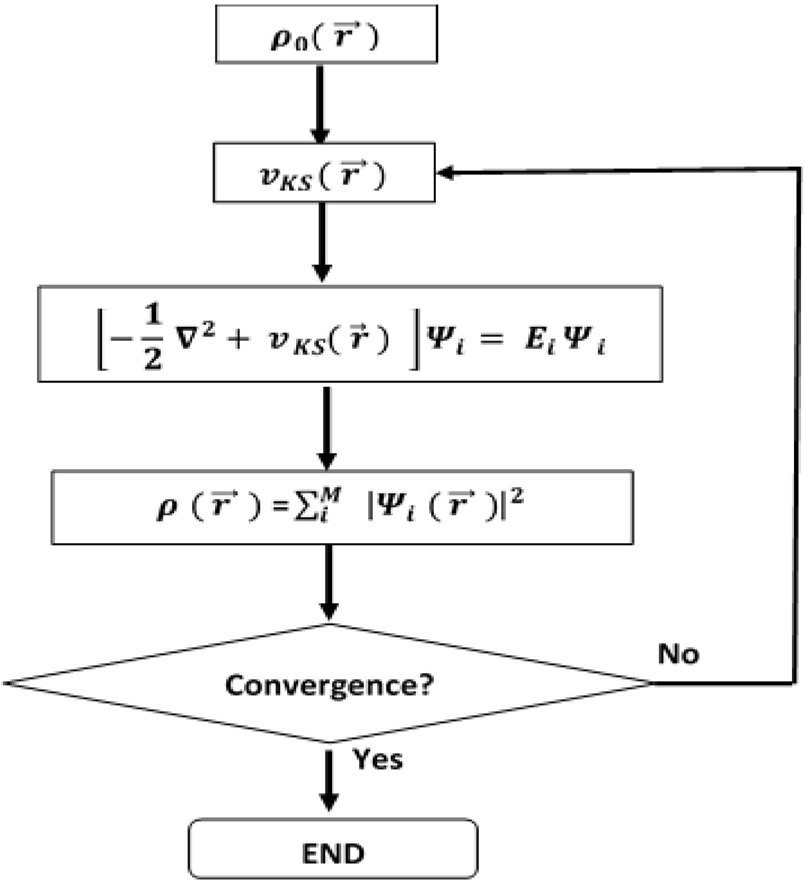

Figure 8: Flow chart of a typical DFT calculation within the Kohn-Sham method [64].

The above formulation assumes that the exchange-correlation functional is known. At present numerical exchange correlation potentials have only been determined for a few simple model systems, and so most current density functional calculations use the Local Density Approximation (LDA). The LDA approximates the XC functional to a simple function of the density at any position r. The value of this function is the XC energy per electron in a uniform homogeneous electron gas of density $\rho(r)$. The LDA expression for $E_{XC}[\rho(r)]$ is given by:

$$E_{XC}[n(r)] \approx \int E_{XC}(\rho(r))\rho(r)\,dr \tag{24}$$

The LDA is remarkably accurate, but often fails when the electrons are strongly correlated as in systems containing d and f orbital electrons [65], [63].

3.2 Pseudopotentials

The concept of a pseudopotential is related to replacing the effects of the core electrons with an effective potential. The pseudopotential generation procedure starts with the solution of the atomic problem using the Kohn-Sham (KS) approach [59]. This approximation is well known and provides a number of computational benefits, including fewer electronic states in solid-state calculations, smooth and node-free pseudo-wave functions in the core region, efficient representation of both pseudopotentials and pseudo-wave functions using a plane wave basis set, and the pseudopotential is much weaker in the core region than the true Coulomb potential of the nucleus. [66]

3.2.1 DFT Plane wave basis set approximation

The plane-wave pseudopotential approach uses the plane-wave basis set to represent the orbitals. The wave function can be written as the product of the cell periodic part and a wavelike part:

$$\Psi k_i(r) = e^{ik.r} f_i(r) \tag{25}$$

The first term is the wave-like part, and the cell periodic component of the wave function is the second term. This can be described by dividing it into a finite number of planewaves, the wave vectors of which are reciprocal crystal lattice vectors, as follows:

$$f_i(r) = \sum_G G_{i,G} \ e^{iG.r} \tag{26}$$

where G represents reciprocal lattice vectors given by $\mathrm{G}.I \ = 2m\pi$ for I, where I is a lattice of the crystal and m is an integer [67]

3.3 Cutoff

A cut-off energy only includes plane waves with energies less than the cut-off, and is defined as:

$$E^{cut} = \frac{\hbar}{2m} |G|^2 \tag{27}$$

The cut-off energy must always be high enough to give accurate results. This can be achieved by repeating the calculations with higher and higher cut-off energies until the properties have converged.

3.4 K-points sampling

Bloch’s theorem eigenstates in a system under a periodic potential $U(r)$ can be written as:

$$\psi_i(\vec{r}_{;}\vec{k}) = e^{i\vec{r}\cdot\vec{k}} U_{i_i}(\vec{r}\cdot\vec{k}) \tag{28}$$

Operators such as the Hamiltonian are block-diagonal by *k*-point:

$$\begin{matrix} h_{ki} & 0 & 0 \\ 0 & h_{k2} & 0 \\ 0 & 0 & h_{k3} \end{matrix} \tag{29}$$

It is important to describe waves and correlation lengths longer than the unit cell in solids (especially conductors/ semiconductors, when only the point is sampled (*k =0)*

$$\psi_k(r) = e^{i(k.r)} U_k(r) \tag{30}$$

where $U_k(r+L) = U_k(r)$ and $e^{i(k.r)}$ are arbitrary phase factor

$$\psi_k(r+L) = e^{ik(r+L)} U_k(r+L) \tag{31}$$

$$e^{ik.L}\psi_k(r) \tag{32}$$

In principle, we need to integrate overall possible k-points when constructing the density. Fortunately, the wave functions change slowly as it’s varied, such that the integral is approximated with a summation.

$$P(r) = \int |\psi_k(r)|^2 \, d^3k \tag{33}$$

$$P(r) = \sum_k |\psi_k(r)|^2 \tag{34}$$

To get more accurate results, enough k-points must be used.

3.5 Computational software

3.5.1 Material studio

Material studio is a comprehensive modeling and simulation environment that enables researchers in a variety of domains to predict and comprehend the links between atomic and molecule structure, characteristics, and behavior. Researchers from a variety of industries are using the material studio to create higher-performing materials of various kinds, including medicines, catalysts, polymers, composites, metals and alloys, batteries and fuel cells, and more. [68]. Cambridge Serial Total Energy Package (CASTEP) is a component of the material studio software that allows us to execute density functional theory calculations

3.5.2 Cambridge Serial Total Energy Package

CASTEP is a program that calculates the electrical characteristics of crystalline solids, surfaces, molecules, liquids, and amorphous materials from first principles, using density functional theory and a set of plane wave basis. The sole limitation is the finite speed and memory of the computers being used to calculate the properties of any material that can be conceived of as an assembly of nuclei and electrons.

Surface chemistry, structural properties, band structure, density of states, and optical properties are only a few examples of typical uses. CASTEP can also be used to investigate the spatial distribution of a system's charge density and wave functions, as well as the properties of point defects (vacancies, interstitials, and substitutional impurities) and extended defects (grain boundaries, for example) in semiconductors and other materials. [68].

3.6 Computational Procedures

The geometry optimization calculations have been performed using the CASTEP code, which employs a basis set of plane waves to solve the Kohn-Sham equations of the density-functional- theory (DFT) [69].

Both the localisation of valence states and the mixing of oxygen p states and iron d states (exchange-correlation energy) of -Fe_2O_3 were studied in this study and the Perdew-Burke-Ernzerhofer (PBE) functional was used to parameterize the generalized gradient approximation (GGA) functional. For the electron-ion interaction, PBE's Ultra-Soft Pseudo potentials were used. GGA+U calculations was also adopted to account for the strong on-site Coulomb repulsion of the Fe-3d electrons $U = 5$ eV proposed by Dudarev *et al.* [70], [71]. Because this interaction parameter is relatively controllable, the DFT+U approach can be used to provide a qualitative assessment of the influence of electronic correlations on a system's physical properties. [72].

To acquire precise energies for all systems, 650 eV convergent plane-wave cut-off energy was utilized, which ensured an accurate description of attributes that are influenced by sharp features in the density of states. The Brillion zone was sampled using a Monkhorst-Pack mesh k-points of 4x4x2 for both bulk and surface calculations with a spacing of 0.07 $Å^{-1}$ for the calculations of density of states (DOS) and partial density of states (PDOS). A fermi smearing of 0.1 eV was utilized to speed up convergence.

The bulk structure of α-Fe_2O_3 was imported from examples of metal oxides within the material studio, α-Fe_2O_3 is a hexagonal cell, at a fixed experimental cell parameters values of a=b=5.035 Å and c=13.720 Å, and an angle between vectors of $\alpha = 90^{\circ}$. In a deformed octahedron, each Fe is coordinated by six oxygen atoms, while each O has four Fe neighbors. This research used a hexagonal lattice with three primordial cells (24 Fe atoms and 20 O atoms). Each layer of Fe atoms in the hexagonal lattice (Figure 11) is separated by a plane of O atoms. This allows for the creation of Fe-layer terminated surfaces.

To investigate the consequences of doping, two surfaces were cleaved from the bulk structure of hematite with cleave plane (*h, k, l*) taking numbers (001), and (101), the surfaces were set to a slab thickness of 8.003 Å and 8.624 Å, for surfaces (001) and (101) respectively. To avoid interaction between the slabs, a vacuum region of 15 was tested as sufficient. For calculations of optical and electronic properties, the band energy tolerance was set at $1.0X10^{-5}$ eV with the energy tolerance per atom while the separation was 0.025/Å . The choice α-Fe_2O_3 (001) and (101) was influenced by a study on the comparative surface structure of minerals of sulfur and oxides minerals by Cui *et al.* [52].

For element doping, one of the Fe atoms was substituted by one of the dopants (Cu, Ti, Ni, and Mn); calculations for the electronic and optical properties were carried out for all the surfaces. The calculated results were compared with the results of recent theoretical research for consistency.

3.7 Calculated properties

3.7.1 Adsorption energy of atoms at α-Fe_2O_3 semiconductor surface

Four transition metals, Cu, Ti, Ni, and Mn were doped in the surface structures (001) and (101) by substituting one Fe atom. The adsorption energies of the two α-Fe_2O_3 surfaces were calculated using equation (32) below:

$$E_{ads} = E_{surf} + E_{atom} - (E_{surf+atom}), \tag{35}$$

E_{atom} is the energy of the adsorbate, while E_{surf} is the energy of the α-Fe_2O_3 slab surface, and $E_{surf+atom}$ is the total energy of the slab with the atom in vacuum gap's centre, where the interaction with the surface is minimal. This method effectively wipes out the minor contributions from lateral interactions between the atoms, as well as inaccuracies from the two terms on the right-hand side of the equation. By definition, a positive value of $E_{ads} > 0$ indicates stable adsorption [73-75].

CHAPTER FOUR

4. Results and Discussions

In this chapter, the first-principles density functional theory (DFT) and density functional theory with Hubbard potential (DFT+U) were employed to study the molecular structures of the bulk hematite, geometric optimization, and electronic and optical properties, hence, proceeding with a method yielding better performance for application in PEC water splitting.

4.1 Geometric optimization

To obtain the optimal condition at which α-Fe_2O_3 is more stable, the cutoff energy and the corresponding k-points were determined by optimizing the bulk structure of α-

Fe_2O_3. The usage of such locations merely causes the periodic function to expand in reciprocal space functions with the necessary symmetries, bringing us closer to the origin (0,0,0) [76]

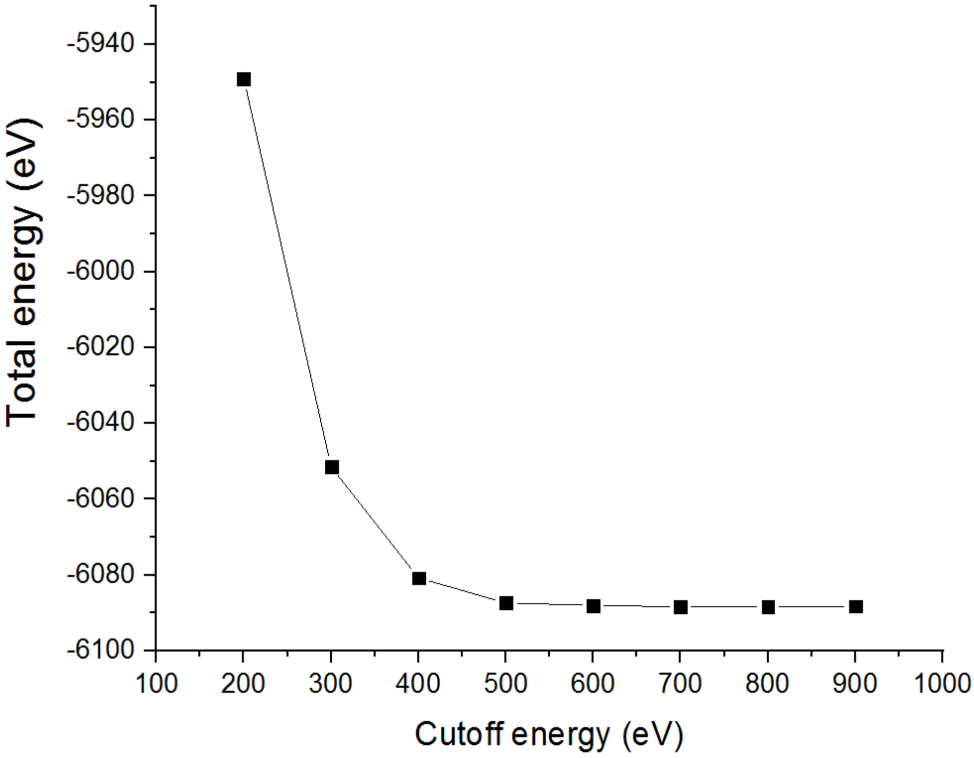

Figure 9: Total energy against plane wave basis set cut-off.

We perform this convergence test for the total energy against the cut-off energy. It can be seen from Figure 9 that when the cuff energy is increased to 600 eV, the total energy begins to converge, so it is believed that the 650-eV calculation result of the cutoff is credible and was chosen to be the ground state energy for all calculations. When compared to the work of Pan *et al.* [77] the cutoff energy of 550 eV using VASP first-principles simulations for synthesis by water splitting on hematite surface (0001), this is fairly near cutoff energy.

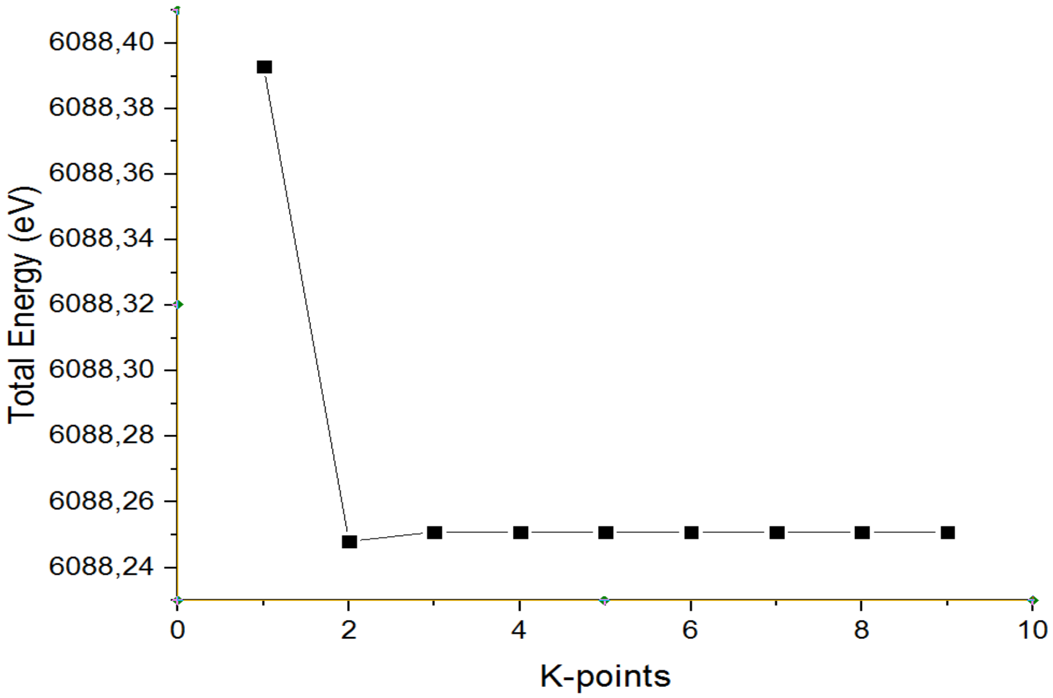

Figure 10: Graph of energy formation versus the number of k-points.

Figure 10 shows the how the number of k-points that gave the lowest total energy were obtained. At energy 6088,25 eV, 4 k-points are obtained, and this corresponded to 4x4x2 for the Brillouin zone integration and observing from the graph it was constant and stable at that point and onwards. Henceforth, all the geometry optimization and properties calculations for the bulk system were performed using 650 eV cut-off energy and 4x4x2 of k-points. Also, possibly k-points 5x5x2, 6x6x2. could be used since they lie along the same curve for the Brillouin zone sampling and this is similar to the used k-point of 5x5x2 for surface unit cell used by An *et al.* on the First-principles study of sulfur atom doping and adsorption on α–Fe_2O_3 (0001) film [49].

4.2 Pure α-Fe_2O_3 bulk structure:

4.2.1 Electronic properties of bulk α-Fe_2O_3

In ambient settings, α-Fe_2O_3 is the most thermodynamically stable form of iron oxide, and it is also the most prevalent form of crystalline iron oxide. The α-Fe_2O_3 structure contains iron (Fe) atoms and oxygen (O) atoms arranged in a hexagonal structure.

The valence d-orbitals of each Fe atom have spatially localized open-shell electrons. The electrons are highly interacting because six oxygen atoms surround the Fe atoms, causing d-orbitals to divide in the crystal field and create groups of degenerate orbitals. [78]. Figure 11 shows the primitive hexagonal unit cell of α-Fe_2O_3.

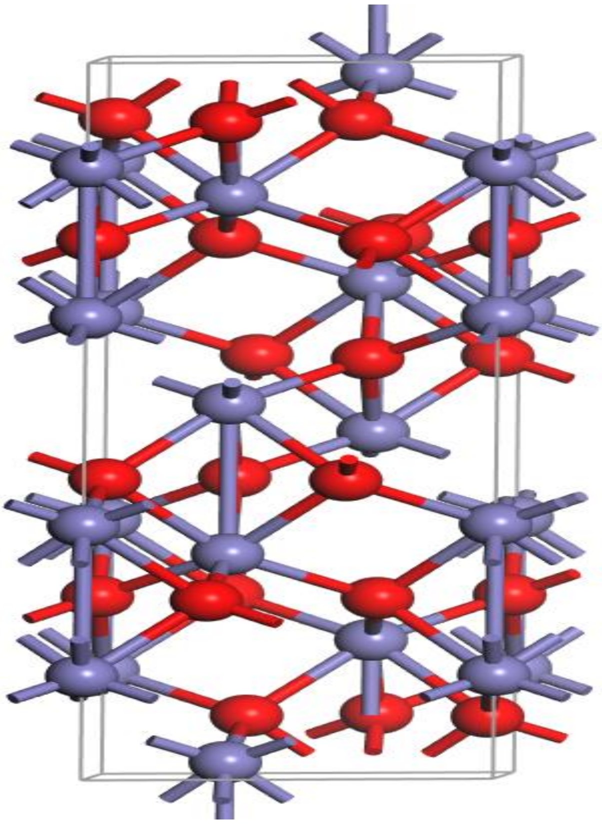

Figure 11: Hexagonal cell for α-Fe_2O3, red representing O and Fe represented by grey.

We estimated the density of states (DOS) and the band structure of a pure α-Fe_2O_3 to explain its electrical properties. Figure 12 depicts the band structure of α-Fe_2O_3 and includes a visualization of the computed density of states. The valence band (VBM) is dominated by O-2p and Fe-3d electrons at lower energy levels, with O-2p electrons playing a prominent role. The Fe-3d states peaks near the minimum Fermi level, while the conduction band minimum (CBM) is characterized by a minority of O-2p states at different energy levels. These orbital features shifted above the Fermi level have resulting in a 2.43 eV energy band gap. This simply demonstrate the existence of localized states, which could be owing to the fact that α-Fe_2O_3 has exceptionally heavy carrier effective masses, resulting in limited electron mobility. Even with a favorable band gap of α-Fe_2O_3, due to these reasons, the efficiency of successfully converting solar to hydrogen is always very low. These findings are in line with earlier theoretical work that suggests α-Fe_2O_3 possesses a valence band dominated by O-2p states and Fe-3d levels. [42].

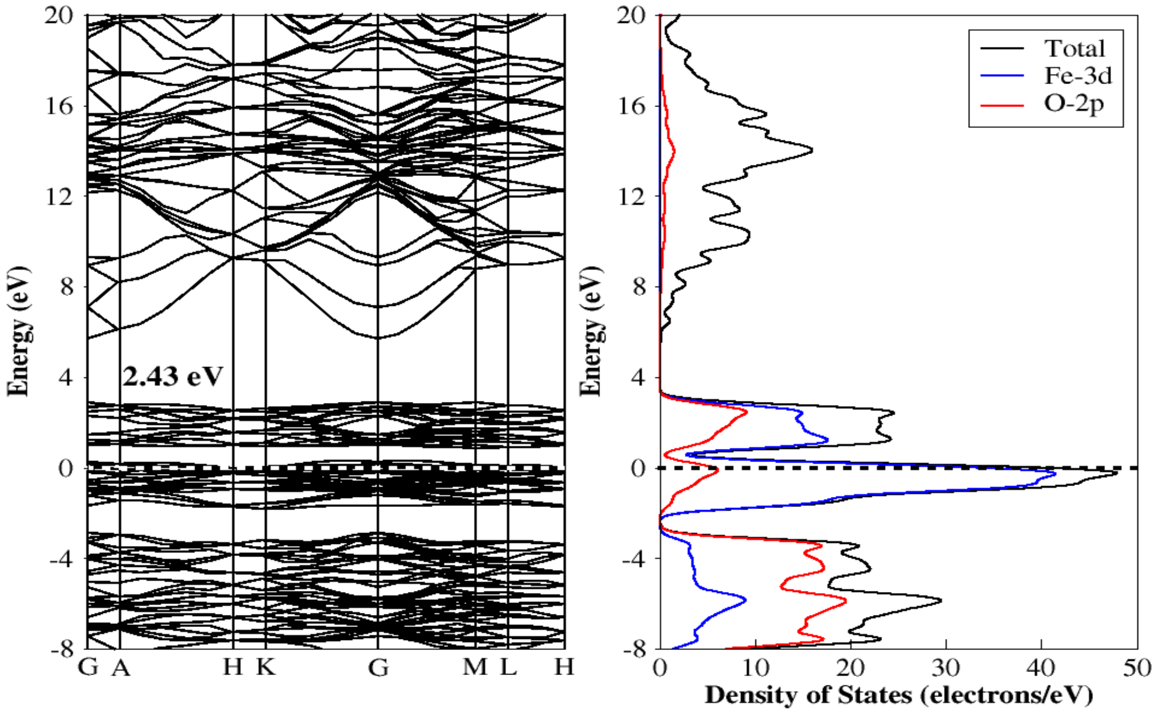

Figure 12: Bulk α-Fe_2O_3 band structure and DOS plot using DFT.

Table 1 summarizes the structural properties observed in this study in comparison to previous theoretical and experimental literature. The predicted band gap using DFT for the band structure (Figure12) is 2.43 eV, which is quite close to prior experiments. The Fe d electrons have a significant Coulomb repulsion on-site [70], hence, the electronic characteristics of the bulk structure were also calculated using DFT+U. The DFT+U method is named after its simple method for accounting for underappreciated electronic interactions, which involves merely adding a semi-empirically tuned numerical parameter "U." The U correction's primary function is to add an additional Hubbard-like component to the strong on-site Coulomb interaction of localized electrons. This "U" correction can be added to the local and semi-local density functionals, enabling LDA+U and GGA+U computational procedures. The Hubbard describes the strongly correlated electronic states (d and f orbitals), while handling the rest of the valence electrons by the conventional DFT approximations [72]. Meng *et* *al.* used a value U= 5 eV [46], we followed this trend and U was set to be U= 5 eV. Figure 13 is a representation of the band structure of bulk α-Fe_2O_3 using DFT+U.

Table 1. Band gap and lattice parameters for optimized bulk α-Fe_2O_3 compared with literature and theoretical studies.

	This work		Theoretical [79]	Literature [43]
	DFT	DFT+U		
Band gap (eV)	2.43	1.889	1.9 – 2.2	2.30
Lattice parameters (Å)	a = b =5,174 c= 13.985	a = b =5,137 c= 13.684	a=b=5.035 c=13.748	a=b=5.07 c=13.88

Figure 13 shows the electrical parameters determined using DFT+U, which provide a fair description of the band gap and compare well to the results of other recent theoretical studies (Table 1). A calculated value of 1.889 eV, falls within the theoretical range of (1.9- 2.2eV) [19], thus, the DFT+U method give a reasonable prediction of the theoretical band gap.

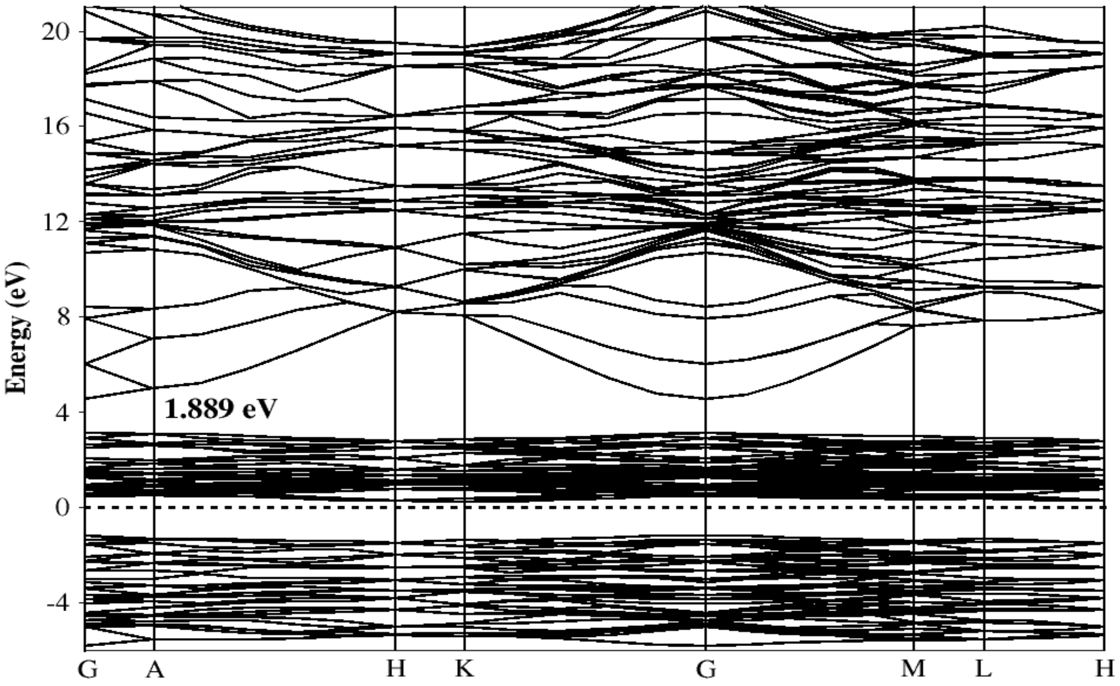

Figure 13: The band structure for bulk α-Fe_2O_3 using DFT+U.

4.2.2 Optical properties for bulk α-Fe_2O_3

4.2.2.1 DFT Method

Other than electronic qualities, optical properties such as dielectric function, refractive index, reflectivity, loss function, absorption coefficient, and conductivity can be highlighted. The optical of a semiconductor show the interaction between photons and the semiconductor. In this section, we look at the absorption spectrum, dielectric function, reflectivity, and conductivity for bulk α-Fe_2O_3, including the selected surfaces. A study using a first-principles approach calculated the optical properties of hematite to better comprehend its role and limitations in photo-electrochemical cells, thus by far fewer theoretical studies on optical properties have been conducted [78]. Figure 14 shows the optical properties plotted against wavelength and frequency.

The complex dielectric function, which can be expressed by the formula below, is connected to these optical properties.

$$\varepsilon(\omega) = \varepsilon_1(\omega) + i\varepsilon_2(\omega) \tag{36}$$

The real and imaginary components are denoted by $\varepsilon_1(\omega)$ and $\varepsilon_2(\omega)$ is, respectively. The actual part is tied to the material's electronic polarizability, whereas the imaginary part is related to the material's electronic absorption. The following relationship can be used to define the imaginary component of the dielectric function:

$$\varepsilon_2(h\omega) = \frac{2\pi^2}{\Omega\varepsilon_0} \sum_{k,v,c} \left| \langle \psi_k^C | u.r | \psi_k^v \rangle \right|^2 \delta(E_k^c - E_k^v - E) \tag{37}$$

where e denotes electronic charge, u denotes incident electric field and ψ_k^v and ψ_k^c denotes valence band and conduction band wave functions at the k point, respectively. To get the real component of a dielectric function from the imaginary part, utilize the Kramers-Kronig transformation. [80].

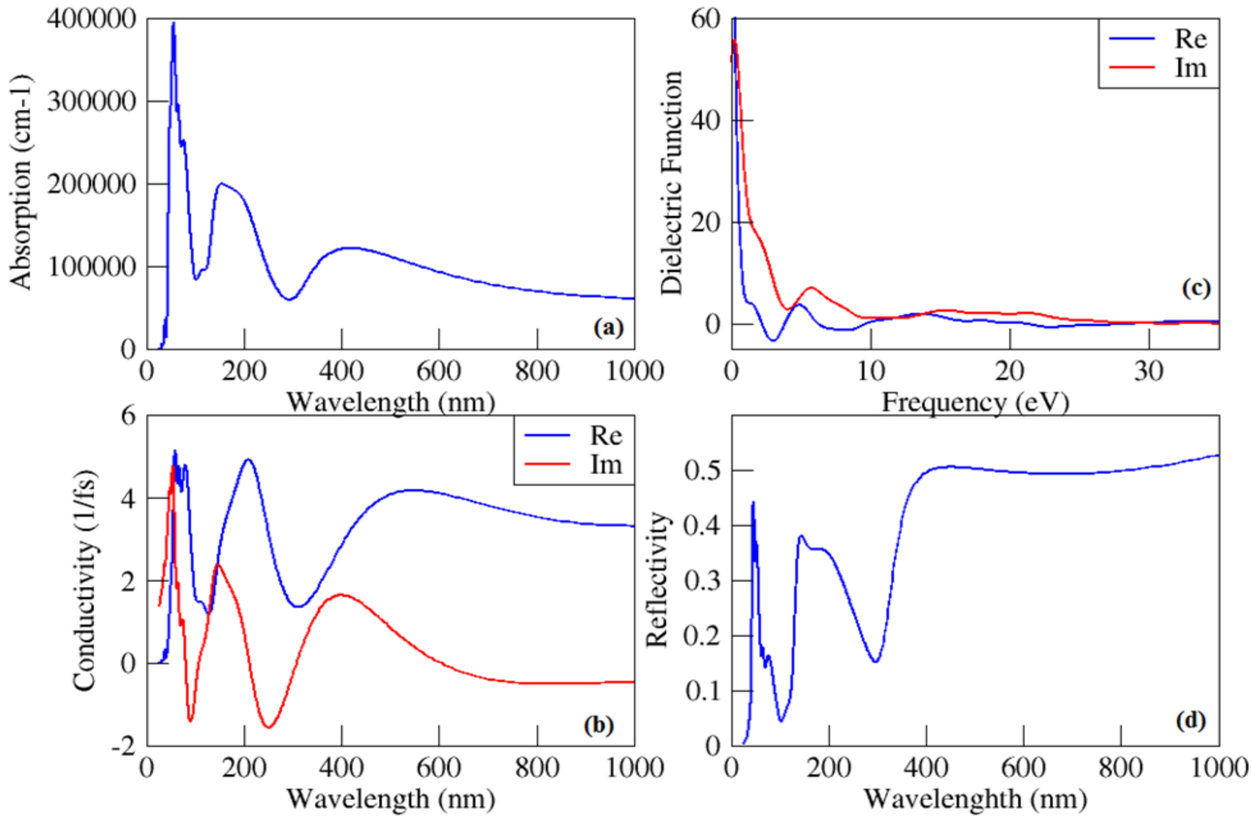

Figure 14: Optical properties: (a) Absorption spectrum, (b) conductivity (c) dielectric function and (d) reflectivity for bulk α-Fe_2O_3 using DFT.

The real part and imaginary parts of the dielectric function of hematite up to a photon frequency of 35 eV from DFT calculations are represented in Figure 14 (c). The real part shows the first energy peak at about 4 to 5 eV, and maintains a straight line with the increasing frequency, however, at 4 eV, there is a major drop for both the imaginary and real dielectric function. From 4 eV to a decreasing frequency there is an increase for both real and imaginary dielectric functions, therefore, we could say that both the imaginary and real parts decrease with increasing frequency. On the other hand, the real part there is a highest peak from around 1.5 to 2 eV, which is the most admirable energy for semiconductors used for solar cells.

The following relationship can also be used to calculate the absorption coefficient $\alpha(\omega)$ from the dielectric function:

$$\alpha(\omega) = \frac{2\kappa\omega}{c} \tag{38}$$

where c is the light speed [81]. The absorption coefficient $\alpha(\omega)$ determines how far wavelength of light can penetrate a substance before being absorbed.

Observing the absorption spectrum for the bulk α-Fe_2O_3, in Figure 14(a), with reference to the electromagnetic spectrum, the visible light region lies between 400 and 700 nm. For higher conversion efficiency of solar cells, absorption should have the highest peak at visible region, and hence achieving the highest peak at visible region is of great deal for PEC activities. The absorption spectrum indicates that the semiconductor is absorbing more in the ultraviolet (UV) region at wavelengths 50nm to 300 nm; however, at this wavelength (300nm to 400nm), it results in another minor peak, an absorption coefficient approximated at $11x10^2$ cm^{-1}, and there after a decrease with increasing wavelength. The results in the study show a trend similar to a DFT study by Pan *et al.* [43] in enhancing the photoelectrochemical activity by doping 4d transition metals on α-Fe_2O_3. Solar photons falling on Earth have wavelengths of 250-2500 nm, thus absorption is desirable in the visible region for solar to hydrogen conversions, therefore we say α-Fe_2O_3 has a reasonable absorption coefficient, which could be modified by element doping.

The ratio of the light wave reflected from a surface to the amount of light incident on the semiconductor is known as reflectivity, and it may be calculated using the following equation:

$$R(\omega) = \frac{(n-1)^2+k^2}{(n+1)^2+k^2} \qquad (39)$$

Figure 14 (d) displays the reflectivity spectrum $R(\omega)$ against the wavelength. We observe a major peak of reflectivity from wavelengths of 300 nm to 1000 nm, and it occurs where the peak of absorption coefficient starts decreasing with increasing wavelength.

The conductivity of a semiconductor is the property that links the current density to the electric field for general frequencies. The conductivity as a function of wavelength is shown in Figure14 (b), we observe that the bulk α-Fe_2O_3 display a significant conductivity in the UV region between wavelengths 50-300nm. The decrease in the conductivity curve, with wavelength approaching the visible light region (400 -700 nm), is a possible characteristic of low current density of electrons due to low absorption caused by the indirect band gap of α-Fe_2O_3 [48].

The electron conductivity σ, which may be defined as follows (Equation 40), determines the likelihood of electron-hole pairs created within the semiconductor travelling to the surface [43]:

$$\sigma = \frac{ne^2\tau(E_F)}{m^*} \qquad (40)$$

The electron carrier concentration is represented by n in the formula, which is proportional to the following equation:

$$n \propto exp\,(-\frac{E_C - E_F}{K_0 T}) \qquad (41)$$

The electron carrier concentration in the doped system will increase as the distance between the conduction band (E_C) and Fermi level (E_F) decreases. The effective electron mass, denoted by m^* is and defined as:

$$m^*(k) = (\frac{h}{2\pi})^2 [\frac{\partial^2 E(k)}{\partial k^2}]^{-1} \qquad (42)$$

The sum of the conductivities attributable to the movements of electrons in the conduction band and holes in the valence band equals the overall conductivity of an intrinsic semiconductor [19], therefore, the conductivity of a semiconductor is linked to its the electron conductivity, and for a semiconductor with a higher electron conductivity, is in possible position of exhibiting a greater conductivity.

4.2.2.2 DFT+U Method

DFT level of the theory offered important electrical and optical properties of $\alpha-Fe_2O_3$, according to studies. It is generally known, however, that adding a Hubbard U term acting on the Fe-3d orbitals to the usual density functional theory provides for a more precise description of the electronic structure. [82], [43], [46]. To account for the strong on-site Coulomb interaction of Fe-3d states in $\alpha-Fe_2O_3$, the DFT+U technique with U = 5 eV was used for the Fe atom [82].

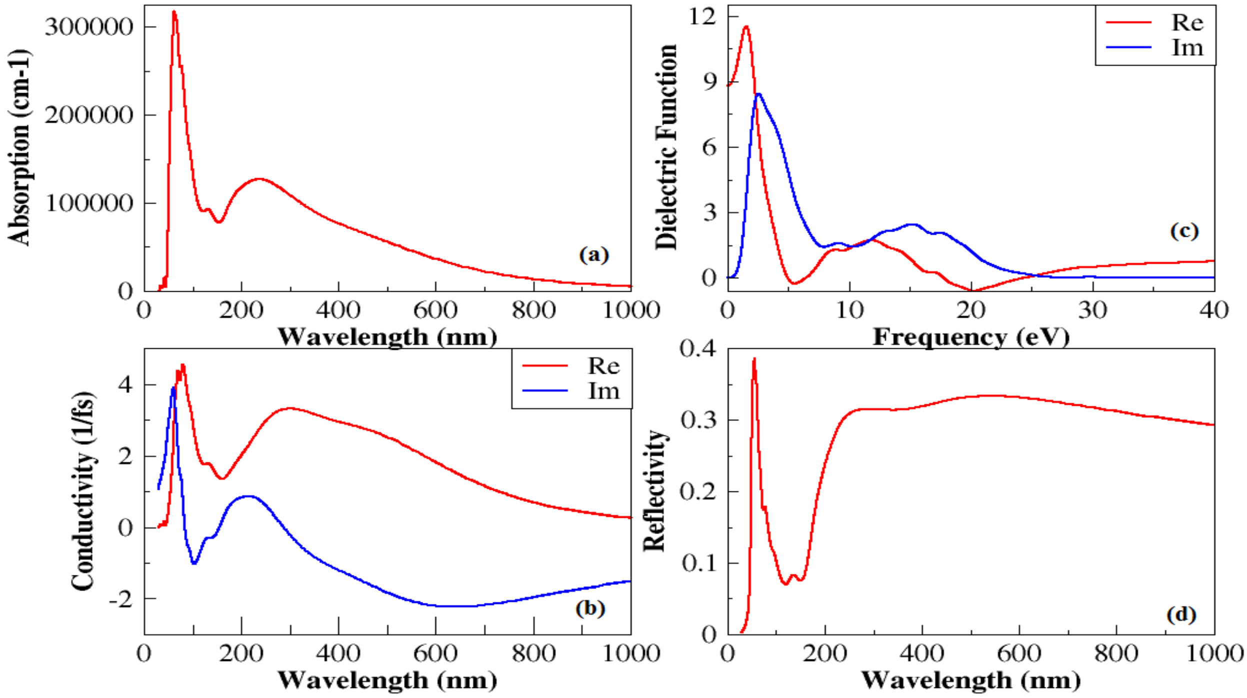

Figure 15: Optical properties: (a) Absorption spectrum, (b) conductivity (c) dielectric function and (d) reflectivity for bulk α-Fe_2O_3 using DFT+U.

To analyze the influence of Hubbard U on the results, we also calculated the optical properties which include the absorption coefficient, conductivity, dielectric function, and reflectivity. For which is the reliable method between DFT and DFT+U in terms of optical properties calculations, we compare the optical properties in Figures 14 and 15. The absorption coefficient graphs of the bulk α−Fe_2O_3 computed with DFT and DFT+U methods are shown in Figures 14(a-d) and 15(a-d), respectively. In terms of absorption, they are both observed to absorb more in the the UV region than in visible light region, the highest peak shows that the coefficient is approximately 3.1x10^4 cm^{-1} by DFT+U, which is lower than that of DFT (~3.9x10^4 cm^{-1}) (see Figure 14 (a)). Furthermore, from wavelengths 400-700nm (visible light region), the graph for DFT+U shows a major drop compared to the DFT graph in Figure 14(a). The results imply that the absorption coefficient values are different with DFT and DFT+U, however, they display a similar trend, it is the same with the other optical properties; for example, looking at Figure 15(c), the real part of the dielectric function is giving a negative value at frequency 20 eV, and the opposite in Figure 14(c). Through observation, DFT+U gives a more accurate prediction of the electronic properties than the optical properties. DFT+U demonstrates that an onsite Coulomb interaction of U = 5 eV leads to an appropriate description of electronic characteristics, according to a previous work. [44] [82]. In summary, the DFT method is recommendable for optical properties calculations and DFT+U for electronic properties calculations on bulk structure. However, because Fe is the dopant substitution site in this study, the number of Fe-3d states will be lower than the number of Fe atoms in the bulk structure. As a result, the strong on-site Coulomb interaction of Fe-3d states in the Fe2O3 surface may not have much effect. Hereinafter, the use of DFT in surface structure calculations would also be recommended, as the study aim at enhancing photocatalytic activities by improving the limitations faced with α−Fe_2O_3 which are their optical properties.

4.3 α-Fe_2O_3 (001) and (101) Surfaces

For this work, we investigated the electronic and optical characteristics of α-Fe_2O_3 (001) and (101) surfaces doped with Cu, Ti, Ni, and Mne using DFT computations. Cu, Ti, Mn, and Ni are first-row transition metals with similar ionic radii to iron but distinct quantities of 3d electrons, resulting in different redox characteristics.

The hematite slabs (001) and (101) used in this work are composed of two closed-packed layers thick cleaved from the bulk structure (Figure 11). α-Fe_2O_3 (001) surface has nine O atoms and eight Fe atoms per surface unit cell. The chosen slab was thick enough to allow room for a doping site, set to a slab thickness of 8.003 Å. Figure 16 shows a doped-α-Fe_2O_3 (001) surface model doped with different transition metals.

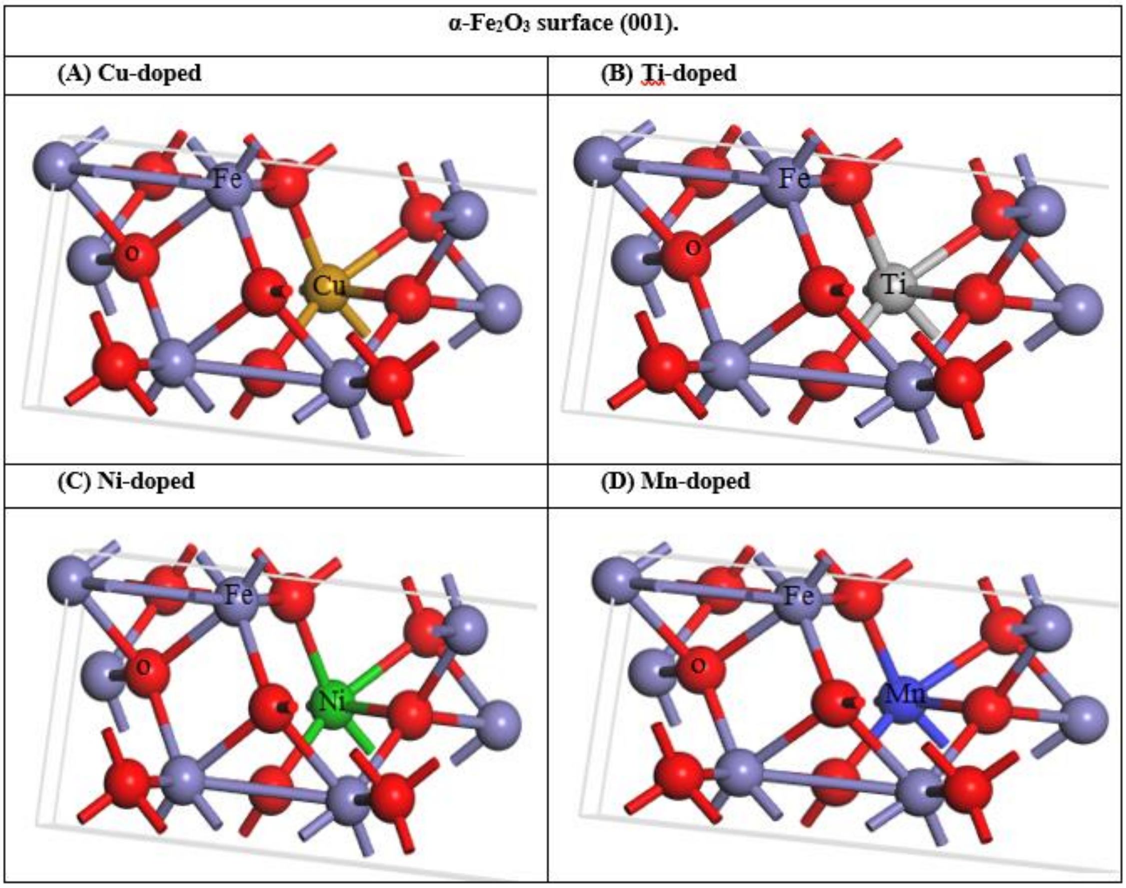

Figure 16: α-Fe$_2$O$_3$ (001) surface doped with (A) Cu, (B) Ti, (C) Ni and (D) Mn

Figure17 depicts α-Fe$_2$O$_3$ surface structure in the direction (101), doped with various transition metals. The surface thickness was set to 8.624 Å, to at least have iron atoms remaining, after the substitution of the dopants. The vacuum thickness chosen to be 9,17 Å, to restrict the atoms from being close to one another, and allowed more doping regions exposed. The surface consists of eight iron (Fe) atoms and 12 oxygen (O) atoms. The doping model for the (001) and (101) α-Fe$_2$O$_3$ surfaces was created by substituting one atom of iron (Fe) with a single dopant (Cu, Ti Ni, or Mn) atom per surface.

α-Fe_2O_3 surface (101).	
(A) Cu-doped	**(B) Ti-doped**
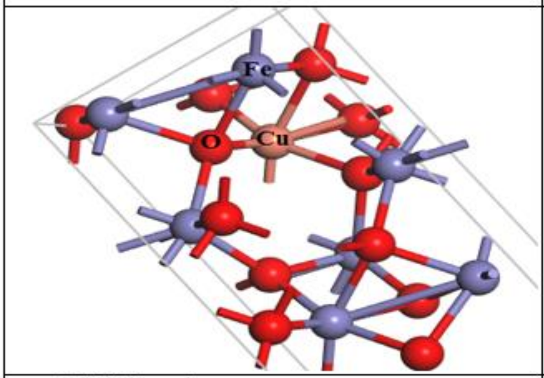	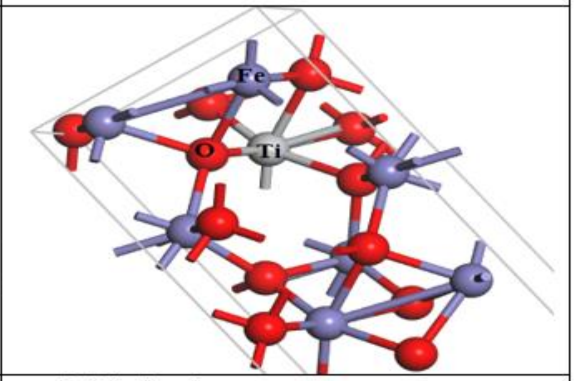
(C) Ni-doped	**(D) Mn-doped**
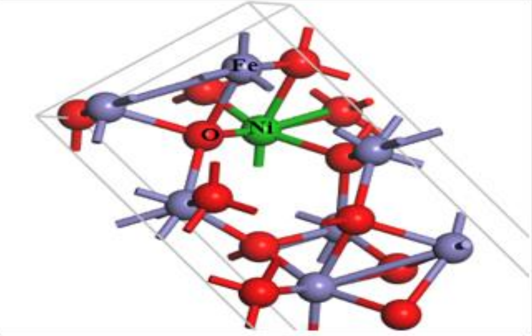	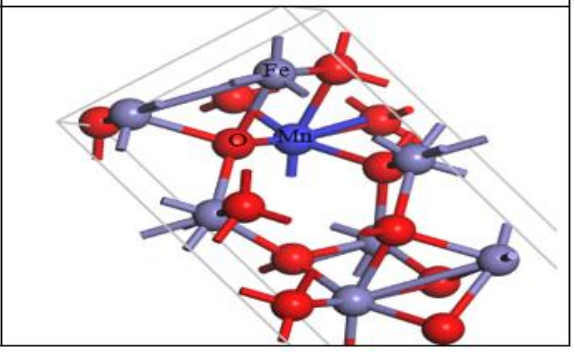

Figure 17: α-Fe_2O_3 (101) surface doped with (A) Cu, (B) Ti, (C) Ni and (D) Mn.

Table 2: Relaxation energies of the dopants, undoped α-Fe_2O_3 (001) and (101) and surfaces and doped α-Fe_2O_3 (001) and (101) surfaces

System	**Energy$_{(surface)}$ (eV)**	**Energy$_{(atom)}$ (eV)**	**Energy$_{(surf+atom)}$ (eV) of α-Fe_2O_3**
Pure α-Fe_2O_3 (001) Pure α-Fe_2O_3 (101)	-9117.648 -6076.842		
Cu Ti Ni Mn		-608.512 -738.571 -3088.792 -7001.041	
Cu-α-Fe_2O_3 (001) Ti-α-Fe_2O_3 (001) Ni-α-Fe_2O_3 (001) Mn-α-Fe_2O_3 (001)			-9727.327 -9860.160 -12210.637 -16122.152
Cu-α-Fe_2O_3 (101) Ti-α-Fe_2O_3 (101) Ni-α-Fe_2O_3 (101) Mn-α-Fe_2O_3 (101)			-6687.760 -6819.618 -9168.316 -13081.925

4.3.1 Electronic properties for α-Fe_2O_3 surface (001)

Figure 18 illustrates the estimated band structure and density of states (DOS) for an undoped α-Fe_2O_3 (001) surface. The electronic band structure, like the bulk structure, has a 1.61 eV band gap, the VBM is dominated by the O-2p and minor Fe-3d states at the lower energy level while the Fe-3d states are dominant in CBM at different energy levels, which is consistent with previous first-principles calculations [43]. The DOS plot confirms that the surface is an n-type semiconductor because the band gap is found at the lower energy level. Elemental doping as confirmed by the literature will likely modify the energy gap of the surface.

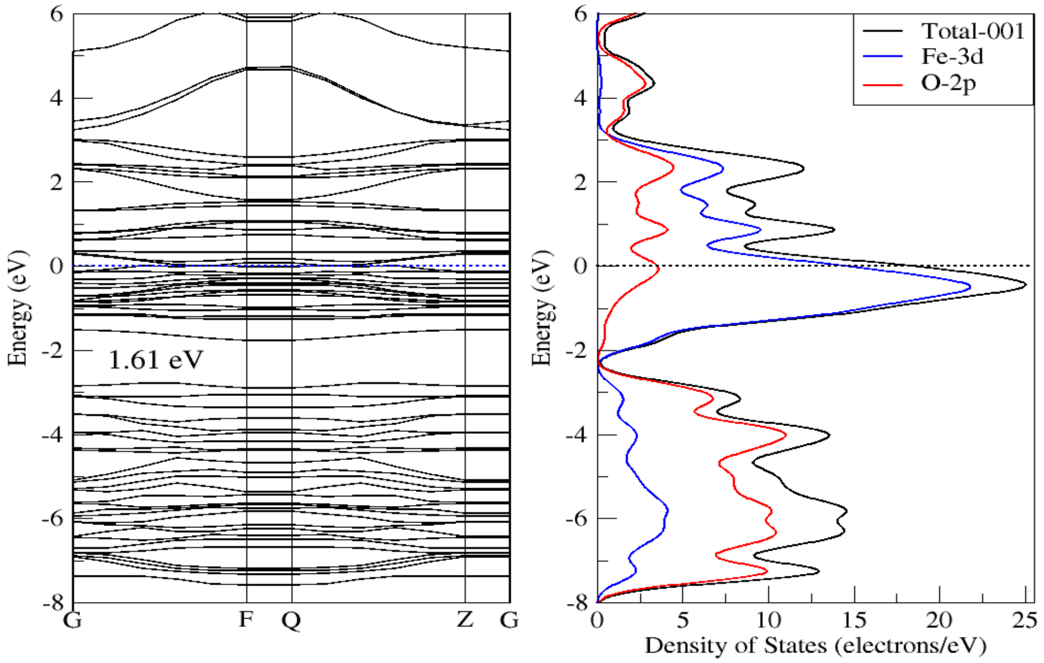

Figure 18: Undoped α-Fe_2O_3 (001) surface band structure and DOS plot.

Figure 19 plots the band structure and density of states (DOS) to show how copper affects the electronic characteristics of the surface (001). At various energy levels, the plot depicts a succession of DOS peaks caused by O-2p, Cu-3d, and Fe-3d.

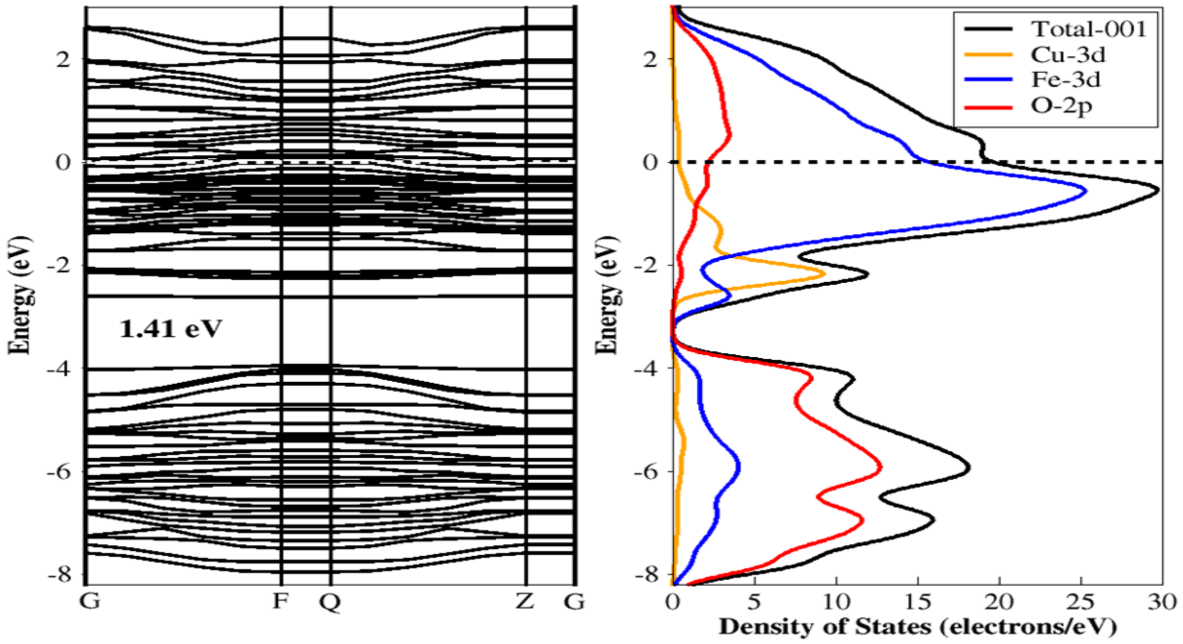

Figure 19: Cu-doped- α-Fe_2O_3 (001) surface band structure and DOS plot.

When Cu is used to substitute for an iron atom, the Fermi level for Cu-doped hematite enters the conduction bands after Cu-3d orbitals are instigated in the conduction band minimum (CBM) of hematite and move the band gap to a lower energy level. In the valence band, the O-2p states also extends to a lower energy and has a high hybridization with the Cu-3d and Fe-3d states. The O-2p states are dominant within the valence band, which, according to Nelson *et al.* [42], suggest that α-Fe_2O_3 is an O-2p - Fe-3d charge transfer. In addition, at energy around -0.6 eV near the Fermi level, the hybridization in the CB is mainly with contributed Fe-3d states and minority of O-2p and evidence of Cu-3d density of state at very low energy. The structure has resulted in a band gap of 1.41 eV, which is narrower than that of the undoped surface in Figure 18. The band gap has narrowed from 1.61 eV to 1.41 eV. The results of previous experimental studies state that a reduced band gap may lead to a low rate of charge recombination and a more absorbing surface [27] [26]. Cu–O bonding suggests the formation of an intermediate or solid solution state that can modify the inherent absorption peak of α-Fe_2O_3. Dopingα-Fe_2O_3 (001) surface with Cu influences the narrowing of the band gap due to the down shift of the CBM edge.

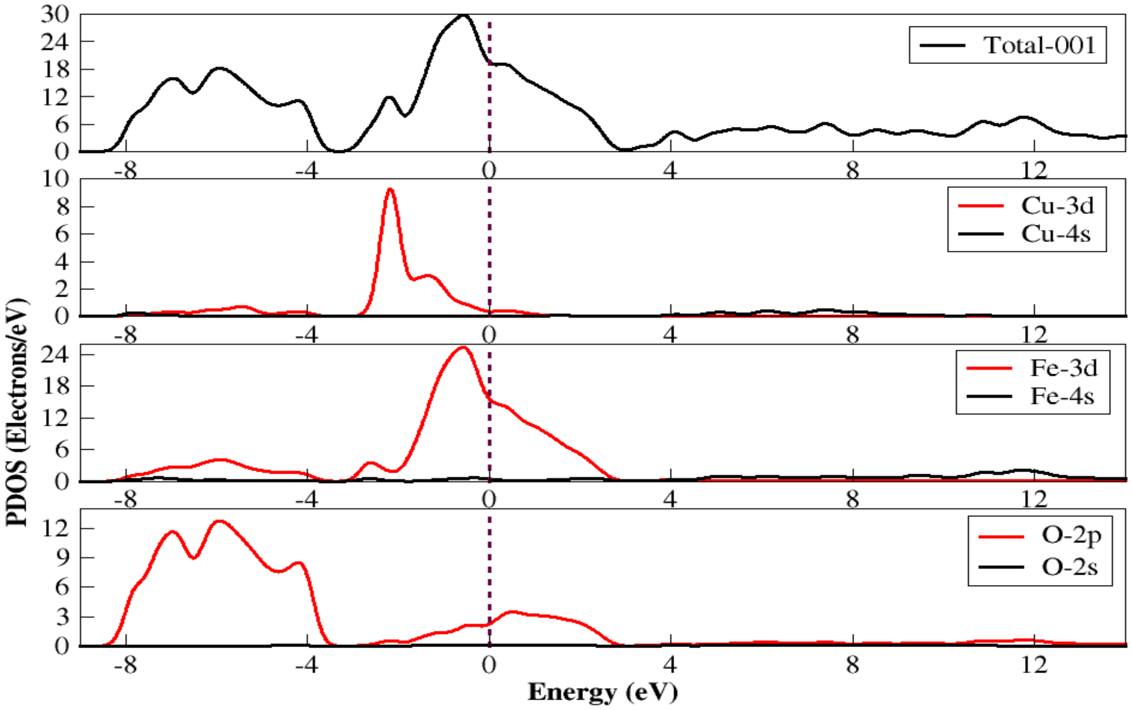

Figure 20: PDOS for Cu-doped- α-Fe_2O_3 (001) surface.

The trend for Cu doped α-Fe_2O_3 can be further characterized from the partial density of states (PDOS) plot shown in Figure 20. We considered the last two states in the atomic configuration for each atom involved for Cu-doped α-Fe_2O_3 surface, where Cu is $3d^{10}4s^1$, O is $2s^22p^4$ and $3d^24s^2$ for Fe. Evidence from the graph indicates that in the conduction band at the very lowest density of states in the energy range from 5 to 8 eV there is an appearance of Cu-4s and Fe-4s and a slight sign of O-2s also in the conduction band on energy range from 0.5 to 3 eV. Hybridization between Fe-3d, O-2p and Cu-3d resulted in sates in the valence band near the fermi level. The presence of Cu-3d states in the valence is the reason we have a reduced band gap. Meng *et al.* showed that doping α-Fe_2O_3 with Cu can reduce the band gap from 2.06 eV to 1.37 eV [46], so these results are consistent with our findings. A band gap of 1.41 eV, which is much lower than that of a pure surface, will also increase the photon energy absorption.

Doping with Ti donates electrons in the conduction band as observed from the band structure plot in Figure 21. The CBM is modified by the Ti-3d orbitals and spreads out more compared to the undoped α-Fe_2O_3 surface. The CBM of Ti-doped hematite (001) shift toward the valence band and decrease, resulting 1.55 eV as the new value of the energy gap.

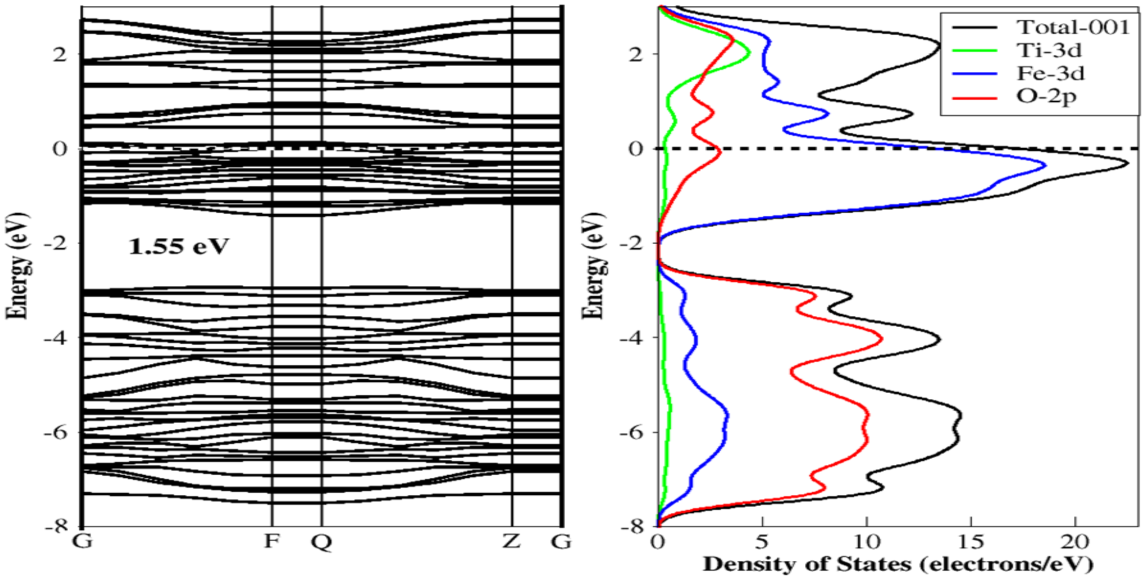

Figure 21: Band structure and DOS for Ti-doped- α-Fe_2O_3 (001) surface.

Due to this significant shift, the peak position of Ti-3d DOS moves towards high energy level. A conduction band full of delocalized states will also perform an increase electrical conductivity. When Pan *et al*. [83] added the impurities of Ti in pure α-Fe_2O_3, they observed feature that are similar and speculated that the CBM's delocalization indicated enhanced carrier transport in the system due to a reduced electron mass, as inferred by the wavy structure of the CBM. As a result, the excited electrons would be able to migrate to the surface and be involved in the reduction-oxidation reaction, which is consistent with the experiment's increased conductivity. [84][83]. This means Ti-doping could have added conduction electrons, which will comprehend a faster rate of electron transportation. The PDOS for Ti-doped α-Fe_2O_3 (001) surface in Figure 22 shows that the Ti-3d states dominate the conduction band, therefore the band gap has changed to the lowest energy level. The hybridization from mostly Ti-3d states, with minimal Fe-3d and O-2p states, makes up the conduction band.

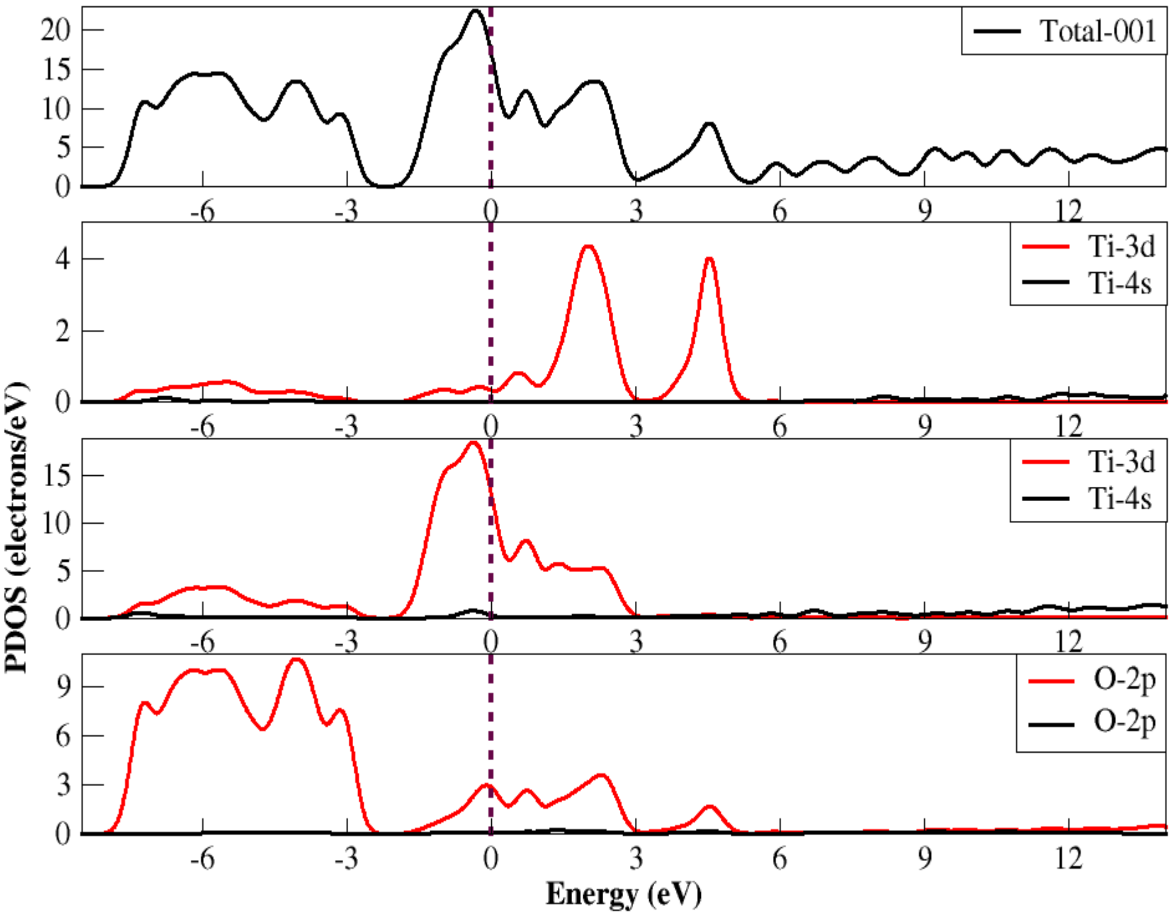

Figure 22: PDOS for Ti-doped- α-Fe_2O_3 (001) surface.

There is also evidence of Ti-4s in the energy range of 7 to 10 eV, though at a very low density of states, we could then say that the CBM is modified by the 3d and 4s orbitals of Ti and Because of the dispersive properties exhibited by Ti in the band, electrons should have a reduced effective mass, Snir *et al.* [78], also stated that doping α-Fe_2O_3 with Ti generates excess electrons. The Ti dopant within α-Fe_2O_3 substitutes Fe^{+3} with Ti^{+4}, thus there is an excess electron for every Ti element to compensate for the charge, hence improved electrical conductivity.

For nickel doped α-Fe_2O_3 (001) surface, the optical band gap has been found to be 1.31 eV, which shows an obvious band gap narrowing. Figure 23 shows the band structure and DOS plot of the Ni-doped hematite surface (001) to investigate its electronic properties. The DOS indicates that the introduction of Ni-3d states has resulted in a concentration of electrons; this is indicated by the hybridization of the Fe-3d, Ni-3d, and O-2p sates showing a higher density of states in the conduction band compared to the valence band. Moreover, the valence band maximum has shifted to a higher energy level.

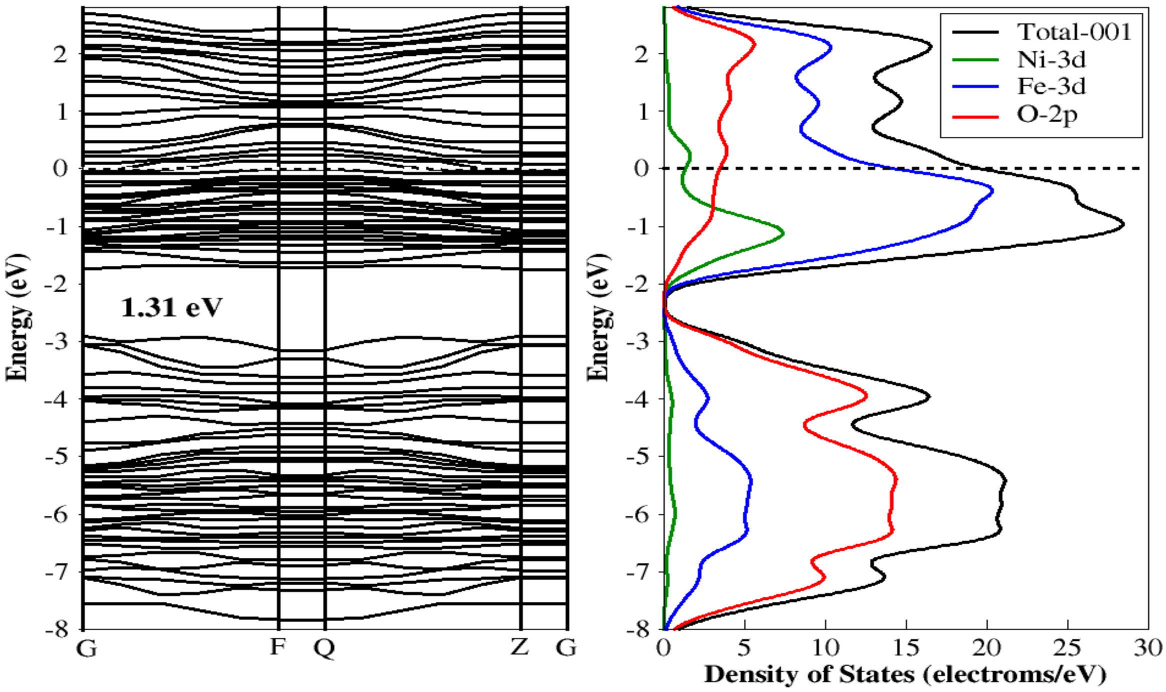

Figure 23: Ni-doped- α-Fe_2O_3 (001) surface band structure and DOS plot.

Doping with Ti and Cu has thus far shown that the valence and conduction band edges are modified; on the other hand, the mechanism of Ni-doped hematite is reported by

Huda *et al.* [44], the findings imply that doping Ni lowers volume in a consistent manner. Because the mobility of tiny polarons limits the transport characteristics of α-Fe_2O_3, changes in volume may modify the electrical conductivity by changing the hopping probability. The substantial localization of Ni-d orbitals was shown to be connected to volume decrease for Ni substitution, which is consistent with the fact that the d orbitals get increasingly localized from Sc to Ni, recent experiments and theory also showed similar behavior [44], [85].

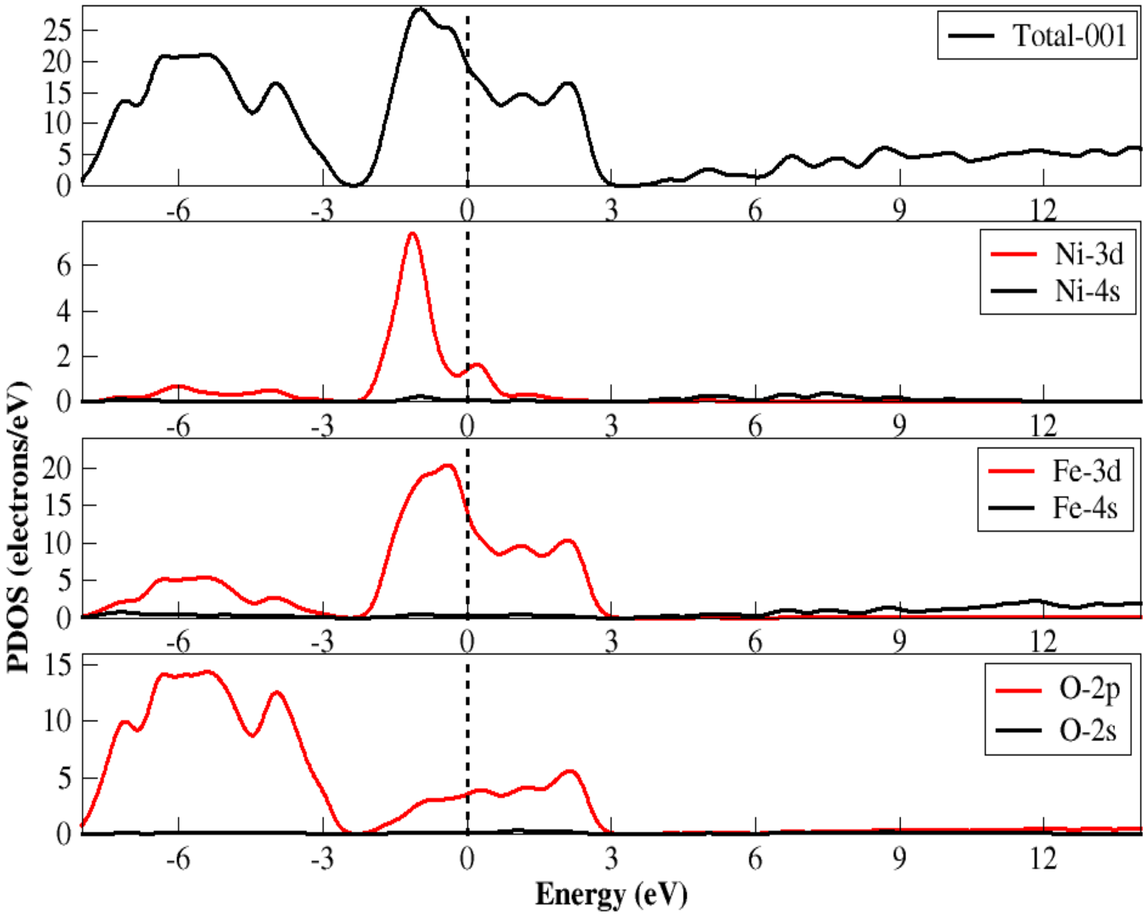

Figure 24: PDOS plot for Ni-doped- α-Fe_2O_3 surface (001).

According to the partial density of states (PDOS) analysis in Figure 24, the Ni-3d orbitals are mainly dominant in the valence band with the highest peak from energy –2 eV to -0.2 eV. As evident from Figures 23 and 24, doping Ni has shifted the band gap to a higher energy level when compared to a pure surface; in other words, this also influences the surface structure. Suman *et al.* [86] also stated that Because Ni^{2+} ions produce a charge imbalance in the host lattice, doping α-Fe_2O_3 with Ni has an effect on the physical and chemical properties. As a result, a change from Fe^{3+} to Fe^{2+} happens to maintain charge neutrality, resulting in structural disorder or flaws. The electronic characteristics of Ni-doped α-Fe_2O_3 nanostructures will be influenced by these lattice defects, as well as the structural and optical features.

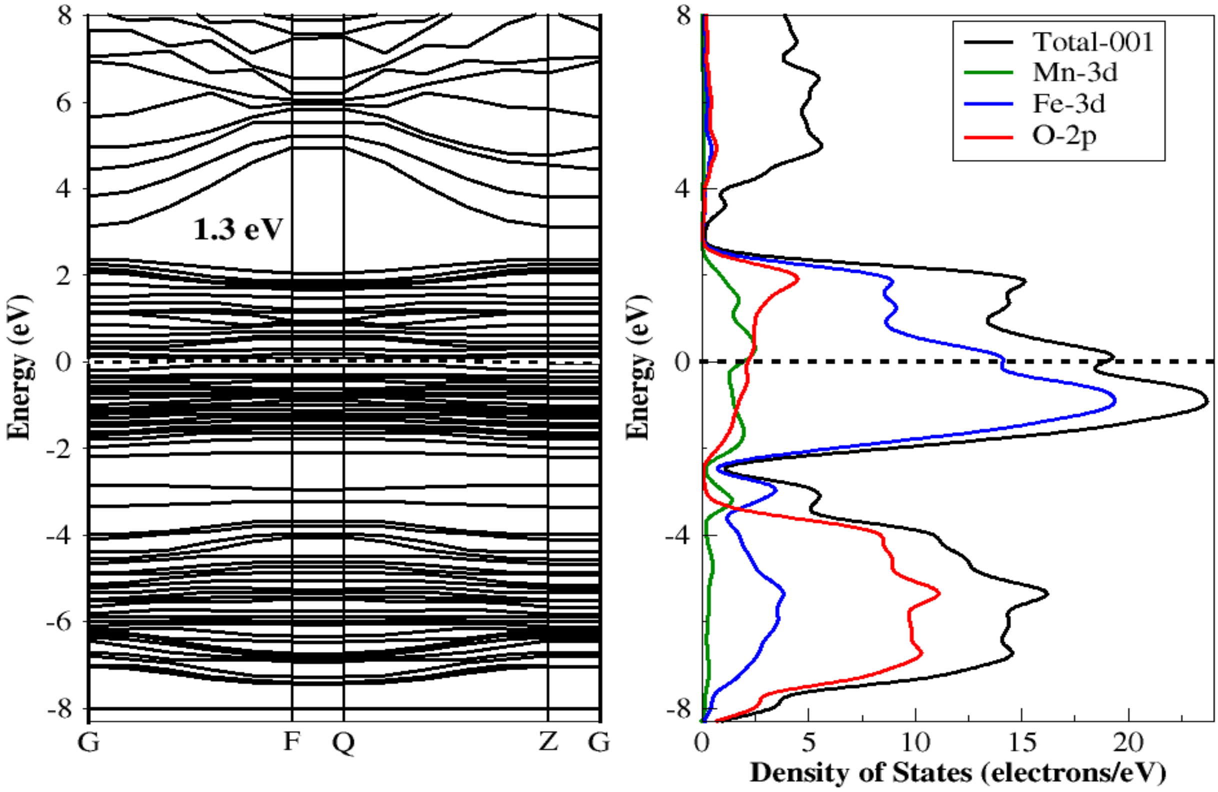

Figure 25: Mn-doped- α-Fe_2O_3 (001) surface band structure and DOS plot.

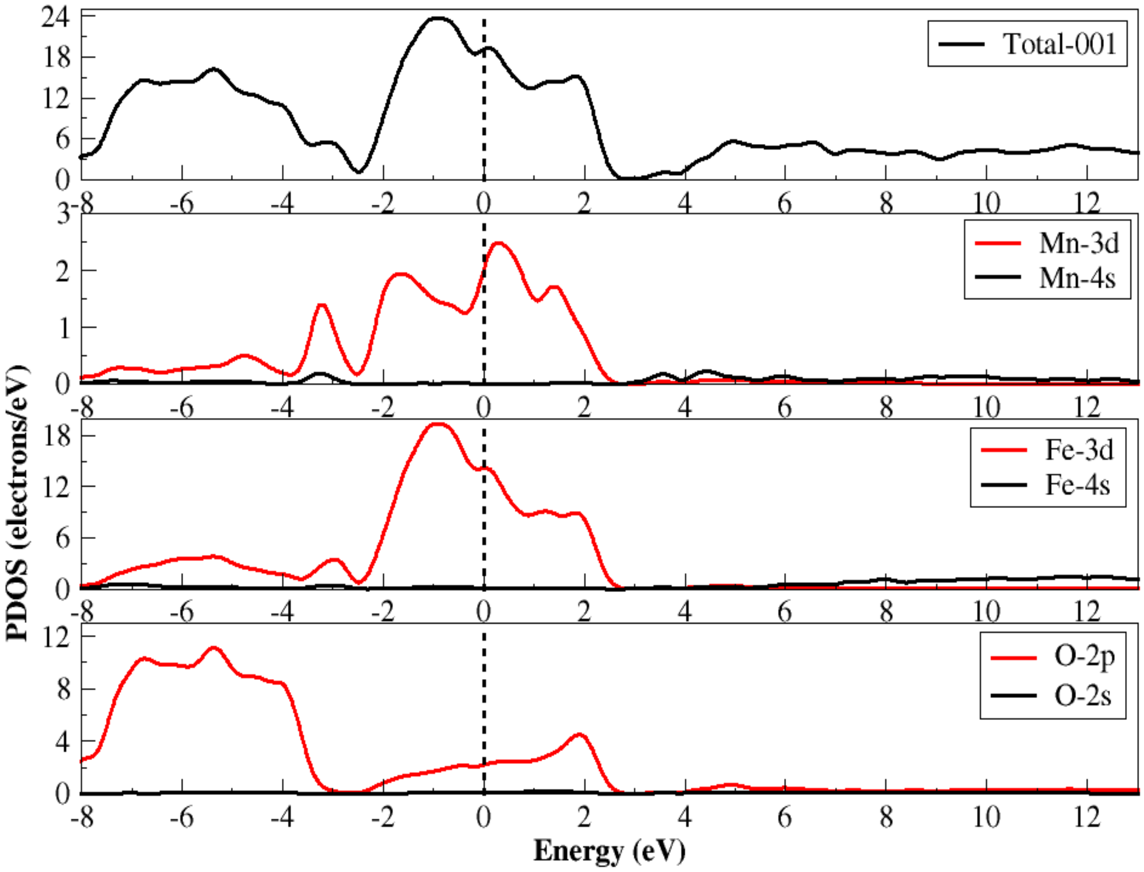

Figure 26:PDOS for Mn-doped- α-Fe_2O_3 (001) surface.

To explain the effect of Mn doped on α-Fe_2O_3 (001) surface, the band structure and density of states are shown in Figure 26. First, we compare the changes of the DOS of the surface before and after doping, and we observe that the DOS of system after doping with Mn are slightly changed. The Fe-3d orbital peaks in the fermi level as before, however, since the energy band gap shifted to a much higher energy level, we no longer observe the multiple major peaks in both bands, similarly with the O-2p, it is only observed in the valence band and near the Fermi level (Figures 25 and 26). As seen in Figure 25, the band gap has reduced from 1.66 to 1.3 eV. It is most obvious that introducing Mn-3d orbital has impacted the band structure of the surface. In addition, the Mn-3d orbitals at 2.5 eV disappear as observed in Figure 26. Based on the above analysis, Mn doping can significantly lead to a surface with a great electrical conductivity; this, according to Lyu *et al.* [73], a narrower band gap, will promote the separation of hole and electron in the band gap.

Due to the symmetry break in the crystal potential field, doping (001) surface with Cu, Ti, Ni, and Mn has enlarged the energy range of the conduction band and generates a split in Fe-3d and O-2p orbitals energy. Table 3 lists the details of the change in band gap of the doped α-Fe_2O_3 (001) surface. The adsorption energy conveys the binding ability of the atom. The adsorption energies of the Cu, Ti, Ni, and Mn doped α-Fe_2O_3 (001) surface are given by equation 35 and the results are listed in Table 3.

Table 3: The energy band gap, and adsorption energies for doped and pure α-Fe_2O_3 (001) surface.

Dopant	Band gap $(E_g)\ eV$	Adsorption energy ((E_{ad}) eV
Cu	1.41	1.167
Ti	1.55	3.941
Ni	1.31	4.197
Mn	1.30	3.463
Pure	1.61	0

The adsorption energies of the four adsorption models are all positive, indicating that each doped system is spontaneously adsorbed. The absolute value of the the adsorption energy of Ni-doped α-Fe_2O_3 system is greater than that of the other doped surfaces, which means that the adsorption of Ni will release more energy. The conclusion is that the Ni molecule is more likely to adsorb on the α-Fe_2O_3 (001) surface.

4.3.2 Optical properties for α-Fe_2O_3 (001) surface

Because α-Fe_2O_3 is a potential photocatalyst, it's crucial to figure out how photons interact with the compensated Cu, Ti, Ni, and Mn in the -Fe2O3 (001) surface. Furthermore, the absorption property study is a precise complement to the electrical structure. Enhancement of these optical properties by element doping will ensure a successful photocatalytic performance of α-Fe_2O_3 under visible light region. Narrow-bandgap semiconductors have a higher optical absorption capability than wide-bandgap semiconductors, making them more prone to efficiently harvesting low-energy photons.

The ability to predict optical characteristics aids in our understanding of how optical photons interact with electrons in doped and undoped α-Fe_2O_3. Figure 27 shows the dielectric function of hematite (001) surface doped with various metals. The optical dielectric interbond transitions from the occupied band to the partially filled band. The energies of the dielectric interbond transitions thus reveal insight into the electronic band structure, as defined by Equation 36. The variation of $\varepsilon_1(\omega)$ and $\varepsilon_2(\omega)$ against frequency is observed for all doped (001) surfaces. It can be seen from Figure 27 that the dielectric constant for both the imaginary and real parts gradually decrease with increasing frequency. In the range of 10 to 40 eV, we observe a constant dielectric function, and it is maintained throughout, this trend shows that at higher frequencies all the systems remain constant. Based on Maxwell-Wagner and Koop's theories [86], the drop in the dielectric constant can be attributed to grain-boundaries at low frequencies, whereas the grain becomes successful at inflated frequencies, and the graph exhibits practically straight-line behavior in this range.

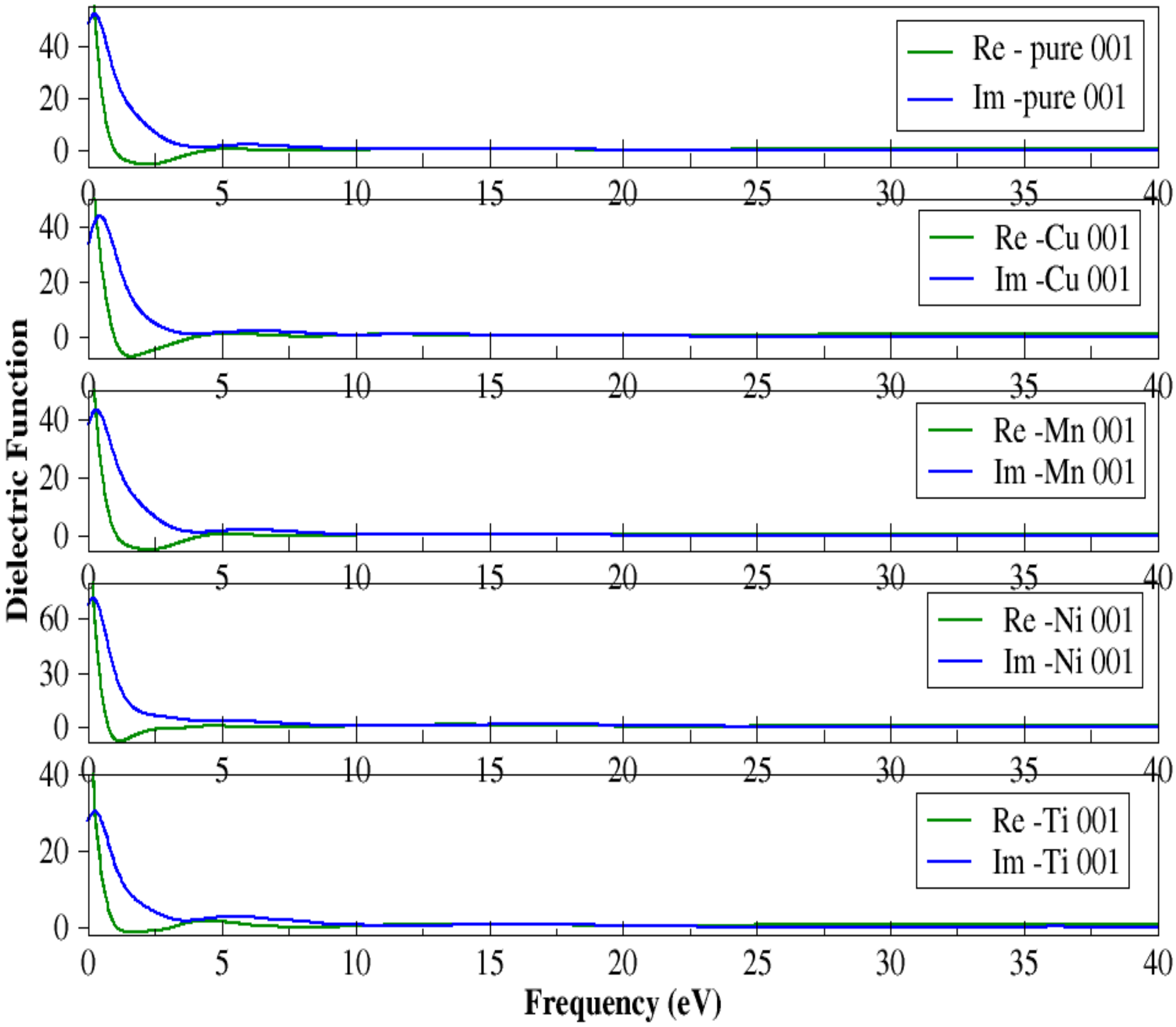

Figure 27: Dielectric function for undoped and doped α-Fe_2O_3 (001) surface.

Absorption coefficient $\alpha(\omega)$ defined in Equation (38) gives information about the solar energy conversion of material and how far light of specific wavelength can penetrate the material before is being absorbed. Transition metal dopants, which may create additional states, have been explored to modify the electronic structure of α-Fe_2O_3 to subsequently improve light absorption under visible light. Figure 28 shows the absorption spectra of undoped and metals doped α-Fe_2O_3 (001) surface. Here, we observe that the four doped surfaces can strongly respond to the UV light region and have weak absorption activity in the visible light region. However, with that observed, when comparing the undoped and doped surfaces in the visible region (400- 700 nm) shown in Figure 26, it is evident that Mn-doped-α-Fe_2O_3 (001) surface shows a broad absorption coefficient with a peak of ~10x10^4 cm^{-1} at wavelength ~500 nm.

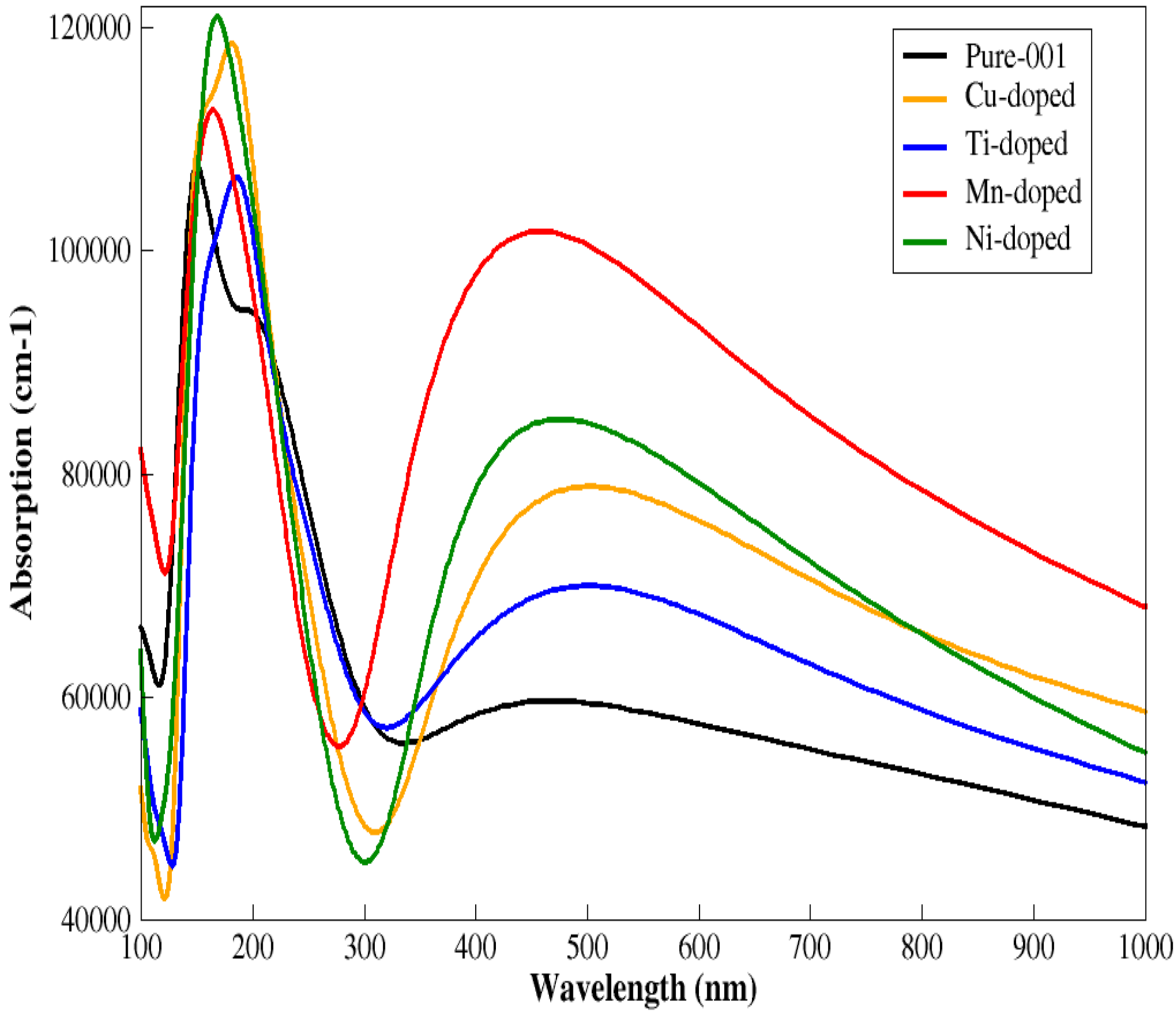

Figure 28: Optical absorption spectra of undoped α-Fe_2O_3 (001) surface compared with Cu, Ti, Ni and Mn-doped surfaces.

At wavelengths 400 to 700 nm, the undoped surface again shows the lowest absorption in the visible light compared to the doped surfaces. Research has suggested that photons with wavelengths around 550 nm are absorbed via indirect transitions (Fe-3d Fe-3d), which are not particularly absorptive in visible light [83]. The optical absorption coefficient of the doped surface does not considerably improve to a higher value in the visible range when these dopants are used (400-700 nm); however, the doped surface in Figure 28 exhibits a better absorptive coefficient at wavelength 400 nm than the undoped surface with manganese being the most efficient, followed by nickel, copper and then titanium at 450 nm. The Cu-doped absorption spectra is at a peak with an absorption coefficient ~7.2×10^4 cm^{-1}. Also, we observe that Ni absorb better in visible region with an absorption coefficient of ~8×10^4 cm ^{1}. In terms of electronic qualities, past research has shown that a reduced band gap provides a major benefit for effective optical absorption and, as a result, greater solar cell efficiency [87], and our results show a similar trend. Moreover, we can observe this from Figures 19-25, the reduction of the energy band gap suggests a faster velocity of photo-generated hole, and due to this, more photons in the solar spectrum can be absorbed, which is confirmed by the literature [83].

The absorption spectra of the pure hematite and Ni doped α-Fe_2O_3 surface are representative transition-metal oxide with strong electron correlation, resulting in complex electronic structures and rich optical properties. Ying Lui *et al.* stated that experimentally the photoelectrochemical response of Ni-doped hematite shows effectiveness for the photo-splitting of water and the doping level affects the photocatalytic activity of thin films [88]. Here in Figure 28, Ni – doped α-Fe_2O_3 surface (001), shows a broad absorption in the region (50-300) nm known as the UV region. The peaks at 50 nm and 200 nm may be associated with 3d orbitals near the Fermi level as seen in figure 26 for the other dopants. Upon doping Ni, the band gap is slightly reduced; this occurrence suggests that there is an opportunity for increased photon absorption, and this was previously confirmed both theoretically and experimentally [73].

Transition metals, according to Yin *et al.* [89] are cation substitutes for Fe atoms that have a smaller or higher ionic radius than the host Fe atoms. The ionic radius variation would give in variances in coupling between neighboring atoms, which would likely increase the light sensitivity. Mn and Ni doping shows the narrowest band gap compared to Ti and Cu, hence, in the visible light spectrum, they have a high absorption.

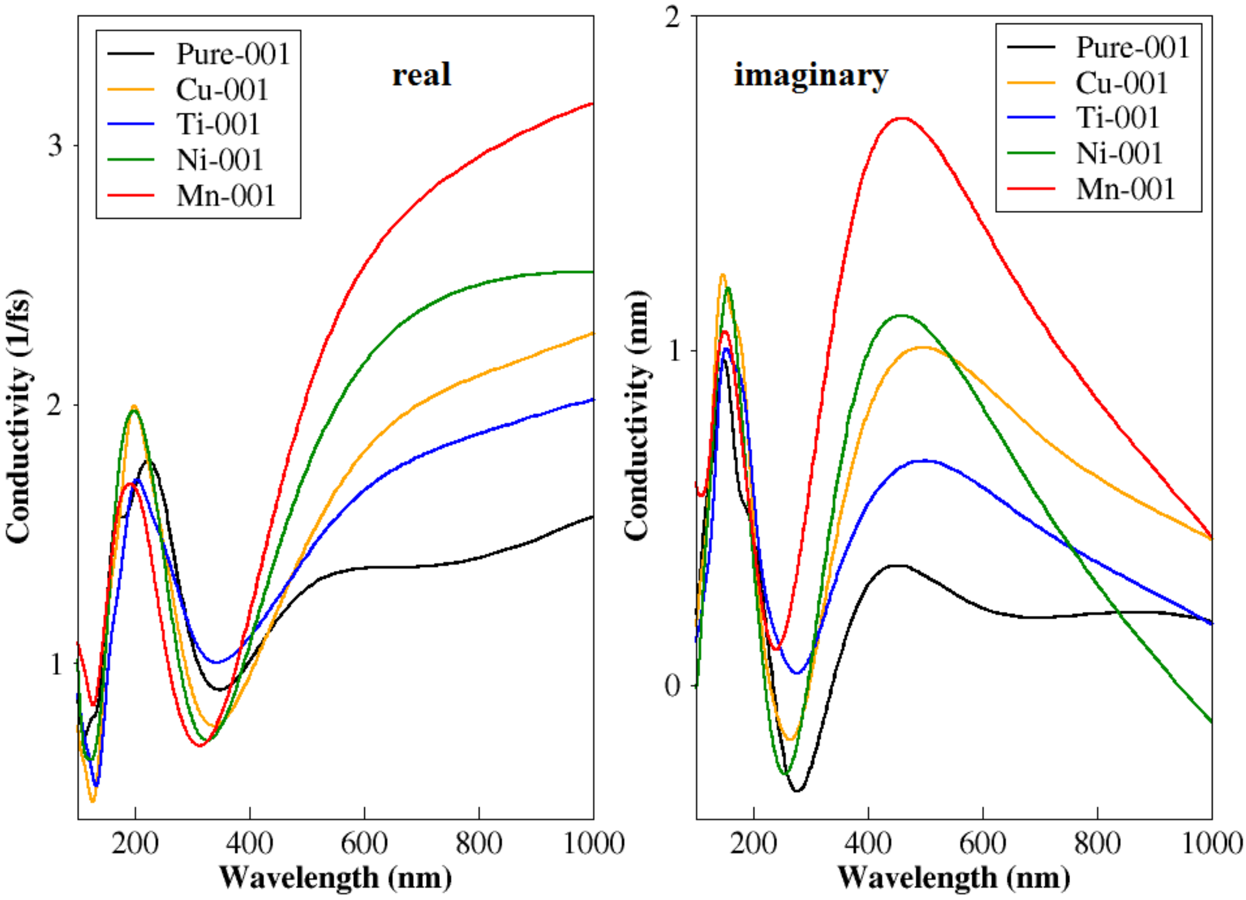

Figure 29: Conductivity of Ti -, Cu-, Ni- and Mn-doped α-Fe_2O_3 compared with undoped α-Fe_2O_3 (001) surface.

Pure hematite has been reported to have poor conductivity [43], therefore, after doping, we calculated and analyzed whether there has been any improvement in terms of conductivity. However, due to the re-orientation of atoms and surface thickness during cleaving, the conductivity of a bulk could be more than that of a surface; hence our interest is comparing the conductivity of the undoped with the doped surfaces. Figure 29 displays the conductivity plots for doped copper-, titanium-, nickel-, and manganese-doped hematite (001) surfaces compared with undoped hematite surface. The graphs depict the two parts of the spectra, one part representing the real part of conductivity and the other representing imaginary part of conductivity. In the visible region (400 – 700 nm), manganese doped surface shows to have the highest peak on both the real and imaginary parts of the conducting spectrum, followed by Ni, Cu and then Ti. At this region we observe an improved conducting surface when modified by elemental doping. We also observe some response in the UV region at wavelength 200 nm from Cu- and Ni-doped surfaces.

At wavelengths 400 nm to 1000 nm, titanium displays a great increase in conductivity. The visible light regions on the real part of the spectra shows that after doping with Ti there is an improved conductivity compared to the undoped surface. This kind of transformation of optical conductivity correlates to the findings on the partial density of states in Figure 21, showing that the Ti-3d states are a major contributor in the conduction band which initially was occupied by minor Fe-3d states. According to the theory, electrons in all states belonging to unoccupied zones can contribute to the electric current; thus, d and s electrons must be categorized as conductivity electrons [90]. Because the vacant d states are important for ferromagnetism and there is a direct relationship between magnetic characteristics and electrical conductivity, conduction electrons may make Ti-3d to the unoccupied d states. As a result, we believe that the 3d orbitals created by titanium doping are likely to boost PEC activity by increasing electrical conductivity in the visible light area.

Although the Cu-doped surface follows the trend of the 3d states, in Figure 19, the Fe-3d states occupy the conduction band more compared to the Cu-3d states, and this could be the possible reason why some parts along the wavelength of the undoped (001) surface are greater than the doped (001) surface. Huda *et al*. used the LSDA+U method to investigate the electrical structure of the 3d transition metal inserted α-Fe_2O_3. According to the results of this research, using Ti would result in the largest gain in electrical conductivity [44].

Nickel is a group VIII element and literature shows that Ni is not widely studied as a dopant for α-Fe_2O_3. However, experiments indicated that substituting Fe^{3+} with Ni^{2+} increased the carrier density of hematite nanoparticles and hence improved the conductivity [91]. The introduction of Ni as a dopant has a greater influence on the carriers with low energy, resulting in a sharp conducting surface in the visible light region. According to DFT calculations and previous theoretical work, Ni atoms provide another transfer path for photocarriers, which is more conductive than in the pristine band, as its transitions are permitted [92].

Manganese oxides have been widely employed as electrocatalysts for water oxidation and fuel cell applications [16], but manganese as a suitable dopant, particularly as a dopant in hematite, has not been thoroughly investigated. Mn is an attractive dopant in -Fe2O3 due to its atomic radius and the multivalent nature of Mn ions. Because Mn is close to Fe on the periodic table, its atomic radius is quite similar to the radius of Fe, and so the crystal structure of α-Fe_2O_3 will not be much distorted. Mn is also a potential p- or n-type dopant for α-Fe_2O_3 because it can exist as Mn^{2+} and Mn^{4+} ions. Mn doping was also expected to produce energy levels within the α-Fe_2O_3 band gap, which could be useful for modifying electrical conductivity. [16]. From the analysis of the electronic band structure of Mn doped α-Fe_2O_3 in Figure 25, the valence band is dominated by the Mn-3d states and this could mean that during charge transport we may have a very low rate of charge recombination since Mn can exist as Mn^{2+} and Mn^{4+} ions. This suggests why we observe a greater conductivity of Mn-doped α-Fe_2O_3 in the visible light region (400- 700 nm). Experiments indicated that as the Mn-content increases in the hematite solid solution, the number of pairs of (Fe^{2+}, Fe^{3+}) and (Mn^{2+}, Mn^{3+}) in the solid solution increases, which changes the conductivity of the solid solution [93].

From wavelengths 600 -1000 nm on the imaginary parts of the spectra in Figure 29, we observe a decrease in the conductivity, hence an increase in the real part of the spectra within the same region of the wavelength and following this trend we therefore suggest that the imaginary part of the graph shows the part where the surface is not conducting.

4.4 α-Fe_2O_3 (101) surface

4.4.1 Electronic properties for α-Fe_2O_3 (101) surface.

In Figure 30, the calculated band structure shows that the pure α-Fe_2O_3 (101) surface has a band gap of 1.72 eV. The density of states shows that the VBM is filled with Fe-3d and O-2p orbitals, while the CBM is mainly empty Fe-3d states, and contributing O-2p states same as in the bulk hematite system; hence this is consistent with previous predictions [43].

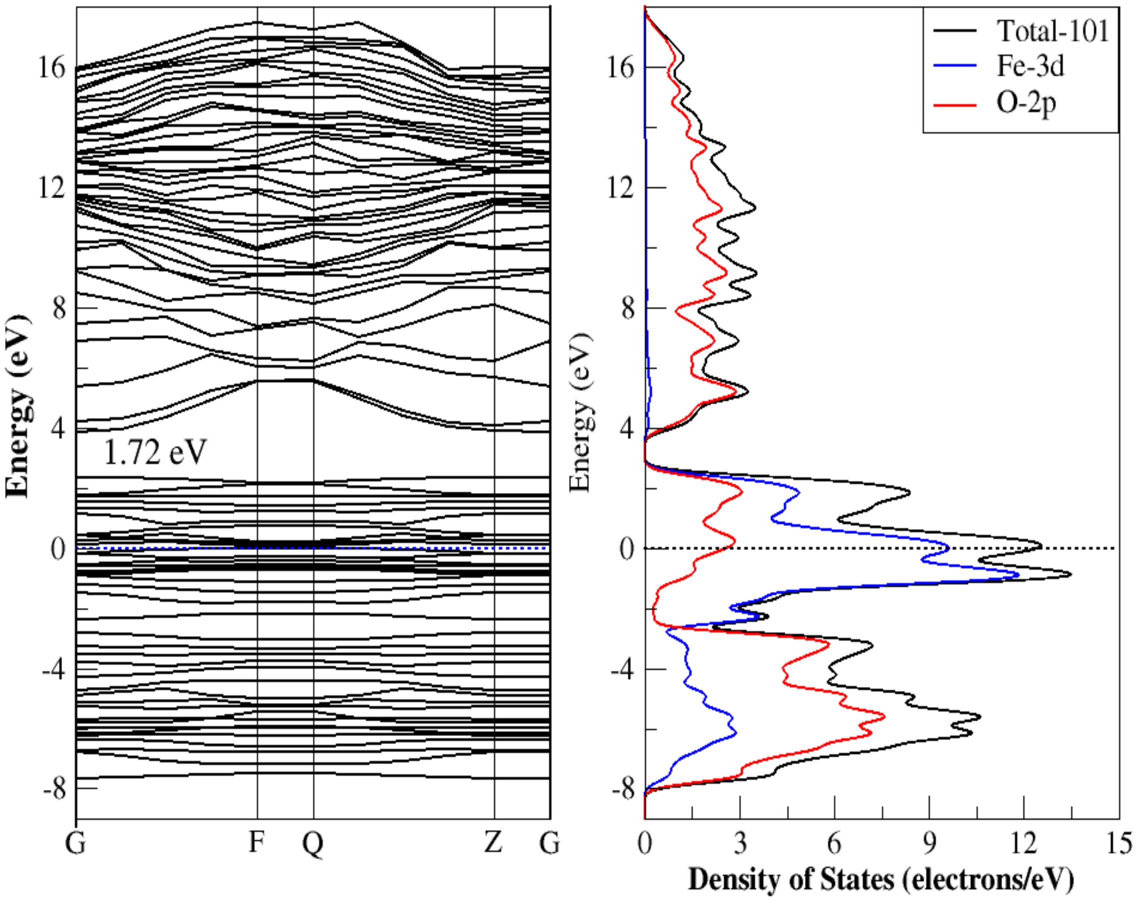

Figure 30:Undoped α-Fe_2O_3 (101) surface electronic band and DOS plot.

The absorption of incident photons, the generation of electron–hole pairs, the migration of carriers, and the redox capability of excited-state electrons and holes are all determined by the energy band-edge structure of a semiconductor; thus, the effect of doping on electronic properties of α-Fe_2O_3 (101) surface is discussed in this section. According to Simfukwe *et al.*, narrow band gap semiconductors with good optical absorption capabilities are more likely to harvest low-energy photons efficiently [27].

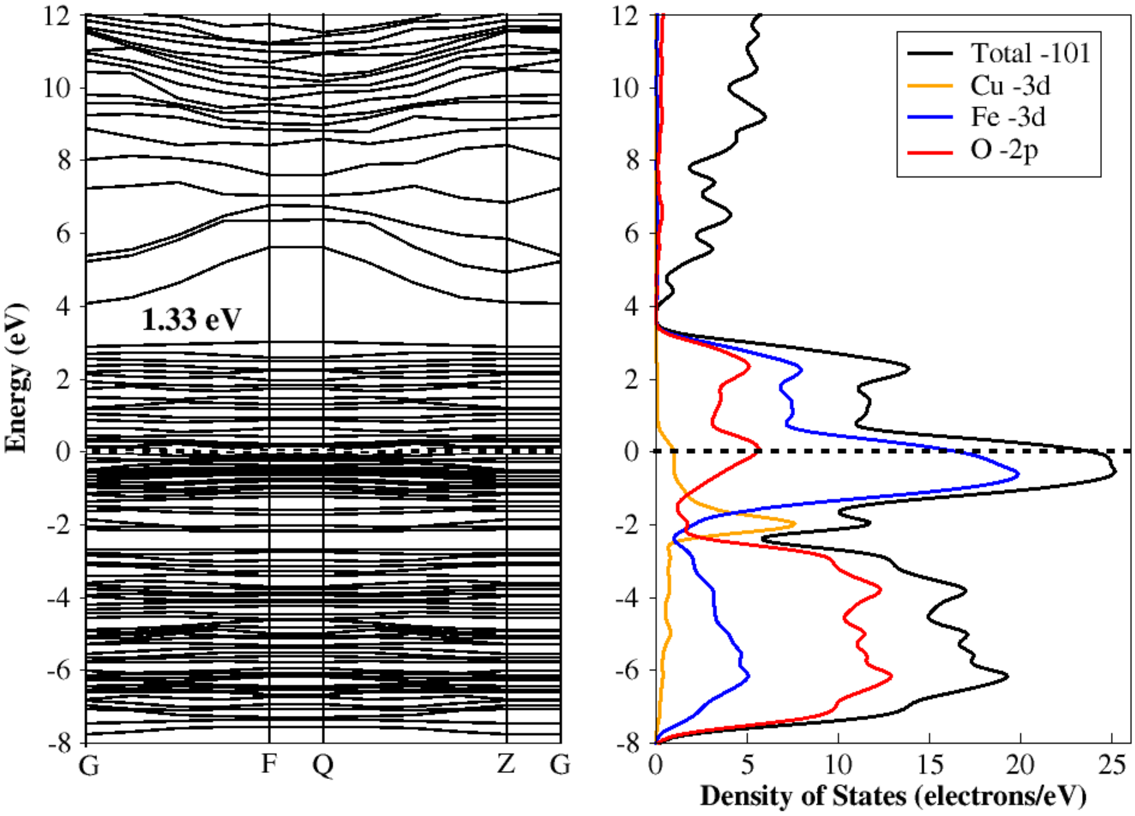

Figure 31: Cu-doped α-Fe_2O_3 (101) surface band structure and DOS plot.

Figure 31 depicts the electronic band structure for Cu-doped α-Fe_2O_3 surface (101) and the density of states. Cu-3d states are introduced in the valence band, leading to the substantial reduction of the band gap to a size of 1.33 eV. Cu-3d states are observed in the valence band, responsible for narrowing the band gap by 0.39 eV. The conduction band, however, shows a very low energy of the DOS at the conduction band. At around – 2 eV, we observe that the Cu *3d* electrons have shifted the Fe-3d states a little to a higher energy level and resulted in a peak in that energy level. With very little evidence of O-2p states from energy 4 eV to 16 eV, we can affirm that the hybridization on this band is linking the O-2p and Fe-3d states. More photons in the sun spectrum can be absorbed due to a narrow band gap [83],[94].

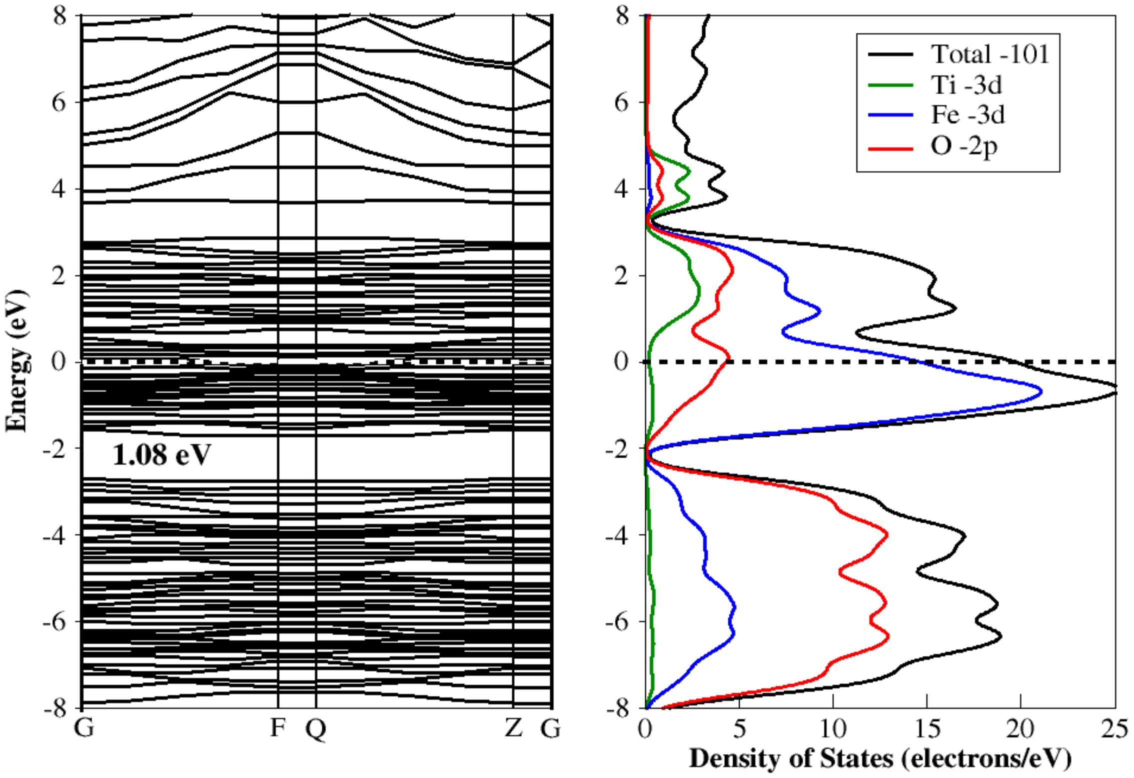

Figure 32: Ti-doped α-Fe_2O_3 (101) surface band structure and DOS plot.

For the Ti-doped α-Fe_2O_3 (101) surface, the 3d states of the substituted titanium contribute to the reduction of the band gap of 1.08 eV, as shown on the electronic band structure in Figure 32. The DOS plot indicates that Ti *3d* states are contributing to the conduction band, and thus may be the reason for the narrow and gap. On the other hand, Ti modifies the CBM by introducing the Ti *3d* state to the empty states of Fe-3d, shifting the CMB edge towards the valence band. The characters of the DOS plot of Ti-doped (101) surface show that O-2p states are the main contributors in the VB with characters of Fe-3d states at the lowest energy level; while the CB depicts mainly the Fe-3d states exhibiting the highest energy of the density of states and minor peak of Ti *3d* state at energy of 3 eV. A narrow band reduces a pathway for excited charges; through the intermediate level in the band gap, electrons in the valence band edge can be excited by the low-energy photons to the conduction band edge. Thus, α-Fe_2O_3 with Ti is expected to generate more electron–hole pairs than the undoped hematite surface. In addition, the narrower gap (1.08 eV) also contributes to the enhancement of the carrier concentration. In summary, the enhancement of carrier concentration is a primary reason for a better photocatalytic performance, which is confirmed by experiments [95].

The ionic radii of the first-row transition metal cations are comparable to those of Fe, but they have a different number of 3d electrons, resulting in distinct stable oxidation states [96]. Figure 33 shows the computed band structure and DOS for Ni-doped α-Fe_2O_3 (101) surface. The calculations follow similar trend as of the Cu and Ti doped surfaces, all of which result in a narrow band gap. The Ni-doped (101) surface gives a calculated band gap of 1.18 eV; however, the Ni-3d orbitals are observed to be contributing minority states on both the valence and conduction bands.

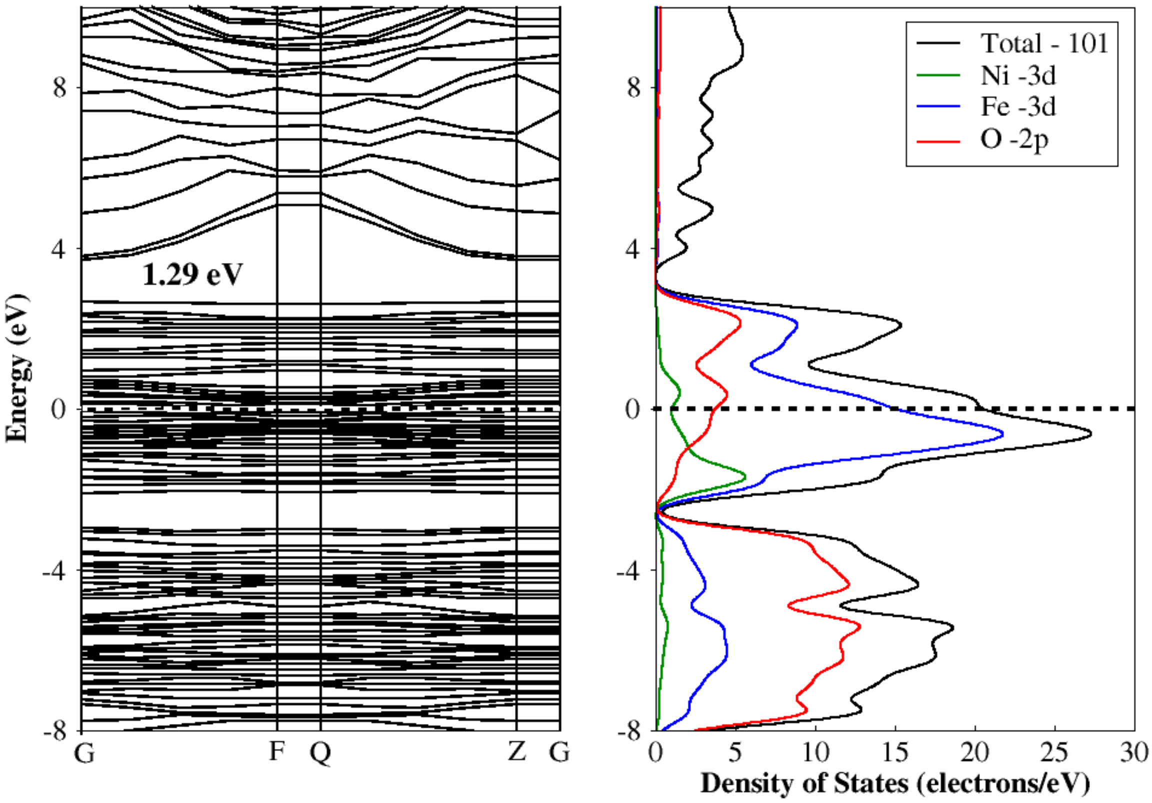

Figure 33: Ni-doped α-Fe_2O_3 (101) surface band structure and DOS plot.

The occupied states around the Fermi energy are of mixed Fe-3d and O-2p character, whereas most Ni-3d states are just below the Fermi level at an approximated energy of -1 eV. Notably, the Fermi level is found within the valence band, which may be due to a down shift of the conduction band edge. For the Ni-doped hematite surface, we observe a peak of Fe-3d electrons which appears right between energy 3 to -3 eV, and it is the major contributor at this level. The signal indicates that Fe^{2+} cations with one minority spin of a 3d electron occur because of Ni^{4+} cation replacement. The DOS of Ni demonstrates that majority states in the VB are more occupied than minority states in the CB, which are partially filled. The trend of these results is similar with prior work on a transition metal-doped hematite by Velev *et al*. using the local density approximation (LDA) +U approach on a transition metal-doped hematite [97].

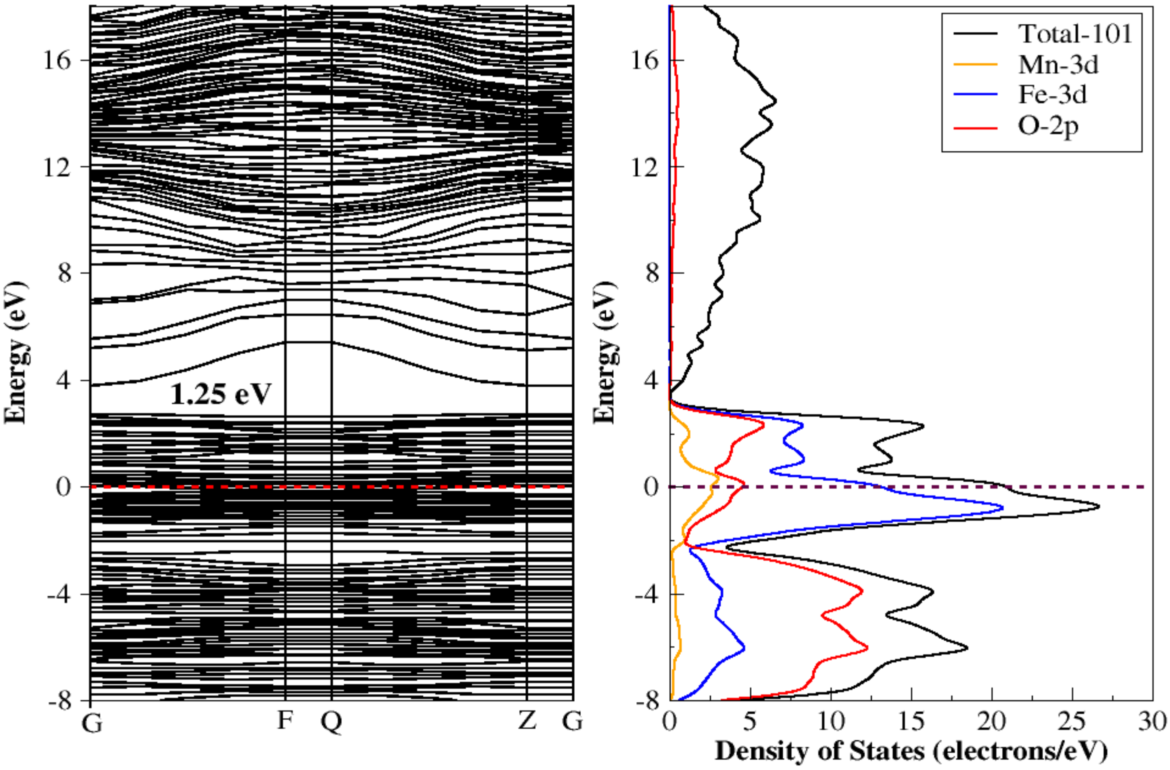

Figure 34: Mn-doped α-Fe_2O_3 (101) surface band structure and DOS plot.

The effect of Mn doping on hematite is investigated and results in a narrowed band gap. In simplified details, according to the DOS analysis in Figure 34, Mn modifies the VBM by introducing the 3d state to the empty states of Fe-3d, shifting toward the conduction band. However, the Mn, 3d states do not contribute much to the CB. The electronic band structure gives a band gap of 1.25 eV, which shows a major peak at the Fermi level contributed by the O-2p, Fe-3d, and Mn-3d states.

Table 4 summarizes the energy band gap and the adsorption energies (calculated using Equation 35) of the pure and doped α-Fe_2O_3 (101) surface. All the results show a positive adsorption value, suggesting stable doping of the doped atoms into α-Fe_2O_3 (101) surface.

Table 4: The energy band gap, and adsorption energies for doped and undoped α-Fe_2O_3 (101) surface.

Dopant	Band gap $(E_g)\ eV$	Adsorption energy ($(E_{ad})\ eV$
Cu	1.33	2.406
Ti	1.08	4.205
Ni	1.29	2.682
Mn	1.25	4.042
Pure	1.72	0

The calculated adsorption energies indicate that Ti-doped α-Fe_2O_3 (101) surface with energy 4.205 eV is greater than the other systems. This implies that the Ti metal reacts more strongly to α-Fe_2O_3 (101) than the other transition metals.

4.4.2 Optical properties for α-Fe_2O_3 (101) surface

Figure 35 shows the dielectric function against frequency for all the doped systems and the undoped surface. We observe that real part$\varepsilon_1(\omega)$ and imaginary part $\varepsilon_2(\omega)$ rapidly decrease with increasing frequency and then remains almost constant at higher frequencies for all doped surfaces. The real part shows that the first energy peaks at about 4 to 5 eV belong to the electronic transition from Fe *3d* to O-2p at the conduction band and valence band. This was observed from all band structures (Figures 31 – 34) where O-2p dominates the VB and a transition, and CB is dominated by Fe-3d, this is also confirmed by previous work [86].

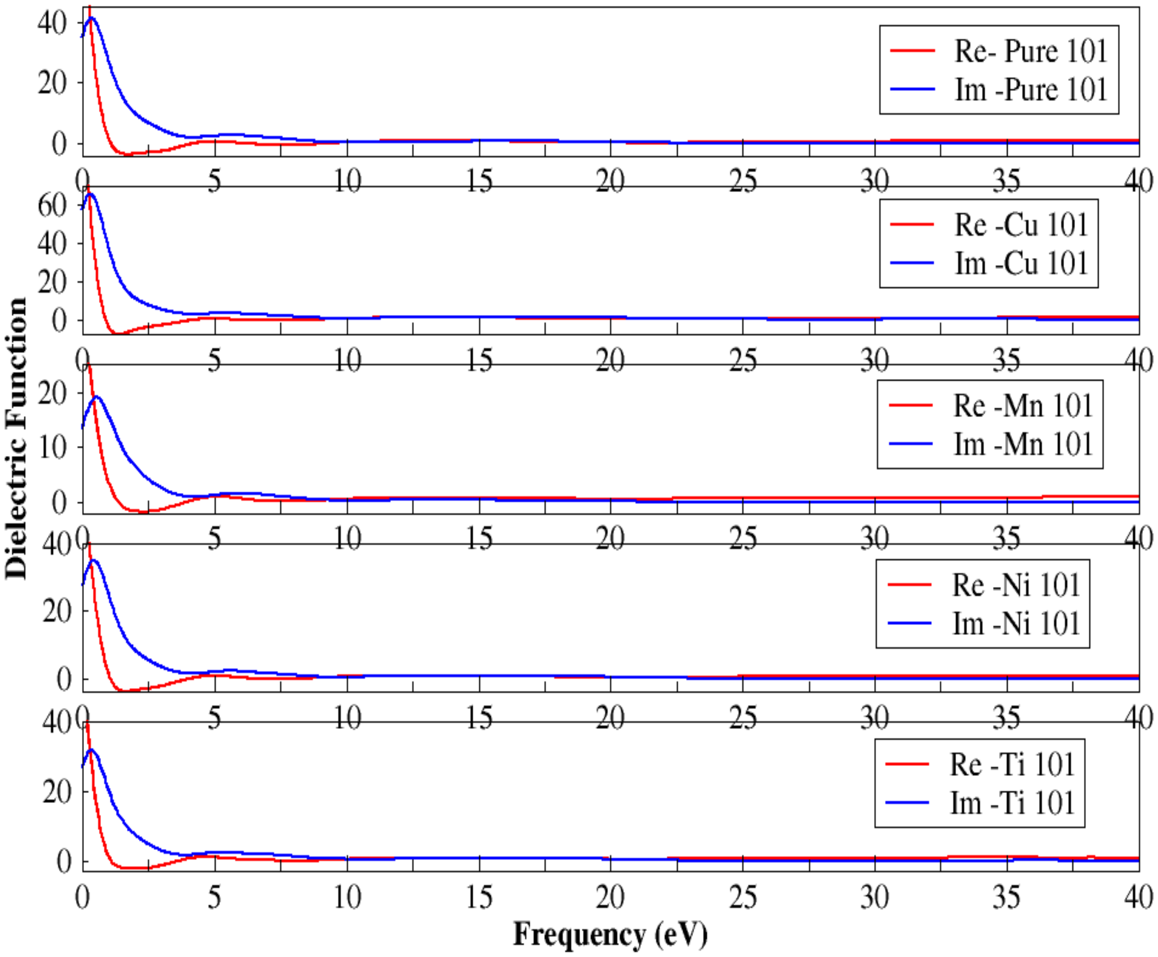

Figure 35: Dielectric function for undoped and doped α-Fe_2O_3 (101) surface.

We also plotted the absorption and conductivity spectrum as a function of the wavelength for copper, nickel, titanium, and manganese doped α-Fe_2O_3 (101) surfaces (101) compared to undoped α-Fe_2O_3 surface (101) as shown in Figures 36 and 37, respectively. As previously stated, the absorption coefficient $\alpha(\omega)$ is derived through the dielectric function.

Figure 36 shows Ni-, Ti- and Mn-doped α-Fe_2O_3 surface (101) depicting peaks with the highest absorptive coefficient in the UV region at wavelength 200 nm and the lowest absorption in the visible light region. Thus, the surfaces are more absorptive in the UV region than in the visible light region when compared to the undoped surface. However, at wavelengths 300 to 450 nm, Ni and Mn display much more absorptive coefficients when compared to the pure surface, while Ti responds very weakly, being the least absorbing surface. From 450 to 800 nm, the undoped surface is slightly more than the other doped surface except Cu-doped surface.

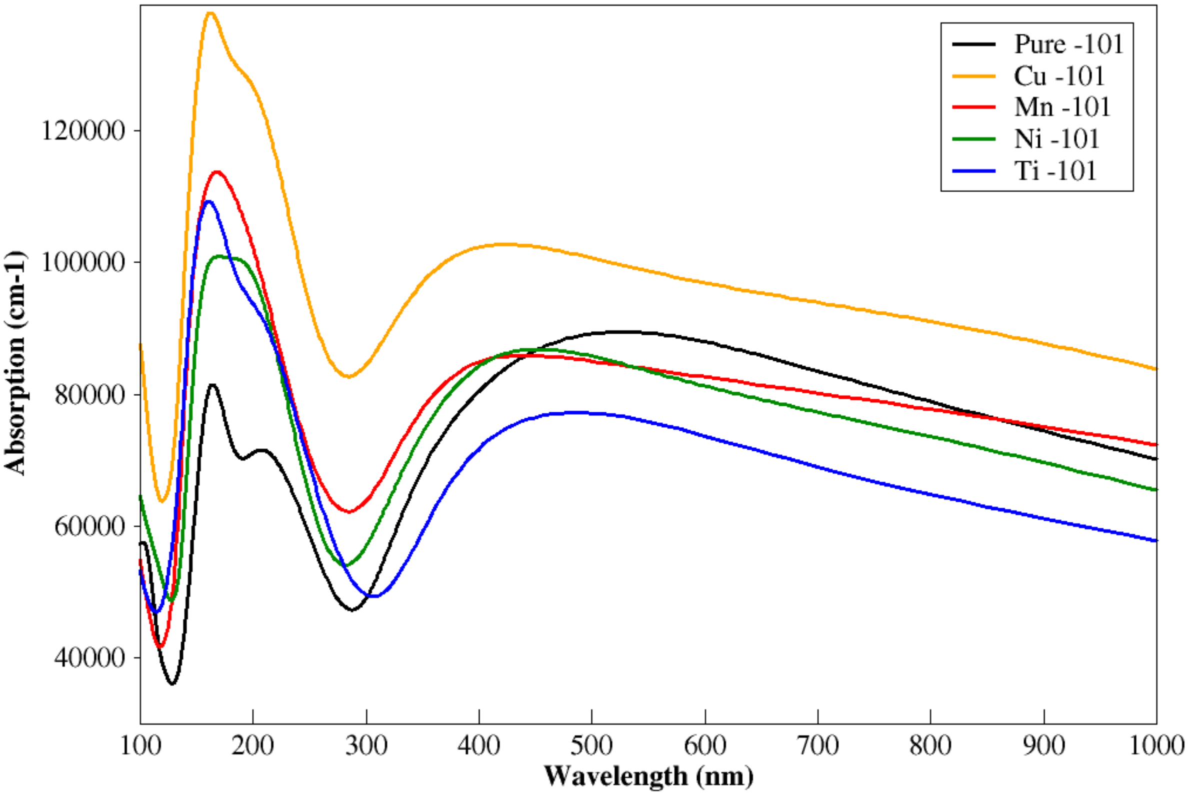

Figure 36: Optical Absorption spectra of pure α-Fe_2O_3 (101) surface compared with Cu-, Ti-, Ni- and Mn-doped surfaces.

A semiconductor with a narrow band gap is expected to absorb more photons in the visible region than that of wider band gap, hence it exhibits a much greater absorption coefficient in this region [44]. Ti-doped α-Fe_2O_3 (101) has the narrowest band gap compared to the pure surface. On the contrary, Ti doped displays the lowest absorption coefficient in the visible region, this could possibly be a reason suggested by Pan *et al.,* stating that the indirect transitions (Fe-3d ~ Fe-3d), are not strongly absorptive in visible light range [83]. Evidence from the surface band structure in Figures 30-33 show that the edge of the VBM is dominated by the Fe *3d* electron; therefore, even with the narrowest band gap these surfaces may not convey a higher absorptive coefficient due to this possible reason.

Meanwhile, the Cu-doped α-Fe_2O_3 surface is responding in both the UV and visible light region, showing the highest peak at wavelength 200 nm and 400 nm. Cu-doped surface exhibits the greatest absorption coefficient throughout the whole targeted visible light region spectrum.

The real and imaginary parts of the conductivity against wavelength are shown in Figure 37. The real part gives information about how much a material can conduct due to the electric field created by excited electrons in a semiconductor [90],[50].

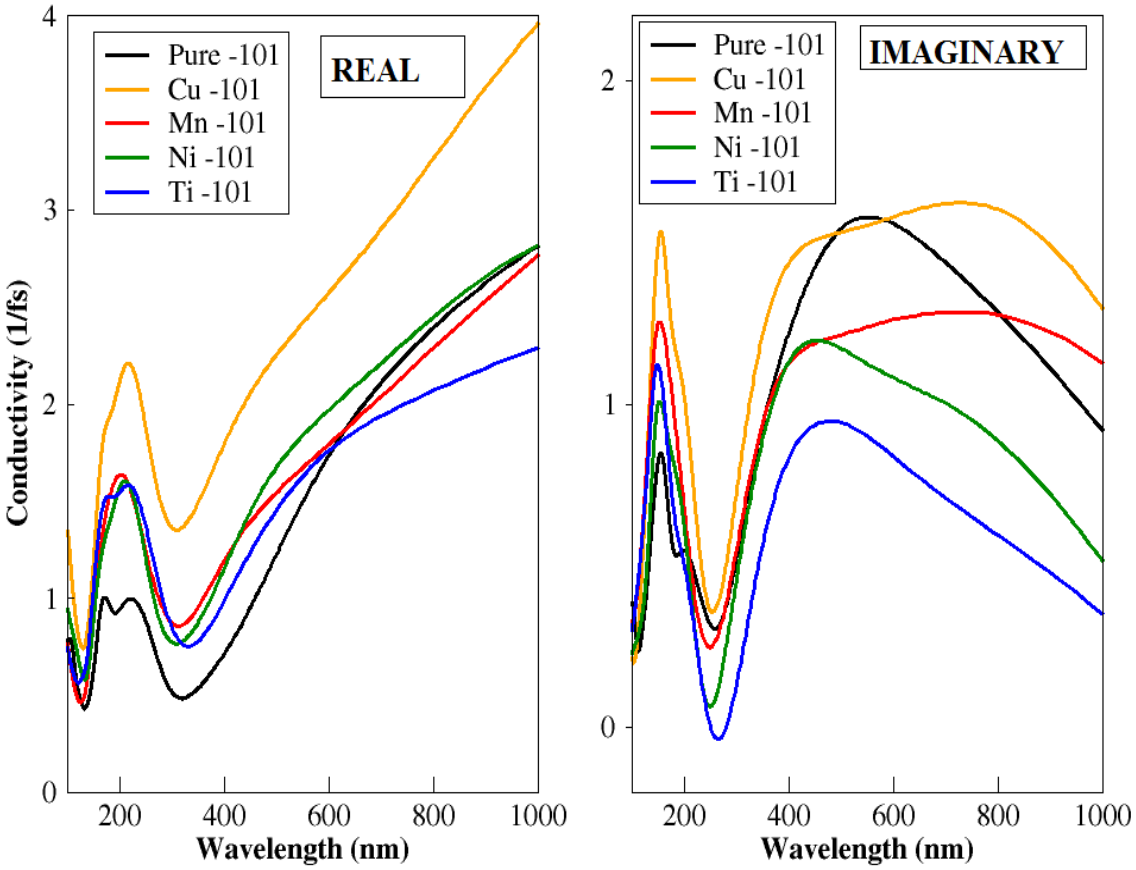

Figure 37: Conductivity of Ti-, Cu-, Ni- and Mn-doped α-Fe_2O_3 vs undoped α-Fe_2O_3 (101) surface.

The real part of the conductivity shows that the Cu-doped α-Fe_2O_3 surface exhibits a higher conductivity; this is in relation with the fact that the Cu-doped α-Fe_2O_3 (101) surface sets off a higher coefficient of absorption and due to an increase in electron carrier concentration, the surface is likely to display a faster rate of flow of charge and hence set high the conductivity. The other doped α-Fe_2O_3 (101) surfaces, show the highest peaks in the UV region more than the undoped surface at wavelength 200 nm. Nickel becomes the second conducting surface in the visible light region (400-700 nm). While manganese- and titanium-doped α-Fe_2O_3 (101) surfaces, also conduct in the in visible light region only at wavelengths 400 nm to 600 nm after the undoped surface.

5. Conclusion

This study focused on enhancing the photocatalytic properties α-Fe_2O_3 by improving the optical properties of α-Fe_2O_3 through doping with transition metals.

Using first-principles computational approach, we explored the electronic and optical properties of two optimized hematite (001) and (101) surfaces doped with Cu, Ti, Ni and Mn. DFT and DFT+U methods were used in this study to carry out the objectives of the study. DFT+U gave a reasonable prediction of the electronic properties than DFT, while DFT was proficient in the optical properties of bulk α-Fe_2O_3, thus for surface calculations DFT was adopted since the study aimed at improving the photocatalytic activities of α-Fe_2O_3.

Electronic and optical properties for doped and undoped α-Fe_2O_3 (001), were investigated using DFT for water-splitting solar cells. The results confirm that the pure surfaces of hematite exhibit weak optical properties while and thedoping with transition metals slightly improved the optical properties of α-Fe_2O_3, this is observed by comparing the absorbance spectra for doped and undoped surfaces. For the doped α-Fe_2O_3 (001) surface, calculations show that all doped surfaces absorb more in the UV region than in the visible region, with that stated, Mn-doped α-Fe_2O_3 set out a great improvement in the absorption coefficient in the visible region than the other surfaces, including the undoped surface owing to its narrow energy band gap of 1.3 eV. Furthermore, Mn is also found to have enhanced the conductivity of α-Fe_2O_3 as it constituted the proficient conducting surface followed by Ni. Calculations on the absorption and conductivity of the Fe_2O_3 (101) surface show that Cu is the most efficient dopant to improve visible light absorption; it showed to have a great influence in the absorption property of Fe_2O_3 (101) surface.

In summary, the performance of Cu-, Ti-, Ni-, and Mn-doped hematite is investigated to improve optical absorption and conductivity using DFT calculations. The results suggest that doping Cu, Ti, Ni, and Mn can effectively reduce the band gap and change surface properties, leading to an excellent absorption property in the visible region. On both (001) and (101) surfaces, we observed similar characteristics, for example, 3d orbitals of transition metals can increase the charge carrier density and thus, improve the electrical conductivity of α-Fe_2O_3. Furthermore, one of the shortcomings faced by α-Fe_2O_3 to realize spontaneous hydrogen production in visible light driven by PEC water splitting is low optical absorption due to the indirect band gap, the results of this study show to have addressed the drawback of low absorption coefficient in α-Fe_2O_3.

References

[1] A. Darmani, N. Arvidsson, A. Hidalgo, and J. Albors, “What drives the development of renewable energy technologies? Toward a typology for the systemic drivers,” *Renew. Sustain. Energy Rev.*, vol. 38, pp. 834–847, 2014.

[2] S. E. Hosseini and M. A. Wahid, “Hydrogen production from renewable and sustainable energy resources: Promising green energy carrier for clean development,” *Renew. Sustain. Energy Rev.*, vol. 57, pp. 850–866, 2016.

[3] A. K. Aliyu, B. Modu, and C. W. Tan, “A review of renewable energy development in Africa: A focus in South Africa, Egypt and Nigeria,” *Renew. Sustain. Energy Rev.*, vol. 81, no. February 2016, pp. 2502–2518, 2018.

[4] P. K. Wesseh and B. Lin, “Can African countries efficiently build their economies on renewable energy?,” *Renew. Sustain. Energy Rev.*, vol. 54, pp. 161–173, 2016.

[5] A. V. Da Rosa and J. C. Ordonez, “Fundamentals of renewable energy processes,” in *Academic Press*, 2021, pp. 22–24.

[6] W. P. Siripala, “Hydrogen Energy and Photoelectrolysis of Water,” *Inst. Phys. – Sri Lanka*, vol. 20, no. June, pp. 67–73, 2004.

[7] H. Lund, “Renewable energy strategies for sustainable development,” *Energy*, vol. 32, no. 6, pp. 912–919, 2007.

[8] S. R. Bull, “Renewable energy today and tomorrow,” *Proc. IEEE*, vol. 89, no. 8, pp. 1216–1226, 2001.

[9] R. Gross, M. Leach, and A. Bauen, “Progress in renewable energy,” *Environ. Int.*, vol. 29, no. 1, pp. 105–122, 2003.

[10] I. M. Bugaje, “Renewable energy for sustainable development in Africa: A review,” *Renew. Sustain. Energy Rev.*, vol. 10, no. 6, pp. 603–612, 2006.

[11] R. Adib, “Renewables 2015 Global Status Report Distrbuted Renewable Energy For Energy Access,” no. September, 2015.

[12] Department of Energy, Department of National Treasury, Development Bank of Southern Africa, Department of Minerals and Energy, and Department of Basic Education, “Independent Power Producers Procurement Programme,” *White Pap.*, vol. 583, no. 31 December, pp. 10–12, 2015.

[13] M. Gratzel, “Photoelectrochemical cells,” *Nature*, vol. 414, pp. 338–344, 2001.

[14] E. Kabir, P. Kumar, S. Kumar, A. A. Adelodun, and K. H. Kim, “Solar energy: Potential and future prospects,” *Renew. Sustain. Energy Rev.*, vol. 82, no. September 2016, pp. 894–900, 2018.

[15] M. Frey and R. Robson, *Hydrogen as a Fuel Learning from Nature Edited by Richard Cammack*. 2001.

[16] G. Gurudayal *et al.*, “Improving the efficiency of hematite nanorods for photoelectrochemical water splitting by doping with manganese,” *ACS Appl. Mater. Interfaces*, vol. 6, no. 8, pp. 5852–5859, 2014.

[17] Y. Lin, G. Yuan, S. Sheehan, S. Zhou, and D. Wang, “Hematite-based solar water splitting: Challenges and opportunities,” *Energy Environ. Sci.*, vol. 4, no. 12, pp. 4862–4869, 2011.

[18] N. S. Lewis and D. G. Nocera, “Powering the planet: Chemical challenges in solar energy utilization,” *Proc. Natl. Acad. Sci. U. S. A.*, vol. 103, no. 43, pp. 15729–15735, 2006.

[19] A. G. Tamirat, J. Rick, A. A. Dubale, W. N. Su, and B. J. Hwang, “Using hematite for photoelectrochemical water splitting: A review of current progress and challenges,” *Nanoscale Horizons*, vol. 1, no. 4, pp. 243–267, 2016.

[20] M. G. Walter *et al.*, “Solar Water Splitting Cells,” *Chem. Rev.*, vol. 110, no. 11, pp. 6446–6473, 2010.

[21] W. J. Youngblood, S. H. Anna Lee, K. Maeda, and T. E. Mallouk, “Visible light water splitting using dye-sensitized oxide semiconductors,” *Acc. Chem. Res.*, vol. 42, no. 12, pp. 1966–1973, 2009.

[22] S. D. Tilley, M. Cornuz, K. Sivula, and M. Grätzel, “Light-inducedwater splitting with hematite: Improved nanostructure and iridium oxide catalysis,” *Angew. Chemie - Int. Ed.*, vol. 49, no. 36, pp. 6405–6408, 2010.

[23] A. Fujishima and K. Honda, “Electrochemical Photolysis of Water at a Semiconductor Electrode,” *Nature*, vol. 238, pp. 37–38, 1972.

[24] S. R. Pendlebury, “Charge Carrier Dynamics in Hematite Photoanodes for Solar Water Oxidation,” 2012.

[25] Z. Li, W. Luo, M. Zhang, J. Feng, and Z. Zou, “Photoelectrochemical cells for solar hydrogen production: Current state of promising photoelectrodes, methods to improve their properties, and outlook,” *Energy Environ. Sci.*, vol. 6, no. 2, pp. 347–370, 2013.

[26] S. Shen, J. Jiang, P. Guo, C. X. Kronawitter, S. S. Mao, and L. Guo, “Effect of Cr doping on the photoelectrochemical performance of hematite nanorod photoanodes,” *Nano Energy*, vol. 1, no. 5, pp. 732–741, 2012.

[27] J. Simfukwe; R. Edwin Mapasha; A. Braun and M. Diale, “Density Functional Theory study of Cu doped {0001} and {0112} surfaces of hematite for water splitting,” South Africa, Pretoria, 2018.

[28] S. Chen, T. Takata, and K. Domen, “Particulate photocatalysts for overall water splitting,” *Nat. Rev. Mater.*, vol. 2, no. August, pp. 1–17, 2017.

[29] H. Ahmad, S. K. Kamarudin, L. J. Minggu, and M. Kassim, “Hydrogen from photo-catalytic water splitting process: A review,” *Renew. Sustain. Energy Rev.*, vol. 43, pp. 599–610, 2015.

[30] T. Jafari, E. Moharreri, A. S. Amin, R. Miao, W. Song, and S. L. Suib,

"Photocatalytic water splitting - The untamed dream: A review of recent advances," *Molecules*, vol. 21, no. 7, 2016.

[31] J. Ran, J. Zhang, J. Yu, M. Jaroniec, and S. Z. Qiao, "Earth-abundant cocatalysts for semiconductor-based photocatalytic water splitting," *Chem. Soc. Rev.*, vol. 43, no. 22, pp. 7787–7812, 2014.

[32] C. Ding, J. Shi, Z. Wang, and C. Li, "Correction to: Photoelectrocatalytic water splitting: Significance of cocatalysts, electrolyte, and interfaces (ACS Catalysis (2017) 7:1 (675-688) DOI: 10.1021/acscatal.6b03107)," *ACS Catal.*, vol. 7, no. 3, p. 1706, 2017.

[33] J. Yang, D. Wang, H. Han, and C. A. N. Li, "Roles of co-catalysts in photocatalysis and photoelectrocatalysis," *Accounts Chem. Reasearch*, vol. 46, no. 8, pp. 1900–1909, 2013.

[34] P. Zhang, T. Wang, X. Chang, L. Zhang, and J. Gong, " Synergistic cocatalytic effect of carbon nanodots and Co_3O_4 nanoclusters for the photoelectrochemical water Oxidation on hematite ," *Angew. Chemie*, vol. 128, no. 19, pp. 5945–5949, 2016.

[35] K. Maeda, K. Teramura, D. Lu, N. Saito, Y. Inoue, and K. Domen, "Noble-metal/Cr_2O_3 core/shell nanoparticles as a cocatalyst for photocatalytic overall water splitting," *Angew. Chemie - Int. Ed.*, vol. 45, no. 46, pp. 7806–7809, 2006.

[36] J. B. Klahr, S.Gimenez, F. Fabregat-Santiago, J.Bisquert, T. W. Hamann, "Photoelectrochemical and impedance spectroscopic investigation of water oxidation with 'Co–Pi'-coated hematite electrodes," *J. Am. Chem. Soc.*, vol. 134, no. 40, pp. 16693–16700, 2012.

[37] J. Yang *et al.*, "A multifunctional biphasic water splitting catalyst tailored for integration with high-performance semiconductor photoanodes," *Nat. Mater.*, vol. 16, no. 3, pp. 335–341, 2017.

[38] D. A. Wheeler, G. Wang, Y. Ling, Y. Li, and J. Z. Zhang, "Nanostructured hematite: Synthesis, characterization, charge carrier dynamics, and photoelectrochemical properties," *Energy Environ. Sci.*, vol. 5, no. 5, pp. 6682–6702, 2012.

[39] J. A. Glasscock, P. R. F. Barnes, I. C. Plumb, A. Bendavid, and P. J. Martin, "Structural, optical and electrical properties of undoped polycrystalline hematite thin films produced using filtered arc deposition," *Thin Solid Films*, vol. 516, no. 8, pp. 1716–1724, 2008.

[40] S. S. Shinde, R. A. Bansode, C. H. Bhosale, and K. Y. Rajpure, "Physical properties of hematite α-Fe_2O_3 thin films: Application to photoelectrochemical solar cells," *J. Semicond.*, vol. 32, no. 1, pp. 1–8, 2011.

[41] J. Tucek *et al.*, "Iron(III) oxide polymorphs and their manifestations in in-field 57Fe Mossbauer spectra," *AIP Conf. Proc.*, vol. 1489, no. October, pp. 56–74, 2012.

[42] N. Dzade, A. Roldan, and N. de Leeuw, "A density functional theory Study of the

adsorption of benzene on hematite (α-Fe_2O_3) Surfaces," *Minerals*, vol. 4, no. 1, pp. 89–115, 2014.

[43] H. Pan, X. Meng, J. Cai, S. Li, and G. Qin, "4d transition-metal doped hematite for enhancing photoelectrochemical activity: Theoretical prediction and experimental confirmation," *RSC Adv.*, vol. 5, no. 25, pp. 19353–19361, 2015.

[44] M. N. Huda, A. Walsh, Y. Yan, S. H. Wei, and M. M. Al-Jassim, "Electronic, structural, and magnetic effects of 3d transition metals in hematite," *J. Appl. Phys.*, vol. 107, no. 12, 2010.

[45] J. Mock *et al.*, "Oxygen vacancy doping of hematite analyzed by electrical conductivity and thermoelectric power measurements," *Phys. Rev. Mater.*, vol. 1, no. 6, pp. 1–11, 2017.

[46] X. Y. Meng *et al.*, "Enhanced photoelectrochemical activity for Cu and Ti doped hematite: The first principles calculations," *Appl. Phys. Lett.*, vol. 98, no. 11, pp. 1–4, 2011.

[47] K. D. Malviya *et al.*, "Influence of Ti doping levels on thephotoelectrochemical properties of thin-film hematite (α-Fe_2O_3) Photoanodes," *J. Phys. Chem. C*, vol. 121, no. 8, pp. 4206–4213, 2017.

[48] P. Liao, M. C. Toroker, and E. A. Carter, "acs_NL_nl-2011-00356n 1..7," pp. 1–7, 2011.

[49] J. An, P. Wanaguru, C. Xia, M. Tao, and Q. Zhang, "First-principles study of sulfur atom doping and adsorption on α–Fe_2O_3 (0001) film," *Phys. Lett. Sect. A Gen. At. Solid State Phys.*, vol. 380, no. 38, pp. 3149–3154, 2016.

[50] S. Kronawitter, C X. Zegkinoglou, I. Shen, "Titanium Incorporation into hematite photoelectrodes: Theoretical considerations and experimental observations," *Encycl. Environ. Chang.*, 2014.

[51] X. G. Wang *et al.*, "The hematite (α-Fe_2O_3) (0001) surface: Evidence for domains of distinct chemistry," *Phys. Rev. Lett.*, vol. 81, no. 5, pp. 1038–1041, 1998.

[52] W. Cui *et al.*, "Comparative study on surface structure, electronic properties of sulfide and oxide minerals: A first-principles perspective," *Minerals*, vol. 9, no. 6, pp. 12–14, 2019.

[53] S. min Chang and W. szu Liu, "Surface doping is more beneficial than bulk doping to the photocatalytic activity of vanadium-doped TiO_2," *Appl. Catal. B Environ.*, vol. 101, no. 3–4, pp. 333–342, 2011.

[54] E. F. Sheka, E. A. Nikitina, V. A. Zayets, I. Y. Ginzburg, and J. Schoonman, "Carboxylic species adsorption on TiO_2 nanoparticles," *Phys. Solid State*, vol. 49, no. 1, pp. 154–163, 2007.

[55] M. Landmann, E. Rauls, and W. G. Schmidt, "The electronic structure and optical response of rutile, anatase and brookite TiO_2," *J. Phys. Condens. Matter*, vol. 24, no. 19, 2012.

[56] D. M. Brink, “Density functional theory,” *Nucl. Phys. News*, vol. 12, no. 4, pp. 27–32, 2002.

[57] M. D. Segall *et al.*, “First-principles simulation: Ideas, illustrations and the CASTEP code,” *J. Phys. Condens. Matter*, vol. 14, no. 11, pp. 2717–2744, 2002.

[58] J. Riess and W. Münch, “The theorem of hohenberg and kohn for subdomains of a quantum system,” *Theor. Chim. Acta*, vol. 58, no. 4, pp. 295–300, 1981.

[59] P. Hohenberg and W. Kohn, “Inhomogeneous Electron Gas,” *Phys. Rev. B*, pp. 136, 864, 1964.

[60] W. Kohn, A. Savin, and C. A. Ullrich, “Hohenberg-Kohn theory including spin magnetism and magnetic fields,” *Int. J. Quantum Chem.*, vol. 100, no. 1, pp. 20–21, 2004.

[61] D. M. Ceperley and B. J. Alder, “Ground state of the electron gas by a stochastic method,” *Phys. Rev. Lett.*, vol. 45, no. 7, pp. 566–569, 1980.

[62] J. P. Perdew, K. Burke, and M. Ernzerhof, “Generalized gradient approximation made simple,” *Phys. Rev. Lett.*, vol. 77, no. 18, pp. 3865–3868, 1996.

[63] W. Kohn and L. J. Sham, “Self-consistent equations including exchange and correlation effects,” *Phys. Rev.*, vol. 140, no. 4A, 1965.

[64] A. F. Oliveira, G. Seifert, T. Heine, and H. A. Duarte, “Density-functional based tight-binding: An approximate DFT method,” *J. Braz. Chem. Soc.*, vol. 20, no. 7, pp. 1193–1205, 2009.

[65] A. Stan, N. E. Dahlen, and R. Van Leeuwen, “Levels of self-consistency in the GW approximation,” *J. Chem. Phys.*, vol. 130, no. 11, pp. 1–11, 2009.

[66] D. Joubert, “From ultrasoft pseudopotentials to the projector augmented-wave method,” *Phys. Rev. B - Condens. Matter Mater. Phys.*, vol. 59, no. 3, pp. 1758–1775, 1999.

[67] J. Hutter, “Excited state nuclear forces from the Tamm-Dancoff approximation to time-dependent density functional theory within the plane wave basis set framework,” *J. Chem. Phys.*, vol. 118, no. 9, pp. 3928–3934, 2003.

[68] S. J. Clark *et al.*, “First principles methods using CASTEP,” *Zeitschrift für Krist.*, vol. 220, no. 5-6–2005, pp. 567–570, 2005.

[69] G. Kresse and J. Furthmiiller, “Efficiency of ab-initio total energy calculations for metals and semiconductors using a plane-wave basis set av *,” vol. 6, pp. 15–50, 1996.

[70] S. L. Dudarev, G. A. Botton, S. Y. Savrasov, C. J. Humphreys, and A. P. Sutton, “Electron-energy-loss spectra and the structural stability of nickel oxide: An LSDA+U study,” *Phys. Rev. B*, vol. 57, no. 3, pp. 1505–1509, 1998.

[71] S. Dudarev and A. Liechtenstein, “Surface states on NiO (100) and the origin of the contrast reversal in atomically resolved scanning tunneling microscope images,” *Phys. Rev. B - Condens. Matter Mater. Phys.*, vol. 56, no. 8, pp. 4900–

4908, 1997.

[72] B. A. A. Sarah A. Tolba, Kareem M. Gameel and H. A. A. and N. K. Allam, “The DFT+U: Approaches, Accuracy, and Applications,” *Intech*, vol. 32, no. tourism, pp. 137–144, 1989.

[73] Z. Lyu, S. Niu, C. Lu, G. Zhao, Z. Gong, and Y. Zhu, “A density functional theory study on the selective catalytic reduction of NO by NH3 reactivity of α-Fe2O3 (0 0 1) catalyst doped by Mn, Ti, Cr and Ni,” *Fuel*, vol. 267, no. October 2019, p. 117147, 2020.

[74] T. Ranwaha, I. Elegbeleye, N. Maluta, and R. Maphanga, “Optical and electronic properties of croconates dye molecules adsorbed on TiO_2 brookite nanocluster for dye sensitized solar cells application,” *Mater. Express*, vol. 10, no. 11, pp. 1917–1924, 2020.

[75] J. An, P. Wanaguru, C. Xia, M. Tao, and Q. Zhang, “First-principles study of sulfur atom doping and adsorption on α–Fe_2O_3(0001) film,” *Phys. Lett. Sect. A Gen. At. Solid State Phys.*, vol. 380, no. 38, pp. 3149–3154, 2016.

[76] Hendrik J Monkhorst and J. D. Pack, “Special points for Brillouin-zone integration Monkhorst and Pack,” *Physical Review B*, vol. 13, no. 12. pp. 5188–5192, 1976.

[77] H. Pan, X. Meng, and G. Qin, “Hydrogen generation by water splitting on hematite (0001) surfaces: First-principles calculations,” *Phys. Chem. Chem. Phys.*, vol. 16, no. 46, pp. 25442–25448, 2014.

[78] N. Snir, N. Yatom, and M. Caspary Toroker, “Progress in understanding hematite electrochemistry through computational modeling,” *Comput. Mater. Sci.*, vol. 160, no. January, pp. 411–419, 2019.

[79] K. Sivula, F. Le Formal, and M. Grätzel, “Solar water splitting: Progress using hematite (α-Fe_2O_3) photoelectrodes,” *ChemSusChem*, vol. 4, no. 4, pp. 432–449, 2011.

[80] M. H. Samat, M. F. . Taib, O. . Hassan, M. Z. . Yahya, and A. M. . Ali, “Structural, electronic and optical properties of brookite phase titanium dioxide,” *Mater. Res. Express*, vol. 4, no. 4, p. 044003, 2017.

[81] M. Kumar and C. Persson, “Cu_2ZnSnS_4 and $Cu_2ZnSnSe_4$ as potential earth-abundant thin-film absorber materials: A aensity functional theory study,” *Int. J. Theor. Appl. Sci.*, vol. 5, no. 1, pp. 1–8, 2013.

[82] L. Ling, J. Song, S. Zhao, R. Zhang, and B. Wang, “DFT study on the effects of defect and metal-doping on the decomposition of H_2S on the α–Fe_2O_3(0001) surface,” *RSC Adv.*, vol. 4, no. 43, pp. 22411–22418, 2004.

[83] H. Pan, X. Meng, J. Cai, S. Li, and G. Qin, “(Ti/Zr, N) codoped hematite towards the enhanced photoelectrochemical activity of water splitting,” *Phys. Chem. Chem. Phys.*, vol. 3, no. 17, p. 22179, 2015.

[84] H. Muta, K. Kurosaki, M. Uno, and S. Yamanaka, “Thermoelectric properties of Ti- and Sn-doped a-Fe_2O_3,” *Wuli Xuebao/Acta Phys. Sin.*, vol. 67, no. 19, pp.

200–202, 2001.

[85] Z. D. Pozun and G. Henkelman, “Hybrid density functional theory band structure engineering in hematite,” *J. Chem. Phys.*, vol. 134, no. 22, pp. 1–9, 2011.

[86] Suman *et al.*, “Understanding the role of Ni ions on the photocatalytic activity and dielectric properties of hematite nanostructures: An experimental and DFT approach,” *J. Phys. Chem. Solids*, vol. 156, no. April, p. 110118, 2021.

[87] C. Xia, Y. Jia, M. Tao, and Q. Zhang, “Tuning the band gap of hematite α-Fe2O3 by sulfur doping,” *Phys. Lett. Sect. A Gen. At. Solid State Phys.*, vol. 377, no. 31–33, pp. 1943–1947, 2013.

[88] Y. Liu, Y. X. Yu, and W. De Zhang, “Photoelectrochemical properties of Ni-doped Fe_2O_3 thin films prepared by electrodeposition,” *Electrochim. Acta*, vol. 59, pp. 121–127, 2012.

[89] Y. Yin, X. Zhang, and C. Sun, “Transition-metal-doped Fe2O3 nanoparticles for oxygen evolution reaction,” *Prog. Nat. Sci. Mater. Int.*, vol. 28, no. 4, pp. 430–436, 2018.

[90] A. H. Wilson and R. H. Fowler, “The electrical conductivity of the transition metals.,” *Proc. R. Soc. A Math. Phys. Eng. Sci.*, vol. 167, no. 931, pp. 580–593, 1938.

[91] S. Sivakumar, D. Anusuya, C. P. Khatiwada, J. Sivasubramanian, A. Venkatesan, and P. Soundhirarajan, “Characterizations of diverse mole of pure and Ni-doped α-Fe_2O_3 synthesized nanoparticles through chemical precipitation route,” *Spectrochim. Acta - Part A Mol. Biomol. Spectrosc.*, vol. 128, pp. 69–75, 2014.

[92] W. Cheng *et al.*, “Ni-doped overlayer hematite nanotube: A highly photoactive architecture for utilization of visible light,” *J. Phys. Chem. C*, vol. 116, no. 45, pp. 24060–24067, 2012.

[93] D. Varshney and A. Yogi, “Structural and Electrical conductivity of Mn doped Hematite (α-Fe_2O_3) phase,” *J. Mol. Struct.*, vol. 995, no. 1–3, pp. 157–162, 2011.

[94] R. Reveendran and M. A. Khadar, “Structural, optical and electrical properties of Cu doped α-Fe_2O_3 nanoparticles,” *Mater. Chem. Phys.*, vol. 219, pp. 142–154, Nov. 2018.

[95] P. Kumar, P. Sharma, R. Shrivastav, S. Dass, and V. R. Satsangi, “Electrodeposited zirconium-doped α-Fe_2O_3 thin film for photoelectrochemical water splitting,” *Int. J. Hydrogen Energy*, vol. 36, no. 4, pp. 2777–2784, 2011.

[96] P. Liao, J. A. Keith, and E. A. Carter, “Water oxidation on pure and doped hematite (0001) surfaces : Prediction of Co and Ni as effective dopants for photocatalysis Water oxidation on pure and doped hematite (0001) surfaces : Prediction of Co and Ni as effective dopants for electrocatalysis,” no. 0001, 2012.

[97] J. Velev, A. Bandyopadhyay, and W. H. Butler, “Electronic and magnetic structure of transition-metal-doped -hematite,” pp. 1–7, 2005.